Magnetic Resonance Velocimetry for Fast Liquid Flows

Zur Erlangung des akademischen Grades eines

DOKTORS DER INGENIEURWISSENSCHAFTEN
(Dr.-Ing.)

von der KIT-Fakultät für Maschinenbau des

Karlsruher Instituts für Technologie (KIT)

angenommene

DISSERTATION

von

M.Sc. Mehrdad Alinaghian Jouzdani

Tag der mündlichen Prüfung:	08.12.2023
Referent:	Prof. Dr. Jan Gerrit Korvink
Korreferent:	Prof. Dr. Dr. h.c. Jürgen Hennig

Karlsruher Institut für Technologie
Institut für Mikrostrukturtechnik
Hermann-von-Helmholtz Platz 1
76344 Eggenstein-Leopoldshafen

Abstract

Magnetic resonance velocimetry, as a non-invasive contactless method, is the central core of this thesis. In addition to mean flow measurement, this method can obtain a three-dimensional three-component (3D-3C) velocity map to visualize flow behavior in clinical and industrial applications. In this method, the measurement signal comes directly from the sample's nuclei, making it a very precise and reliable technique. However, some limitations and instances of inaccurate results are reported. Based on the available literature, three main issues are reported for NMR/MRI flow measurement. The first is the obstacles to using the NMR technique in commercial flowmeters. The second topic is the length of echo time, the main bottleneck for fast flow measurement. The last one is the velocity encoding parameter (V_{enc}), whose small values result in aliasing, and big values reduce phase-SNR for slow-moving voxels.

Despite extremely high precision in measuring flow rate by the available NMR spectrometers, this technique is not broadly used in the flowmeter industry. The main barriers are the high cost and large volume. The main limitation of a compact NMR magnet is the instability, more precisely, the *drift* in working frequency. In the current study, the pulse sequence and measurement parameters of an affordable and portable NMR-based flowmeter are optimized to counteract the drift issue. A pulse sequence is designed based on the flow encoding bipolar gradient and the *Job Acquisition* technique. The former encodes the flow in the MR phase, and the latter enables us to have two acquisitions after each excitation. The first acquisition is before, and the second one is after the bipolar gradient. The first is used as the reference, and the second contains the injected phase due to flow. Having both acquisitions in a single measurement reduces the consequences of the drift. In addition, all other parameters, including the bandwidth of the excitation pulse, bipolar gradient, and acquisition times, are optimized, and the adjustment is limited to the *Drift Adjustment*. The designed pulse sequence is tried on a compact and affordable NMR-based flow meter, and the results show robust measurements.

Available studies show that the maximum measurable velocity is directly related to the length of the echo time. Conventionally, flow imaging is based on a slice selective excitation pulse and then applying a flow encoding gradient (preceding spatial encoding gradients). In this study, these two steps are merged. Instead, a slice selective flow encoding excitation pulse is designed using optimal control theory. A constraint is added to make the pulse slice selective. Due to being over-constrained, the optimal control problem is divided into two steps. In the first one, a mathematical model is proposed to encode the velocity of the central plane of the excited slice into the MR phase. The Pontryagin Maximum Principle is used to solve the optimal control problem, and the GRadient Ascent Pulse Engineering (GRAPE) algorithm is employed to maximize the Hamiltonian. Despite being nonlinear, a bijective relationship between phase and velocity is established. However, the evaluations show that the phase over the thickness of the excited slice is nonuniform. Therefore, the second step of the optimal control problem is initiated, whose target is to minimize the nonuniformity. Even though some nonuniformity is still left, the assessments show significant improvement in the uniformity. The results show that the increase in length of echo time caused by flow encoding is 1.58 times shorter in the optimal control method compared to the bipolar gradient technique. Furthermore, the slice refocusing gradient is not needed, which makes this method much more time-efficient.

The last topic is about the velocity encoding parameter V_{enc}, which plays a central role in phase contrast flow measurement. The value of this parameter should be slightly bigger than the maximum velocity expected in the flow system. The problem is that the phase-velocity resolution for the voxels moving significantly slower than V_{enc} is too low. Also, if the V_{enc} is smaller than needed, aliasing happens, and the imaging goes through wrapping, which results in considerable errors. In the current thesis, selective excitation is employed to tackle this issue. In the presence of several chemical groups, selective excitation enables us to define a different value of V_{enc} for each group. For the present research, this technique is applied to flow NMR, and the number of groups is limited to two (water and sodium acetate). The bigger value of V_{enc}, representing the maximum velocity in the system, is assigned to sodium acetate, and the smaller one is defined for water. The injected phase in the signal coming from water goes through the wrapping. However, that of sodium acetate can be used to unwrap it reliably. The ratio between values of V_{enc} is 7, which means that the phase-SNR is improved by the same factor. In flow NMR, the whole volume is treated as one voxel, which results in phase dispersion and, hence, loss of signal. It confines the maximum achievable ratio between the values of V_{enc}. In flow imaging, much higher ratios are expected.

Zusammenfassung

Magnetische Resonanz-Velozimetrie, als eine nicht-invasive berührungslose Methode, bildet das Kernstück dieser Dissertation. Neben der Messung des mittleren Durchflusses kann mit dieser Methode auch eine dreidimensionale und dreikomponentige (3D-3C) Geschwindigkeitskarte erstellt werden, um das Durchflussverhalten in klinischen und industriellen Anwendungen zu visualisieren. Bei dieser Methode stammt das Messsignal direkt von den Atomkernen der Probe, was sie zu einer sehr präzisen und zuverlässigen Technik macht. Es gibt jedoch einige Einschränkungen und Fälle von ungenauen Ergebnissen. Basierend auf der vorhandenen Literatur werden drei Hauptprobleme für die NMR-/MRI-Flussmessung genannt. Das erste sind die Hindernisse für die Verwendung der NMR-Technik in kommerziellen Durchflussmessgeräten. Das zweite Thema ist die Echolaufzeit, die den Hauptengpass für schnelle Durchflussmessungen darstellt. Der letzte Punkt betrifft den Geschwindigkeitscodierungsparameter (V_{enc}), dessen kleine Werte zu Aliasing führen, während große Werte die Phasen-SNR für langsame bewegte Voxel verringern.

Trotz der äußerst hohen Präzision bei der Messung der Durchflussrate mit den verfügbaren NMR-Spektrometern wird diese Technik in der Durchflussmessgeräteindustrie nicht in großem Umfang eingesetzt. Die Hauptbarrieren sind die hohen Kosten und das große Volumen.. Die größte Einschränkung eines kompakten NMR-Magneten ist die Instabilität, genauer gesagt, der *Drift* der Arbeitsfrequenz. In der vorliegenden Studie werden die Pulssequenz und die Messparameter eines erschwinglichen und tragbaren NMR-basierten Durchflussmessgeräts optimiert, um dem Problem des Drifts entgegenzuwirken. Es wurde eine Pulssequenz entwickelt, die auf dem bipolaren Flusskodierungsgradienten und der *Job Acquisition*-Technik basiert. Erstere codiert den Fluss in der MR-Phase, und letztere ermöglicht es, zwei Akquisitionen nach jeder Anregung durchzuführen. Die erste Aufnahme erfolgt vor, und die zweite erfolgt nach dem bipolaren Gradienten. Die erste wird als Referenz verwendet, und die zweite enthält die durch den Fluss injizierte Phase. Da beide Erfassungen in einer einzigen Messung erfolgen, werden die Folgen des Drifts verringert. Darüber hinaus werden alle anderen Parameter, einschließlich der Bandbreite des Anregungspulses, des bipolaren Gradienten und der Erfassungszeiten, optimiert, und die Anpassung beschränkt sich auf die "Driftanpassung". Die entworfene Pulssequenz wird auf einem kompakten und kostengünstigen NMR-basierten Durchflussmesser getestet und die Ergebnisse zeigen robuste Messungen.

Verfügbare Studien zeigen, dass die maximal messbare Geschwindigkeit direkt mit der Länge der Echolaufzeit zusammenhängt. Konventionell basiert die Durchflussbildgebung auf einem schichtselektiven Anregungspuls und der anschließenden Anwendung eines Flusskodierungsgradienten (welchem ein räumlicher Kodierungsgradient vorausgeht). In dieser Studie werden diese beiden Schritte zusammengeführt. Stattdessen wird ein schichtselektiver, flusskodierender Anregungsimpuls mit Hilfe der Theorie der optimalen Steuerungen (optimal control) entworfen. Es wird eine Nebenbedingung hinzugefügt, um den Puls schichtselektiv zu machen. Aufgrund der übermäßigen Einschränkung wird das Problem der optimalen Steuerung in zwei Schritte unterteilt. Im ersten Schritt wird ein mathematisches Modell vorgeschlagen, um die Geschwindigkeit der zentralen Ebene der angeregten Schicht in die MR-Phase zu kodieren. Das Pontryagin-Maximum-Prinzip wird zur Lösung des optimalen Steuerungsproblems verwendet, und der GRadient Ascent Pulse Engineering (GRAPE)-Algorithmus wird zur Maximierung des Hamiltonian eingesetzt. Trotz der Nichtlinearität des Problems wird eine bijektive Beziehung zwischen Phase und Geschwindigkeit hergestellt. Die Auswertungen zeigen jedoch, dass die Phase über die Dicke der angeregten Schicht nicht gleich-

mäßig ist. Daher wird der zweite Schritt der optimalen Steuerung eingeleitet, dessen Ziel es ist, die Ungleichmäßigkeit zu minimieren. Obwohl immer noch eine gewisse Ungleichmäßigkeit vorhanden ist, zeigen die Bewertungen eine deutliche Verbesserung der Gleichmäßigkeit. Die Ergebnisse zeigen, dass die Verlängerung der Echozeit, verursacht durch die Flusscodierung, bei der optimalen Steuermethode im Vergleich zur bipolaren Gradiententechnik um den Faktor 1,58 kürzer ist. Darüber hinaus ist der Schichtrefokussierungsgradient nicht erforderlich, was diese Methode viel zeiteffizienter macht.

Das letzte Thema betrifft den Geschwindigkeitscodierungsparameter V_{enc}, der eine zentrale Rolle bei der Phasenkontrastflussmessung spielt. Der Wert dieses Parameters sollte leicht größer sein als die maximale erwartete Geschwindigkeit im Flusssystem. Das Problem besteht darin, dass die Auflösung der Phasen-Geschwindigkeit für die Voxels, die deutlich langsamer als V_{enc} bewegen, zu gering ist. Wenn V_{enc} kleiner als erforderlich ist, kommt es zu Aliasing, und die Bildgebung wird überlagert, was zu erheblichen Fehlern führt. In der vorliegenden Dissertation wird eine selektive Anregung verwendet, um dieses Problem zu lösen. Bei Vorhandensein mehrerer chemischer Gruppen ermöglicht es die selektive Anregung, für jede Gruppe einen anderen Wert für V_{enc} festzulegen. Für die vorliegende Arbeit wird diese Technik auf die Fluss-NMR angewendet, und die Anzahl der Gruppen wird auf zwei begrenzt (Wasser und Natriumacetat). Der größere Wert von V_{enc}, der die maximale Geschwindigkeit im System darstellt, wird Natriumacetat zugewiesen, und der kleinere wird für Wasser definiert. Die eingeführte Phase im Signal, das von Wasser stammt, wird eingehüllt. Diejenige von Natriumacetat kann jedoch zuverlässig verwendet werden, um sie zu enthüllen. Das Verhältnis zwischen den Werten von V_{enc} beträgt 7, was bedeutet, dass die Phasen-SNR um denselben Faktor verbessert wird. In der Fluss-NMR wird das gesamte Volumen als ein Voxel behandelt, was zu Phasendispersion und somit zu Signalverlust führt. Dadurch wird das maximal erreichbare Verhältnis zwischen den Werten von V_{enc} begrenzt. Bei der Durchflussbildgebung werden jedoch wesentlich höhere Verhältnisse erwartet.

Nomenclature

Abbreviations

2D	Two dimensional
3C	Three component
3D	Three dimensional
BPP-LED	Bipolar pulse longitudinal eddy-current delay
CEMRA	Contrast-enhanced magnetic resonance angiography
CFD	Computational fluid dynamics
DIR	Double inversion recovery
DQM	Differential quadrature method
DW	Diffusion weighted
DW-MRI	Diffusion-weighted magnetic resonance imaging
EPI	Echo planar imaging
FEM	Finite element method
FID	Free induction decay
FLASH	Fast low-angle shot
FOV	Field of view
FT	Fourier transformation
FWHM	Full width at half maximum
HOT	Higher order terms
HWA	Hot wire anemometer
IR	Inversion recovery
LDA	Laser Doppler anemometry
MR	Magnetic resonance
MRI	Magnetic resonance imaging
MRS	Magnetic resonance spectroscopy

MRV	Magnetic resonance velocimetry
NMR	Nuclear magnetic resonance
OC	Optimal control
OCP	Optimal control problem
OCT	Optimal control theory
PC	Phase contrast
PC-MRI	Phase contrast flow MRI
PFG-STE	Pulsed-field gradient stimulated echo
PGSE	Pulsed gradient spin echo
PIV	Particle imaging velocimetry
PMP	Pontryagin maximum principle
ppm	Parts per million
RARE	Rapid acquisition with relaxation enhancement
RF	Radio frequency
ROI	Region of interest
SNR	Signal to noise ratio
SPI	Single point imaging
SPRITE	Single point ramped imaging with T1 enhancement
SSG	Slice selection gradient
SWI	Susceptibility weighed imaging
TE	Echo time
TIR	Triple inversion recovery
TOF	Time of flight
TONE	Tilted optimized non-saturating excitation
TR	Repetition time
TS	Target state
UT	Ultrasonic technique
VOI	Volume of interest

Constants

h	Planck constant
k	Boltzmann constant

Symbols

δ	Chemical shift
γ	Gyromagnetic ratio
ω_0	Larmor frequency
$\vec{\mu}$	Spin magnetic moment
$\vec{S}$	Spin angular momentum
B_0	Static magnetic field
B_1	RF magnetic field
I	Spin quantum number
M_0	Net magnetisation
M_T	Transverse magnetisation
M_z	Longitudinal magnetisation
T	Temperature
T_1	Longitudinal (spin-lattice) relaxation time
T_2	Transverse (spin-spin) relaxation time
T_2^*	Effective transverse (spin-spin) relaxation time

Contents

1 Introduction

Magnetic resonance (MR) is known mostly for the imaging application in clinical studies. However, it has many more applications not only in clinical but also in industrial investigations. MR spectroscopy, thermometry, elastography, and flow measurement are some of the applications, among which the latter is in the interest of this study. In this thesis, the application of MR in velocimetry is discussed. In the first chapter, it is explained why we are motivated to employ this method among all available experimental techniques. Then, the challenges and limitations of the method are discussed, and upon them, the objectives are defined. At the end of the chapter, the thesis outline is presented, in which the main objectives and the corresponding solutions are explained.

1.1 Motivation

Understanding fluid flow behavior is among the most important industrial and clinical applications. MR enables us to measure the velocity of the sample in a noninvasive manner. MR flow measurement can be divided into two primary groups: flow NMR and flow MRI. In flow NMR, the mean velocity is under investigation, while in flow MRI, the aim is to have a 3D flow map.

Flow NMR is a matter of interest in the design of flowmeters. There are several methods to design the flow sensors. Electrical capacitance tomography sensors measure the flow rate by measuring the change in capacitance values between electrodes due to flow [1]. In ultrasonic tomography, the reflection of ultrasonic waves is used to identify the flow regime within the sample holder [2]. Electromagnetic flowmeters use the change in induced voltage caused by velocity to measure the flow rate [3]. In the opposite of all of these methods, NMR flowmeters employ the signal emitted directly from the nuclei and demonstrate high accuracy in mean flow measurement. So, the application of NMR, as a non-invasive method, can be extremely helpful in flowmeter design. In addition, the ability to perform spectroscopy experiments in parallel with flow measurement makes this method remarkably instrumental in monitoring flow rate and chemical reactions in the same measurement.

Flow MRI, or MRV, can provide a 3D flow map, including all velocity components of the voxels. A precise conception of this behavior can enhance many industrial productions due to the significant effect of fluid flow on the efficiency of many technological advances such as internal combustion engines, turbojets, gas/wind turbines, pipelines, and heating/cooling systems. Also, it can be exceptionally beneficial to prevent or cure many diseases in clinical applications. A variety of methods have been presented to evaluate flow behavior. Still, in general, fluid dynamics problems are addressed in three main categories, including analytical studies, computational fluid dynamics, and experimental approaches. Analytical studies are used to analyze fluid behavior, such as laminar flows, which can lead to very accurate results. Despite their accuracy, analytical approaches have specific limitations since they are not capable of solving turbulent or geometrically complicated models.

In such complicated conditions, we can utilize computational fluid dynamics (CFD) as a powerful method. CFD codes provide a comprehensive visualization of flow behavior, but there are also some limitations and errors due to difficulties in modeling, which are inevitable in this approach. For instance, we can consider the difficulties of a vascular system modeling for blood flow investigation as a very sophisticated flow system [4]. Beyond the mentioned problem, if we can model these complex situations, we need massively parallel supercomputers to do these enormous computations.

The importance of experimental approaches is absolutely clear in fluid dynamics and other engineering and clinical sciences. These methods have demonstrated a strong ability to solve very complicated problems, such as highly turbulent cases, where the computational methods cannot be used due to the above-mentioned reasons. These merits give more credit to experimental methods. Several experimental methods have been introduced for fluid dynamics problems, and MRV is one of them. In the following, the whys and wherefores of magnetic resonance velocimetry are discussed. Hot wire anemometer (HWA) [5], Laser Doppler anemometer (LDA) [5, 6], particle image velocimetry (PIV) [7] and ultrasonic technique (UT) [8] are among the most prominent methods which have been used in order to assess fluid dynamics problems. In addition to the previous methods, magnetic resonance velocimetry (MRV) is considered to be a very useful and efficient method to investigate flow behavior. The following reasons are the main motivations to use MRV in fluid flow assessment and show the superiority of the present method.

MRV is a completely non-invasive method, while in some methods, such as HWA, embedded probes are required to measure the velocities [5], which can disturb the flow behavior itself and, as an invasive method, restrain the applicability, especially in clinical applications. Making a comparison between LDA and MRV illustrates the superiority of the latter. The MR signal, which is used to measure the velocity in MRV, is sent directly from the nuclei of the fluid, while in LDA, as well as PIV, the velocity of particles is measured rather than the velocity of the fluid itself. So, even if the seeding particles don't change the properties of the liquid, these methods result in inaccurate results if the particles don't follow the fluid streamlines [6]. In addition, MRV is more time-efficient than LDA [5], and, in contrast to LDA, it doesn't need any optical access to the sample. Also, the ultrasonic technique can be used to have a mean velocity measurement, but MRV has the ability to give a three-dimensional, three-component velocity map. Utilizing MRV, all velocity components of any voxel on a 2D plane or 3D volume can be measured with a high spatial resolution (<50 µm) [9]. In summary, this method brings a lot of benefits, such as capability in complex situations, accuracy, time efficiency, and non-invasiveness, which make this method suitable for analyzing flow with complicated geometries.

1.2 Objectives

The first aim of the present study is about mean flow measurement. There are several techniques to measure the flow rate, including electrical capacitance tomography [1], ultrasonic tomography [2], and electromagnetic flowmeters [3]. NMR, as a non-invasive contactless method, can be employed to measure the flow rate as well. Receiving the measurement signal directly from the nuclei makes this method exceptionally reliable. NMR spectrometers can obtain even a precise three-dimensional three-component velocity map of a sample for velocities up to $50\,\mathrm{m\,s^{-1}}$[9]. So, they are also significantly reliable in mean flow measurement. However, this method is not widely and commercially used in the flowmeter industry [10]. The main reasons are the high cost and big volume of NMR spectrometers. In industrial applications, compact and portable sensors are needed to perform the measurement on-site. Also, as a commercial sensor, NMR-based flowmeters are more expensive than the alternatives. However, in the case of mean flow measurement, lower values of SNR are needed, and more reasonable spectrometers can replace sophisticated ones. Nevertheless, such devices can't have the robustness of the usual spectrometers. There are several issues, but the main one is the drift in the working frequency. In this study, it is tried to propose some techniques to optimize the flow measurement pulse sequence to counteract this issue. Therefore, **"Pulse sequence optimization for compact NMR flowmeters"** is defined as the first objective of the current thesis.

MRV measurement has a variety of advantages in 3D flow visualization. However, there are some cases that could lead to inaccurate results. The areas right after sharp bends, as well as separated and secondary flows, result in highly turbulent cases, which are known as the most important inaccurate case studies [8]. In such conditions, some voxels have velocities considerably bigger than the mean velocity of flow. These situations lead to dephasing and aliasing. Consequently, we realize that MRV measurement presents unreliable results where the range of velocity or its fluctuations crosses a certain threshold [8, 11].

In the following, the most prominent issues that affect the accuracy of the measurement have been discussed.

Uncertainty (StdDev) in MRV measurement depends on the highest expected velocity (V_{enc}) and signal-to-noise ratio (SNR) according to the following relationship [12],

$$\text{StdDev} = \frac{\sqrt{2}}{\pi} \cdot \frac{V_{\text{enc}}}{\text{SNR}}. \tag{1.1}$$

Based on Equation 1.1, an enhancement in SNR could help the reliability of the method [13]. SNR is in a direct relationship with the following variables [14],

$$\text{SNR} = K \frac{\omega_0 B_1^* M_0 V_s}{\sqrt{4FkTt_{aq}R}} T_2^* \left(1 - e^{-t_{aq}/T_2^*}\right). \tag{1.2}$$

where K is the factor of B_1 inhomogeneity, ω_0 is the Larmor frequency, B_1^* is the strength of transverse magnetic field induced by the RF coil per unit of current, M_0 is the sample magnetization, which is a function of B_0 and the nuclei concentration, V_s is the volume of the sample, F is the preamplifier noise factor, k is the Boltzmann constant, T is temperature, t_{aq} is the acquisition time, R is the coil resistance, T_2^* is the observed or effective transverse relaxation time. Most of the mentioned parameters are related to the hardware of the spectrometer. In order to enhance measurement accuracy, SNR can be improved by an increase in magnetic field and voxel size [15]. They respectively improve ω_0 and V_s in Equation 1.2. But from another point of view, an increase in voxel size leads to more partial volume artifacts and also decreases spatial resolution. Also, a higher magnetic field results in a higher initial and running cost; it makes shielding more complicated and increases the power absorption rate. Another effective parameter is receiver coil [15], which should be precisely optimized depending on the sample and the required application. However, in the current research, we focus on the software's effective parameters, particularly the employed pulse sequence and related innovative techniques.

After the excitation, the signal decays due to two phenomena: longitudinal and transverse relaxation[1]. The longitudinal relaxation is basically the process in which the excited spins will be recovered and get back to the equilibrium condition. In this process, longitudinal magnetization is a function of time and a time constant called *spin-lattice relaxation time* (T_1) and follows the equation below [15],

$$M_z(t) = M_0\left(1 - e^{-t/T_1}\right). \tag{1.3}$$

The transverse relaxation is basically a loss of signal due to spin-spin interactions. Signal, or in other words, transverse magnetization, is a function of time and *spin-spin relaxation time* (T_2) [15],

$$M_{xy}(t) = M_0 e^{-t/T_2}. \tag{1.4}$$

Equation 1.4 demonstrates the exponential decay of the MR signal versus time. It shows the significant effect of time on the signal decay. So, the faster we perform the experiment, the more signal we have.

The dephasing parameter (DP) is another term that shows the importance of time in flow measurement. The value of DP can affect the accuracy of the method. It is defined as [8, 16]

$$DP = \frac{X_d}{X_v} = \frac{\mathrm{TE} \cdot V}{X_v}, \tag{1.5}$$

in which X_v is the length of the voxel, and X_d is the displacement of spin during echo time, and V is the velocity. Dephasing happens for DP values bigger than one [8]. In fact, when the displacement of spin goes beyond the length of the voxel during echo time (TE), it decreases the measurement accuracy. So, a decrease in TE can enhance precision. That is why pulse sequences with shorter TE are preferred for fast flow measurements, and any technique that can reduce TE can be extremely helpful.

---

[1] That holds in the absence of any inhomogeneity.

In order to make a reliable measurement, the aforementioned issues should be taken into consideration, which is why the most prominent part of MRV measurement is the pulse sequence technique [9, 17]. It consists of several parameters, such as echo time (TE), repetition time (TR), phase encoding, frequency encoding, slice selection gradient, and radio frequencies. Different combinations of these parameters can completely change the characteristics of the method. In order to clarify the distinction between different pulse sequence techniques, simple spin echo and SPIRAL pulse sequences are shown in Figure 1.1. In this figure, RF is radio frequency, G_{ss} is slice selection gradient, G_{fe} is flow encoding gradient, G_{ph} is phase encoding gradient, and G_{fr} is frequency encoding or readout gradient. The properties and capabilities of these sequences in different applications can be completely distinct.

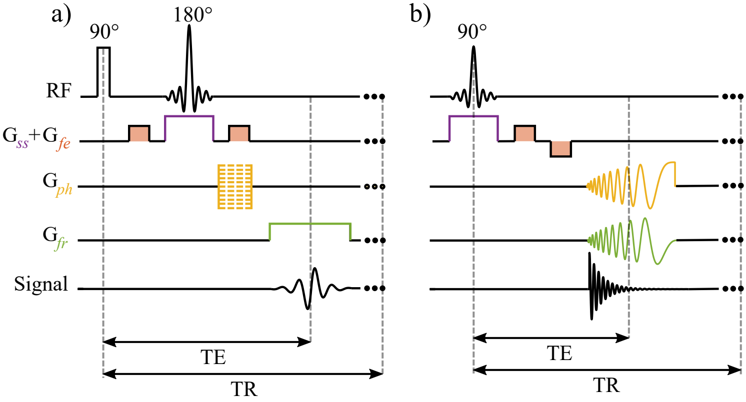

Figure 1.1: Schematic representation of (a) a simple spin echo and (b) a SPIRAL flow imaging pulse sequence [9].

As mentioned, the pulse sequence technique plays an important role in the accuracy and time efficiency of the measurement process [9, 18]. Several pulse sequence techniques in MRV are used to measure the velocity field of flow. For instance, single spin echo, Echo Planar Imaging (EPI), spiral, Rapid Acquisition with Relaxation Enhancement (RARE), Fast Low Angle SHot (FLASH), Single

Point Imaging (SPI), and Single Point Ramped Imaging with T1 Enhancement (SPRITE), which is a version of SPI, are among the most important ones. There are different advantages and disadvantages for each one, which makes them suitable for a particular application [9]. According to the results, SPI (SPRITE) is applicable for the highest range of velocity ($0.5 - 50\,\mathrm{m\,s^{-1}}$), while EPI seems comparatively more time efficient ($20 - 100\,\mathrm{ms}$). The former is appropriate for samples with shorter T_2^* yet inappropriate for transient flows while the latter is suitable for transient cases [9].

In Table 1.1, a comprehensive comparison between different characteristics of some velocimetry pulse sequences is presented. It is done by Lynn F. Gladden and Andrew J. Sederman [9]. According to the results, the most capable technique in fast flow velocity measurement is SPI (SPRITE), which is able to measure velocities up to $50\,\mathrm{m\,s^{-1}}$[9].

In addition, there are some techniques to improve flow measurement accuracy, which can be used by any pulse sequence. For example, the measurement can be performed two times with identical parameters, once with flow and once without flow. The subtraction of the results can eliminate the effect of some parameters unrelated to the flow and result in more accurate measurements [19]. In the research done by C.J. Elkins [8], 4D MRV has been used as a method to achieve higher values of SNR in comparison with the 2D MRV measurement. Furthermore, the effect of some parallel imaging techniques including *Simultaneous Acquisition of Spatial Harmonics* (SMASH) or *Sensitivity Encoding* (SENSE) has been addressed, and according to results, although these techniques make this method more time efficient, they can cause a decrease in SNR [8].

All the abovementioned points, including the decay of signal (Equations 1.3), dephasing parameter (Equation 1.5), and effect of the employed pulse sequence, show the importance of pulse sequence and especially TE in MRV experiments. As shown in Table 1.1, for fast flow measurement, SPI, which has the shortest TE, is the most capable one. As a result, **"Reduction of the echo time (TE) in flow imaging pulse sequences"** is considered the second objective in the current research.

Table 1.1: Comparison of different pulse sequences in their application to velocity imaging (modified with permission from [9]).

Pulse sequence	Acquisition time	Measured velocity	Comments
Single spin echo	1 – 100 min	Up to 5 $\mathrm{m\,s^{-1}}$	Slow acquisition but applicable to most relaxation times. Suitable for short T_2 and T_2^*. Acquisition time decreases as T_1 decreases. High spatial resolution is possible. Too slow to capture transient behavior.
EPI	20 – 100 ms	1 – 100 $\mathrm{cm\,s^{-1}}$	Applicable to transient systems characterized by long T_2^* (TE = 10 – 100 ms). Less sensitive to gradient imperfections than spiral sequences.
Spiral	3 – 25 ms	Up to 5 $\mathrm{m\,s^{-1}}$	Can probe systems with shorter T_2^* than EPI (since TE=3-25 ms). Possibility of small tip angle excitation and rapid image frame rate. More complex image reconstruction than EPI.
RARE	2 – 10 s	Up to 10 $\mathrm{cm\,s^{-1}}$	Higher spatial resolution achieved than with EPI and spiral. Appropriate for studying slowly changing systems. Requires long T_2 but can cope with quite short T_2^* (TE=50-500 *ms*). Usually, it is too slow to capture transient behavior.
FLASH	>150 ms	50 $\mathrm{cm\,s^{-1}}$	Best for short T_1 (<50 ms) to achieve rapid recycle, short T_2; moderately short T_2^*. Low SNR leads to low-moderate spatial resolution. Very robust. Usually, it is too slow to capture transient behavior.
SPI (SPRITE)	Seconds to hours (time-averaged)	0.5 – 50 $\mathrm{m\,s^{-1}}$	Suitable for very short T_2^*. Too slow to capture transient behavior.

Back to Equation 1.1, uncertainty is directly proportional to the value of velocity encoding (V_{enc}). The value must be greater than the highest expected velocity. Otherwise, the injected phase goes beyond π, and aliasing happens, which leads to considerable errors [8]. Nevertheless, based on Equation 1.1, as the value of V_{enc} increases, the uncertainty rises. That is why V_{enc} is considered just slightly greater than the highest expected velocity. The velocity-phase resolution, or phase-SNR, is always a proportion of V_{enc}. It means that change in velocities much smaller than V_{enc} can't be measured. This is an issue in fast flow measurement when the velocity of a number of voxels is much higher than the average flow. In such cases, big values of V_{enc} are needed, and flow measurement suffers from a low value of phase-SNR in slow-moving regions, which include most of the voxels. So, the last topic of the current thesis entitles **"Enhancement of phase-SNR versus the value of V_{enc}"**.

1.3 Outline

In conclusion, the current thesis follows three main objectives described below.

1. **Pulse sequence optimization for a compact NMR flowmeter**
   A compact, affordable NMR device enables us to benefit from the MR techniques and perform precise flow experiments on-site. Such a device makes MR methods more accessible in many clinical, industrial, and environmental applications. However, portable permanent magnets can't reach the stability of the superconducting ones. This issue can be managed by an optimized pulse sequence.

   In this study, a pulse sequence is designed based on the application of bipolar flow encoding gradient and by use of the job acquisition technique. In addition, effective parameters are optimized to perform robust and reliable flow measurements by a compact portable NMR-based flowmeter.

2. **Reduction of the echo time (TE) in flow imaging pulse sequences**
   Echo time plays a crucial role in MR velocimetry. A shorter TE is always preferred due to a number of reasons. First, the MR signal decays exponentially. So, shorter TE means high SNR. Second, in fast flow measurement, each scan has to be finished before the sample leaves the coil. Third, shorter echo time reduces the dephasing parameter (Equation 1.5).

   In this research, the optimal control method is employed in order to design a slice-selective flow encoding RF pulse. Flow encoding is conventionally accomplished by applying a bipolar gradient after the excitation pulse. In this study, the designed optimal control pulse combines two steps and performs both jobs (slice selective excitation and flow encoding) at the same time. Using this method, the delay caused by the flow encoding in the TE is 1.58 times shorter than that of the bipolar gradient method. Moreover, the slice refocusing gradient is no longer required.

3. **Enhancement of phase-SNR versus the value of V_{enc}**
   V_{enc} is the key parameter in MR flow evaluation. It is defined as the maximum velocity that is likely to be encountered in the flow system. This value should be chosen precisely to avoid aliasing on the one hand and not to increase the standard deviation (StdDev) on the other hand. Since StdDev is directly proportional to V_{enc}, any value of V_{enc} imposes a certain limitation on the velocity-phase resolution.

   In this project, selective excitation is utilized in combination with the chemical shift to tackle this issue. Chemical shift between chemical groups lets us excite and encode each chemical compound separately. This feature enables us to define a different value of V_{enc} for each compound. Multiple values of V_{enc} provide a much higher phase-velocity resolution. In fact, the higher value of V_{enc} guarantees that aliasing is prevented, and the smaller one increases the resolution.

In the current chapter, entitled **Introduction**, the motivation, objective, and outline of the thesis are presented. The fundamentals of MR applications are explained in Chapter 2, titled **Theoretical background**. The three principal bottlenecks mentioned above are addressed in the next three chapters, including **MRV for compact flowmeters** in Chapter 3, **Optimal control theory for time-efficient MRV** in Chapter 4, and **Application of selective excitation in MRV** in Chapter 5. In the final chapter, a brief **Conclusion** is presented, and potential topics for further studies are presented.

2 Theoretical background

The content presented in this chapter was mostly derived from the following valuable books:
Spin Dynamics [20], *NMR Spectroscopy* [21], *Handbook of MRI Pulse Sequences* [22], *Understanding NMR Spectroscopy* [23], *MRI from picture to proton* [24].

Magnetic resonance, as a non-invasive method, has a variety of applications, which are classified into two main categories: spectroscopy and imaging. It can be used to obtain an image to visualize organs of the body, which is extremely helpful in clinical diagnosis, or it can be employed in biochemistry to discover the chemical compounds in a sample. There are many more applications, such as velocity and diffusion measurement. But, before venturing into the applications, some terms and definitions should be explained. In this chapter, the fundamentals of magnetic resonance, including spin, magnetization evolution, nuclear magnetic resonance (NMR), magnetic resonance imaging (MRI), magnetic resonance velocimetry (MRV), and related terms and definitions are explained.

2.1 Spin

First, we need to know where the MR signal comes from. The signal is generated from an intrinsic quantum characteristic of the atomic nuclei, called the *spin*. Spin, or spin angular momentum , is a purely quantum property of elementary particles, namely protons and neutrons[1]. Spinning of those particles generates

---

[1] Electrons also have spin, but in this study, we focus only on the spin of nuclei.

the spin angular momentum. In point of fact, all subatomic particles possess spin. But, the way they interact defines the overall spin of the nuclei. In an atom like ^{12}C, spins are paired against each other, and the overall spin of the nucleus is zero, but for example, in ^{13}C, the overall spin is non-zero. The spin of a nucleus can be calculated by the equation below [25].

$$|S| = \hbar\sqrt{I(I+1)} \tag{2.1}$$

in which $\hbar$ is Planck constant $6.626\,070\,15 \times 10^{-34}\ \mathrm{m^2\,kg\,s^{-1}}$ divided by 2π, and I is the spin quantum number. This number plays a central role in the feasibility of MR methods in the characterization of the nucleus since, as implied from Figure 2.1, only the nuclei with $I \neq 0$ can emit MR signal, and the rest are not visible by this technique. Protons and neutrons have spin, in turn, and the quantum number of nuclei roots in these elementary particles, but there is no simple way to calculate it. However, the following cases hold regarding the quantum number of different elements with respect to the number of protons and neutrons [26].

- *Even number of protons and neutrons* $\Longrightarrow I = 0 \left(e.g.\ ^{16}O,\ ^{4}He\right)$.
- *Odd number of protons and neutrons* $\Longrightarrow I \in \mathbb{Z}^+ \left(e.g.\ I_{^{10}B} = 3,\ I_{^{2}H} = 1\right)$.
- *Others* $\Longrightarrow I \in \mathbb{Z}^+ - 1/2 \left(e.g.\ I_{^{1}H} = 1/2,\ I_{^{23}Na} = 3/2\right)$.

To put it succinctly, the spin of the elementary particles defines the spin quantum number I, which determines the spin angular moment ($\vec{S}$) based on Figure 2.1. In addition, spin magnetic moment ($\vec{\mu}$) is also caused by the spin of elementary particles. The ratio of ($\vec{\mu}$) to ($\vec{S}$) is called gyromagnetic ratio.

$$\gamma = \vec{\mu}/\vec{S}. \tag{2.2}$$

So, if the spin angular moment and spin magnetic moment are parallel, the gyromagnetic ratio would be positive, and if they are anti-parallel, then the ratio would be negative (Figure 2.1).

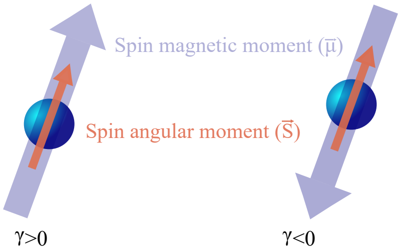

Figure 2.1: Effect of alignment of spin angular moment and magnetic moment on the gyromagnetic ratio.

The gyromagnetic ratio of some nuclei is listed in Table 2.1.

Table 2.1: Gyromagnetic ratio of different nuclei.

Nucleus	$\gamma \times 10^6$ $\mathrm{rad\,s^{-1}\,T^{-1}}$	$\gamma/2\pi$ $\mathrm{MHz\,T^{-1}}$	Nucleus	$\gamma \times 10^6$ $\mathrm{rad\,s^{-1}\,T^{-1}}$	$\gamma/2\pi$ $\mathrm{MHz\,T^{-1}}$
^1H	267.522	42.577	^{17}O	-36.264	-5.772
^2H	41.065	6.536	^{19}F	251.815	40.078
^3H	285.3508	45.415	^{23}Na	70.761	11.262
^3He	-203.789	-32.434	^{27}Al	69.763	11.103
^7Li	103.962	16.546	^{29}Si	-53.190	-8.465
^{13}C	67.283	10.708	^{31}P	108.291	17.235
^{14}N	19.331	3.077	^{57}Fe	8.681	1.382
^{15}N	-27.116	-4.316			

Even though inadequate, we can consider the spin as a tiny, never-resting spinning magnetic ball (Figure 2.2). As mentioned, spin is a pure quantum property, and there are many quantum complexities regarding the atomic building blocks

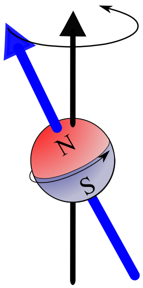

Figure 2.2: A simplified representation of the *spin* as a spinning magnetic ball. Although inaccurate, this representation is helpful in evaluating the spin behavior.

that form the spin. But, it is a helpful simplification to consider it as a spinning magnetic ball, as long as we don't use this consideration deeply.

2.1.1 Spin polarization

As shown in Figure 2.2, spin precesses around an axis. In the absence of any external magnetic field, the orientation of the axis is random, and the angular moments cancel each other out (Figure 2.3 a)) [2]. In the presence of an external magnetic field (B_0), spinning occurs around the axis of B_0 (z-axis by convention), resulting in a net magnetization in this direction (M_0) (Figure 2.3 b)). The process of positioning spins in two[3] opposite directions by applying an external magnetic field (B_0) is called *polarization*. The rotating axis of spins will be aligned with the direction of B_0.

As explained in Section 2.1, spin quantum number plays an important role in MR feasibility. In addition to the fact that nuclei with $I = 0$ are not detectable by MR techniques, this number determines the number of possible states of spin, which is equal to $2I + 1$. For instance, the hydrogen spin quantum number is $1/2$, resulting in 2 possible states for its nucleus. They are oriented parallel

---

[2] This assumption is true in the absence of spin-spin coupling. Otherwise, it is not true and has to be studied in the field of *zero field NMR*.

[3] This number is valid for nuclei with $I = 1/2$, e.g. H.

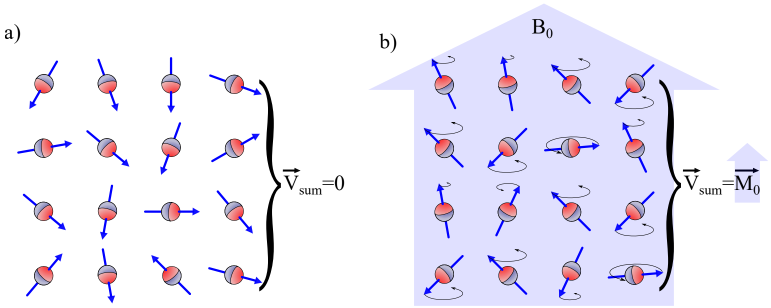

Figure 2.3: Spins orientation in the presence and absence of an external magnetic field (B_0).

and anti-parallel with respect to the direction of the external magnetic field and are called lower and higher energy levels, denoted by α and β, respectively. This phenomenon is called *Zeeman splitting*. Since the lower energy level is preferred by the majority of spins, there will be a net magnetization parallel with B_0, which is a function of the applied magnetic field,

$$\Delta E = E_{m_{down}} - E_{m_{up}} = \hbar \cdot \gamma \cdot B_0. \tag{2.3}$$

Planck-Einstein equation determines the relationship between energy and frequency,

$$\Delta E = \hbar \cdot \omega, \tag{2.4}$$

in which ω is called Larmor frequency. Comparing Equations 2.3 and 2.4, one can conclude the following relationship between Larmor frequency and external magnetic field,

$$\omega = \gamma \cdot B_0. \tag{2.5}$$

On the other hand, in order to characterize the probability of each state, the Boltzmann (or Gibbs) distribution can be used.

$$N_m = e^{-\frac{E}{K_B T}}, \tag{2.6}$$

where m is the quantum number which is equal to -1/2 for the higher energy level and 1/2 for lower energy level, K_B is Boltzmann constant ($1.38 \times 10^{-23}\,\mathrm{J\,K^{-1}}$), and T is the temperature. Finally, the net magnetization M_0, which is the magnetization difference between spins in lower and higher energy levels, for N number of spins at resonance can be calculated by the equation below ($I = 1/2$),

$$\vec{M}_0 = \Delta N \gamma \vec{S} = \frac{N B_0 \gamma^2 \hbar^2}{4 K_B T}. \tag{2.7}$$

As a brief presentation for this subsection, in the absence of any external magnetic field, spins are randomly aligned, canceling each other out. In the presence of B_0, they will be polarized parallel and anti-parallel with B_0, resulting in a net magnetization. The polarization would be enhanced by decreasing the temperature in Equation 2.7. Figure 2.4 gives us a graphical abstract of the current subsection.

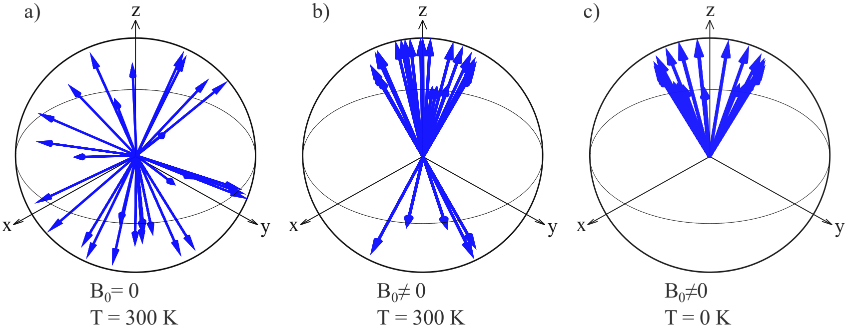

Figure 2.4: Spins orientation under different circumstances is shown. a) Absence of external magnetic field results in a random orientation and hence the net magnetization equal to zero. b) The presence of an external magnetic field in the z-direction leads to polarization of spins parallel and anti-parallel with the field. However, the majority stands parallel, which generates a net magnetization in this direction. c) In absolute zero (−273.15 °C), all spins are oriented parallel with the external magnetic field.

2.2 Magnetization evolution - Bloch equations

In order to evaluate any physical phenomena, first, we need to define the coordinate system in which the process is described. In MR, two coordinate systems, or reference frame, are used, namely *laboratory reference frame* and *rotating reference frame*, which both are *right-handed Cartesian coordinate system*. Compared to *laboratory reference frame*, *rotating reference frame* will be rotating around its z-axis at ω_0 frequency. So, if we look at the spin from *laboratory reference frame*, spin is precessing at γB_0, but if the spin is viewed from a *rotating reference frame*, it is spinning at $\gamma B_0 - \omega_0$, and in case γB_0 and ω_0 are equal, spin looks stationary from this reference frame. Magnetization evolution is mostly preferred to be assessed in the *rotating reference frame* since it simplifies the calculations.

2.2.1 Equilibrium, excitation, relaxation

Here, it is briefly explained how the net magnetization can be measured by an MRI machine. In practice, after putting the sample in the machine, we deal with the situation shown in Figure 2.4 b), which leads to a net magnetization denoted by M_0. In the absence of an RF field, this magnetization is pointed at the direction of B_0 (traditionally z-direction, which is called *longitudinal axis*). This situation, in which spins are fully polarized, is called equilibrium. If we put a coil around the sample and apply an RF pulse with a frequency close enough to Larmor frequency and perpendicular to B_0, the pulse leads to the resonance phenomena, tilting M_0 from z-direction to xy-plane (also called *transverse plane*). This process is called *excitation* and is shown in Figure 2.5 a) and c) from both laboratory and rotating reference frames, respectively. Also, the frequency of the RF pulse in the excitation is called *carrier frequency* (ω_{rf}). If we stop applying the pulse, the magnetization will go back to the equilibrium condition and will be polarized again. This process is called *relaxation* and is presented in Figure 2.5 b) and d).

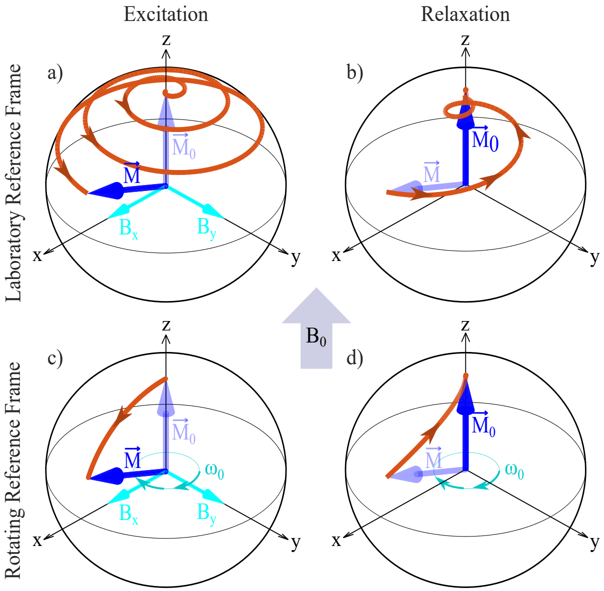

Figure 2.5: Trajectory of magnetization evolution during excitation and relaxation.

Magnetization evolution during the excitation and relaxation, which is demonstrated in Figure 2.5 follows the Bloch equation, named after Felix Bloch deciphered the following relationship between magnetization evolution, applied RF field, and external magnetic field. In the rotating reference frame, the Bloch equations can be written as the following,

$$\begin{pmatrix} \dot{M}_x \\ \dot{M}_y \\ \dot{M}_z \end{pmatrix} = \begin{pmatrix} -\frac{1}{T_2} & \Delta & -\gamma B_y \\ -\Delta & -\frac{1}{T_2} & \gamma B_x \\ \gamma B_y & -\gamma B_x & -\frac{1}{T_1} \end{pmatrix} \begin{pmatrix} M_x \\ M_y \\ M_z \end{pmatrix} + \begin{pmatrix} 0 \\ 0 \\ \frac{M_0}{T_1} \end{pmatrix}, \tag{2.8}$$

where, M_x, M_y, and M_z, are magnetization components in the corresponding index direction, Δ is the offset between the carrier and Larmor frequency ($\gamma B_0 - \omega_{\mathrm{rf}}$), T_1 is the spin-lattice relaxation time, T_2 is the spin-spin relaxation time,

B_x and B_y are x and y components of the RF pulse, γ is the gyromagnetic ratio of the nucleus under consideration, and M_0 is the steady state magnetization generated by spins (in the presence of B_0 and absence of any excitation pulse when $t \rightarrow \infty$).

Now that the excitation and especially relaxation phenomena are explained, we can describe how the MR signal is collected. During the relaxation process, the miniature magnetization M_0, which was already titled toward xy-plane during the excitation time, would be polarized again and go back to its equilibrium position, following the trajectory shown in Figure 2.5 b) and finally pointing upward in the z-direction. This means that there would be a precessing magnetization. So, if we put a coil around the sample, this precessing magnetization induces an electrical current, which is considered as the MR signal.

As implied by Figure 2.5 b) and d), in the absence of any excitation pulse, the signal decays over the relaxation time. That is why, in MR, it is called free induction decay (FID). Also, the angle between the z-axis and magnetization at the end of the excitation time, or beginning of the relaxation time, is called the Flip angle and is mostly shown by α. In order to have a better understanding of the relaxation phenomenon, the behavior of longitudinal (M_z) and transverse (M_{xy}) components of the magnetization during the relaxation is illustrated in Figure 2.6.

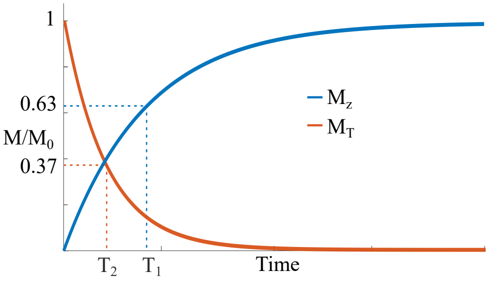

Figure 2.6: Illustration of free induction decay (FID), spin-lattice (or longitudinal) relaxation time T_1, and spin-spin (or transverse) relaxation time T_2. M_T is the euclidean norm of $M_x + i\,M_y$ and is called transverse magnetization.

In this figure, the Flip angle is considered equal to 90°. Also, two important concepts in MR, namely longitudinal and transverse relaxation times (T_1 and T_2 respectively) are shown. Based on a conventional definition, the required time to recover 63% of the longitudinal magnetization (M_z) is called spin-lattice or longitudinal relaxation time (T_1). The time in which the transverse magnetization loses the same percent (or, in other words, drops to 37% of its initial value) is called spin-spin or transverse relaxation time (T_2).
The whole process of excitation and acquisition consists of some actions and delays, and for obvious reasons, the chronology of them matters. The way all of these actions and delays are applied to generate and collect the MR experiment is called *pulse sequence*. A graphical illustration highly helps us to understand a pulse sequence. In the following, the simplest pulse sequence is presented in Figure 2.7. The pulse sequence is called *single pulse* and consists of a single excitation and one acquisition.

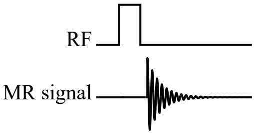

Figure 2.7: Graphical illustration of a *single pulse* pulse sequence.

2.2.2 Refocusing

After the excitation, the signal attenuates due to three main reasons: longitudinal relaxation, transverse relaxation, and the inhomogeneity of the magnetic field[4]. To compensate for the latter, a refocusing pulse can be used. It is a 180° RF pulse, which flips the magnetization by 180 degrees. In an inhomogeneous field, spins experience different values of B_0, which changes the frequency of the spins. Some would be precessing faster, some slower. As a result, they will be dephased. In this case, the signal decays even faster than in ideal conditions.

---

[4] In the absence of any displacement.

This phenomenon is illustrated in Figure 2.8. Another important concept in MR, namely effective transverse relaxation time (T_2^*), is shown in the figure.

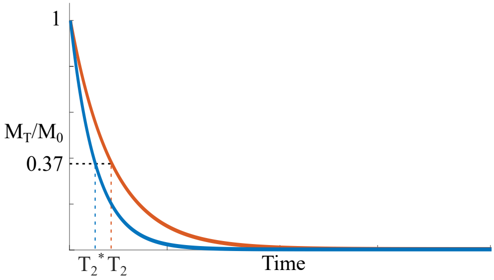

Figure 2.8: Illustration of free induction decay (FID) in a homogeneous and inhomogeneous B_0 field. Effective transverse relaxation time (T_2^*) is indicated in the figure.

The problem of faster decay due to inhomogeneity can be minimized by applying a refocusing pulse[5]. It is applied after a certain delay (τ) after the excitation and flips the magnetization. As a result, it puts the slower spins ahead of the faster ones. Consequently, after the same time delay (τ), they will be in phase again, and hence magnetization is refocused. The signal is called an echo, and the technique is called Hahn spin-echo. All steps of a Hahn spin-echo are shown in Figure 2.9.

2.3 Nuclear magnetic resonance (NMR)

In order to explicate NMR, we get back to the Bloch equation (Equation 2.8). After the excitation, tilted magnetization goes through the relation process and gets back to the equilibrium. It induces the MR signal in the coil. During the relaxation process, B_x and B_y are equal to zero. Also, the Flip angle is considered equal to 90°, which would define the initial condition of the equations. In addition, the initial phase of the signal is assumed equal to zero, and $\Delta = \omega$. In these conditions, the following would be the solution to the Bloch equation,

---

[5] There can be a number of refocusing pulses depending on the application.

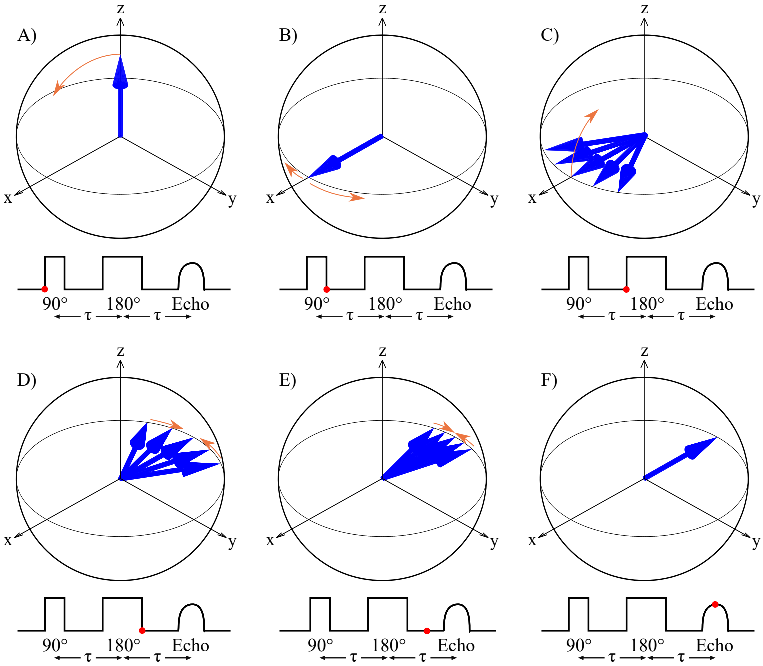

Figure 2.9: Schematic representation of a Hahn spin-echo. A) The first step is the excitation. B) After the excitation, spins start dephasing. C) After a certain delay (τ), the 180° refocusing pulse is applied, which flips the magnetization. D) At the end of the refocusing pulse, slower spins are ahead of the faster ones. E) Over time, they will be more in phase. F) After the same delay (τ), they will be all in phase, and the summation signal will experience its maximum.

$$\begin{cases} M_x = M_0 \cos(\omega t) e^{-t/T_2}, \\ M_y = M_0 \sin(\omega t) e^{-t/T_2}, \\ M_z = M_0 \left(1 - e^{-t/T_1}\right). \end{cases} \tag{2.9}$$

In other words, the following would be the MR signal observed by the spectrometer,

$$M_T = M_x + iM_x = M_0 e^{j\omega t} e^{-t/T_2}. \tag{2.10}$$

There are two important keys in the abovementioned equation. First, as mentioned in Table 2.1, different nuclei have distinct gyromagnetic ratios and hence non-identical frequencies (ω). So, the frequency of the signal tells us the type of nucleus from which the signal is emitted. Second, the magnitude of the signal talks about the number of nuclei, elucidating the amount, or the density, of the specific nucleus. These two keys are the principle of many MR applications, including NMR and MRI.

Figure 2.10 implies that the transverse signal exponentially decays. In Figure 2.10 a), the x and y (real and imaginary) components of the signal are shown. In order to decipher the type of nucleus, we need to check the frequency of the signal. So, a Fourier transformation (Figure 2.11) will be applied to the collected signal in order to transfer the signal from the time domain to the frequency domain.

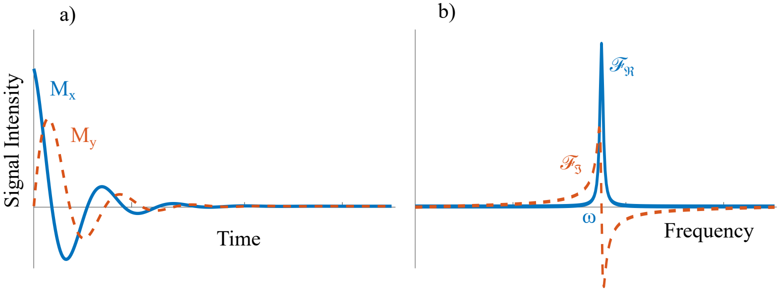

Figure 2.10: Real and imaginary parts of an MR signal in time (M_x, M_y) and frequency domain $(\mathscr{F}_{\Re}, \mathscr{F}_{\Im})$.

$$M(\omega) = \int_{-\infty}^{\infty} M(t)\, e^{-j\omega t}\, dt. \tag{2.11}$$

As depicted in Figure 2.10, the x and y components of the MR signal constitute the real and imaginary parts of the signal in the time domain. Applying a Fourier transformation on this complex vector (Figure 2.11) transforms the collected data to the frequency domain, in which ω shows the frequency of the signal, which reveals the type of the nucleus. In order to make the concept of NMR more clear, here we discuss a case in which there are two distinct nuclei with different frequencies (ω_1 and ω_2). Suppose we perform a separate experiment on each of the two samples containing each nucleus. In that case, the spectrometer delivers the results shown in Figure 2.11 a) and corresponding spectra, Figure 2.11 b). But, if we perform an experiment on a sample including both nuclei, the signal would be the summation of both signals, Figure 2.11 c), and the corresponding Fourier transformation reveals the frequency of both of them, Figure 2.11 d).

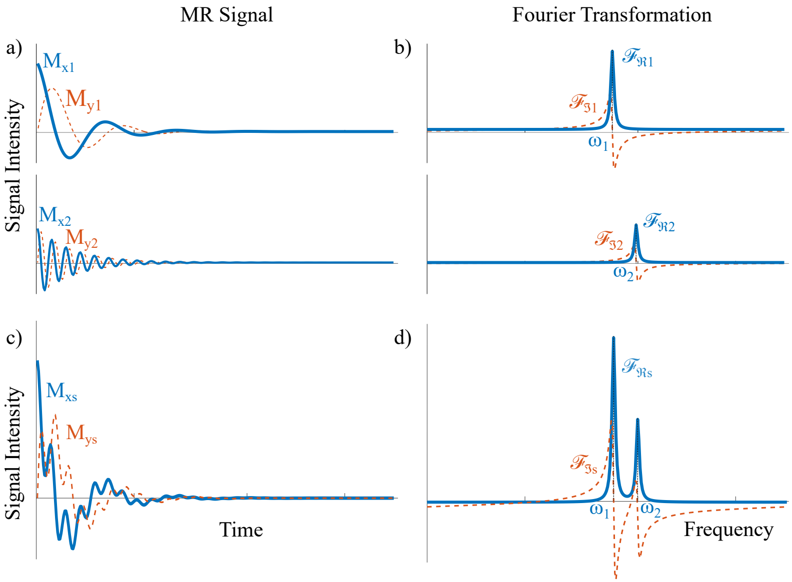

Figure 2.11: Real and imaginary parts of an MR signal in time (M_x, M_y) and frequency domain $(\mathscr{F}_\Re, \mathscr{F}_\Im)$.

That is how NMR can reveal the atomic structure of a sample. This feature ranks NMR among spectroscopic techniques with atomic resolution, which benefits us in different scientific fields, such as chemistry, physics, biology, and materials science.

2.3.1 Chemical shift

As explained in the last section, NMR is able to distinguish the amount of nuclei with different precessing frequencies. The frequency is in a direct relationship with the gyromagnetic ratio and magnetic field experienced by the nucleus (Equation 2.5). While the gyromagnetic ratio is a physical property of a nucleus, the magnetic field experienced by nuclei can be slightly different from the external magnetic field applied by the spectrometer. The reason is the local magnetic field as a result of the structure of the atom. The change in the local magnetic field results from two main reasons: deshielding and anisotropy. A comprehensive explanation of these concepts is out of the scope of this study, but here, a short description is presented.

Regarding de/shielding, the electrons surrounding the proton generate a magnetic field in the opposite of the external magnetic field, B_0, which decreases the magnetic field running into the nucleus. In other words, they shield the proton. So, the chemical shift is smaller for the nuclei with higher electron density. In addition, if there are electronegative groups[6] in the neighborhood, they can reduce the chemical shift since, due to their attraction for electrons, they reduce the density of electrons and lead to deshielding.

Anisotropy happens when the interaction of electrons with the external magnetic field results in a non-uniform magnetic field. In such a case, there will be three different magnetic fields around the electrons (Figure 2.12). Depending on the location of the proton, it can increase or decrease the frequency or has no effect on that.

Chemical shift slightly changes the precession frequency (in the order of a few Hertz in a 1 T external magnetic field). It is, in fact, a function of the field. Higher magnetic fields increase the range of change in frequency due

---

[6] Electronegativity refers to the ability of the atom to attract shared electrons in a chemical bond.

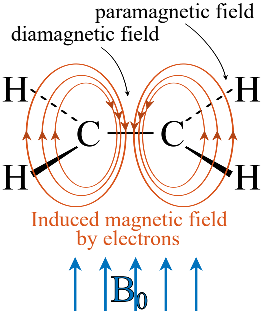

Figure 2.12: Magnetic field induced by electrons causes a diamagnetic effect between bonded atoms and a paramagnetic effect outside of that area. The latter results in deshielding, and the former causes shielding.

to chemical shifts. In order to make it independent of the magnetic field and make it easier for any comparison, conventionally, chemical shift is mentioned in parts per million (ppm) instead of Hz and follows the equation below,

$$\delta = \frac{\nu - \nu_{\mathrm{ref}}}{\nu_{\mathrm{ref}}} \times 10^6, \tag{2.12}$$

in which δ is chemical shift in ppm, ν is the precession frequency, and ν_{ref} is the reference frequency.

2.4 Magnetic resonance imaging (MRI)

In the former section, it was explained how NMR can decipher the quantity and type of the nuclei in a sample. In this section, we describe how this attribute can be used to have a comprehensive image of the internal structures of the sample. NMR is capable of providing us with a signal that represents the number of spins of each chemical compound in a sample, but the signal comes from the whole sample. In order to have an image from the sample, we need to know the signal emitted from each volume element. The spatial encoding technique enables us to venture from NMR into MRI. MRI was first introduced in 1973 [27], where P.C. Lauterbur employed induced local interactions to take the image of a sample. In this study, he showed how a secondary magnetic field restricts the contribution of spins to a limited volume. This technique, called spatial encoding, provides the opportunity to uncover the contribution of each voxel in the MR signal.

2.4.1 Spatial encoding

Spatial encoding is based on gradient encoding techniques. In fact, gradients will be applied in three different directions and in a highly targeted manner to distinguish the signal coming from each volume element. In the following, each part of this technique is explained separately.

Excitation pulse, slice selection gradient (G_{ss})

The first gradient in the spatial encoding gradient technique is called slice selection gradient (G_{ss}) and is applied coupled with a selective RF excitation pulse. The excitation pulse is conventionally a modified version of the sinc pulse and has a certain bandwidth. The gradient changes the Larmour frequency of spin along the gradient direction. As a result, only the spins whose frequency is within the bandwidth of the pulse undergo the resonance phenomena, and therefore, just this certain slice will be excited. A graphical representation is shown in Figure 2.13. In this figure, the slice selection is performed in the z-direction.

The bandwidth of the excitation pulse and strength of the slice selection gradient define the thickness of the excited sample. As an instance, coupling of an excitation pulse with 10 Hz of bandwidth and a slice selection gradient with the strength of $5\,\mathrm{Hz\,mm^{-1}}$ excites a slice of the sample with 2 mm.

Phase encoding gradient (G_{ph})

Having excited a spatially selected slice, we can start the second step of spatial encoding, called *phase encoding*. So far, the targeted slice is excited, but still,

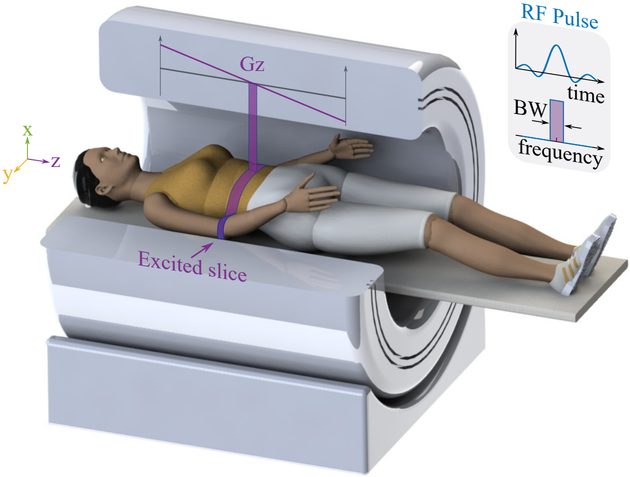

Figure 2.13: Slice selection achieved by applying a magnetic field gradient (in addition to B_0) in the corresponding direction (here z) (Modified from Leon Maryasin [28]).

we are not able to distinguish the signal from each voxel of the slice. The goal of this step is to make the signal from each row of the sample unique by encoding the phase of the signal in this orientation; let us consider it as the y-axis. To do so, the gradient will be temporarily on in the y-axis direction. It gives a unique phase to each row of the sample (Figure 2.14). This process is called *phase encoding*. It is worth mentioning that since the phase encoding gradient is off at the end, spins will be spinning at the same frequency after G_{ph} (in the absence of field inhomogeneity and chemical shift offset).

Field of view (FOV) refers to the physical extent of the image. In the direction of phase encoding, it can be calculated by the following equation,

$$\mathrm{FOV}_p = \frac{N}{\gamma G_{\mathrm{ph}} t_p}, \tag{2.13}$$

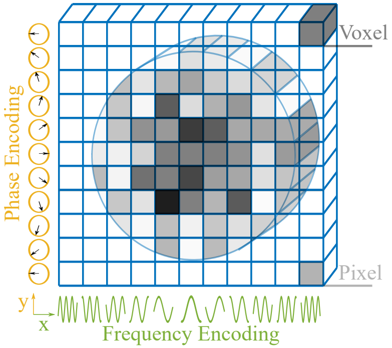

Figure 2.14: Phase and frequency encoding, applied in two orthogonal directions, make the signal emitted from each voxel distinguishable. This process is called *spatial encoding*.

in which N is the number of voxels in the phase encoding direction, G_p is the amplitude of the phase encoding gradient, and t_p is the time of applying gradient.

Frequency encoding gradient (G_{fr})

In the last step, the MR signal was encoded in the y direction by phase encoding gradient. In this step, the signal will be encoded along the x-axis by encoding the frequency of the signal. The frequency encoding step would be performed concurrently with signal acquisition, which is why it is called *readout gradient* as well. Starting with the MR signal acquisition, a gradient will be applied perpendicular to phase encoding orientation, which changes the frequency of the signal along this axis (here, x-axis). Figure 2.14 demonstrates a graphical representation of phase and frequency encoding steps.

The number of collected points in the signal acquisition is the same as the number of voxels in the frequency encoding direction. The corresponding field of view (FOV) can be obtained by the following equation,

$$\mathrm{FOV}_f = \frac{\Delta f_{\mathrm{acq}}}{M\gamma G_{\mathrm{fr}}}, \tag{2.14}$$

in which Δf_{acq} is the receiver bandwidth, M is the number of voxels in the frequency encoding direction, and G_f is the amplitude of the frequency encoding gradient.

2.4.2 Image reconstruction

The transformation from signal to image is based on the definition of the Fourier transform operator. It transforms a function from time to frequency domain (and vice versa). This operator is even used intrinsically by the human senses. When you are hearing an array of sounds, each of them has a certain pitch (or frequency). Your sense of hearing can filter out and distinguish each of them. This is simply a natural Fourier transform operator. The same holds for the lights. In MRI, we benefit from this concept. The idea of phase and frequency encoding was explained in the last subsection. All voxels contribute to the net signal collected by the spectrometer, but the encodings assign a unique phase and frequency to the contribution of each voxel. The contribution can be decoded by Fourier transformation.

An image can be considered as an $N \times M$ matrix. N is the number of voxels in the y direction (G_p), and M is the size along the x-axis (G_f). As explained in subsection "**Frequency encoding gradient ($\mathbf{G_{fr}}$)**", in the signal acquisition, M number of data points are collected. So, in order to decode the encoded data of $N \times M$ voxels, one has to collect the MR signal N times with different phase encoding gradients. These signals fill out our data matrix in the spatial frequency domain, called *k-space*. A two-dimensional Fourier transformation (FT) of the *k-space* gives us the corresponding data in the spatial domain, which is the image itself. In fact, the FT consists of complex numbers whose absolute value gives us the magnitude of the signal emitting from each voxel, and its phase gives us the phase of the signal. Since the signal is emitted from the spins, the magnitude represents their density in each voxel. So, the absolute value gives us an image of the nuclei density. Regarding the applications of the phase of the signal, there are many applications, including susceptibility-weighted imaging (SWI), functional MRI (fMRI), flow MRI, and so on, among which flow MRI will be discussed.

The order of applying pulses, gradients, delays, and data collection is called *pulse sequence*. A very widely used one, called FLASH, is represented in Figure 2.15.

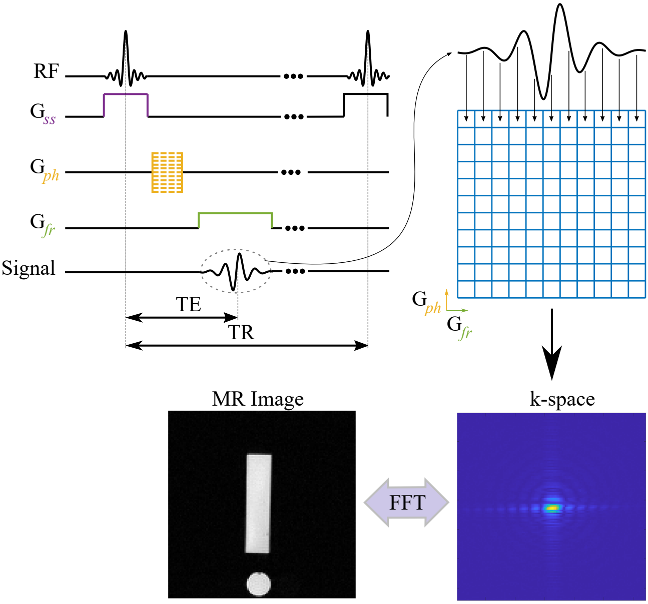

Figure 2.15: Graphical illustration of a FLASH (Fast Low-Angle SHot) pulse sequence, including an RF excitation pulse, a slice selection, a phase encoding, and a frequency encoding gradient. Also, two fundamental terms, the echo time (TE) and the repetition time (TR), are shown.

It is noteworthy that all we need to have the image is to fill the k-space[7]. But, filling it the way it is done in FLASH is unnecessary. To recall, in the FLASH pulse sequence, one row of the k-space would be filled after each excitation. But, there are many alternative methods available to perform it. Three of them,

---

[7] Even a complete filling of the k-space matrix is not necessary. There are some techniques to produce the image from a partially filled k-space.

including Echo planar imaging (EPI), Spiral, and Radial techniques, are shown and compared with that of FLASH Figure 2.16.

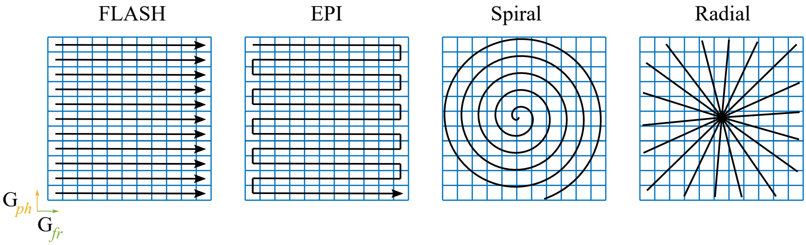

Figure 2.16: Different k-space sampling orders, including two Cartesian (FLASH and EPI) and two non-Cartesian (Spiral and Radial) methods.

Also, the graphical representation of the corresponding pulse sequence is shown in Figure 2.17.

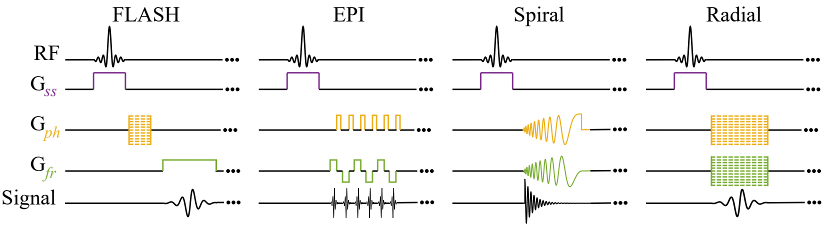

Figure 2.17: Corresponding gradients for different k-space sampling orders presented in Figure 2.16.

2.5 Magnetic resonance velocimetry (MRV)

Comprehending fluid flow phenomena is one of the crucial challenges in engineering. A thorough understanding of these dynamics has the potential to significantly improve various industrial processes. There are several methods in MR that enable one to acquire a velocity map of the sample. Here, a brief explanation of each one is provided. Conventionally, flow MRI pulse sequences are divided into three main categories: black blood angiography, time of flight

(TOF) and contrast-enhanced MR angiography (CEMRA), and phase contrast (PC). All of these techniques are based on imaging pulse sequences and are basically a modified version of them. Still, they are designed to provide a velocity map instead of a density map.

2.5.1 Black blood angiography

As the name implies, this method is based on the attenuation of the signal coming from the moving sample while preserving the signal from the stationary part. There are a number of techniques to perform this job. Some are based on the presaturation pulses to eliminate signals from a certain volume. These pulses are just 90° spatially selective pulses, but in the opposite of the excitation or refocusing ones, they are designed to maximize phase dispersion in the region of interest, and they don't precede refocusing gradients. Another technique is based on 180° refocusing pulses. In fact, in any pulse sequence which contains a refocusing pulse, this method can be implemented. The idea is straightforward. Stationary samples experience both pulses (90° and 180°), while the moving ones experience only the first one. While the second one is being applied, they are off-resonance (out of exciting slice). The third technique is the inversion recovery (IR) method. It is based on the longitudinal relaxation process. In this technique, the imaging sequence is preceded by a 180° excitation pulse and a certain delay, called inversion time (TI). The value of TI is chosen such that the signal coming from blood is at the xy-plane at the beginning of the imaging sequence and, hence, suppressed. The last technique is susceptibility-weighted imaging (SWI), which works based on the direct relationship between deoxyhemoglobin and effective transverse relaxation time (T_2^*) of the sample. A number of aforementioned methods can be used together in a pulse sequence to prepare a venogram. In the following, some pulse sequences in black blood angiography are explained.

Rapid Acquisition with Relaxation Enhancement (RARE) sequences

RARE pulse sequences benefit from the 180° refocusing pulses to provide a venogram. In fact, the brightness of voxels depends on the movement of the voxel between the 90° excitation and 180° refocusing pulses. If the voxel is stationary, an ideal excitation would happen. And if the voxel goes out of the excited slice, signal attenuation is expected. If we consider a single-echo pulse sequence, in which the delay between two pulses is TE/2, signal loss is expected when the velocity component perpendicular to the slice direction goes beyond the following value,

$$v_{\perp} = \frac{2\Delta z}{\mathrm{TE}}, \tag{2.15}$$

in which Δz is the thickness of the excited slice. For a double-echo pulse sequence, at the time applying the second refocusing pulse, the excited slice would be out of the exciting area if the velocity exceeds,

$$v_{\perp} = \frac{2\Delta z}{\mathrm{TE}_1 + \mathrm{TE}_2}, \tag{2.16}$$

in which TE_1 and TE_2 are, respectively, the echo time of the first and second refocusing pulses. Also, adding a presaturation technique to the RARE pulse sequences can enhance the performance of the black blood angiography.

Inversion recovery (IR) sequences

Inversion recovery pulse sequences rely on the longitudinal relaxation process, and therefore, T_1 plays an important role in such sequences. A single inversion recovery pulse sequence starts with a 180° inversion RF pulse, preceding an imaging pulse sequence. As shown in Figure 2.18, the idea is to invert the magnetization and, after a certain delay, called the inversion time (TI), excite the whole sample. Depending on the TI, when the 90° excitation pulse is applied, a certain component of the tissue is located on the transverse plane. Therefore,

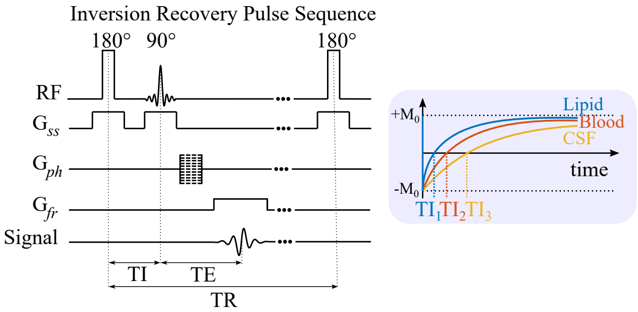

Figure 2.18: Single inversion recovery pulse sequence. Important delays, including the inversion time (IT), the repetition times (TR), and the echo time (TE) are shown.

it won't generate any signal. For instance, if the TI is set to that of blood, this technique suppresses its signal. Required TI to suppress each tissue depends on the T_1.

Double inversion recovery (DIR) sequences

The flaw of the inversion recovery method is that the stationary tissues with the same T_1 will be suppressed as well. This issue is reduced by double inversion pulse sequences. Compared to the single inversion method, a selective 180° pulse is added right after the hard one (Figure 2.19). During the first pulse, the signal in the whole sample will be inverted. Thereafter, the selective 180° pulse restores the magnetization within the slice. After a certain delay (TI), the magnetization of a certain component (i.e., blood) in the rest of the sample will be nulled. This can give us a visualization of the flow map since the inflow that has the targeted TI comes to the slice and the exciting region. But since it is already nulled, it appears in black in the image. If the sample is stationary, then it generates a signal. As a result, the loss of signal is expected at velocities greater than

$$v_{\perp} = \frac{\Delta z}{\mathrm{TI}}. \tag{2.17}$$

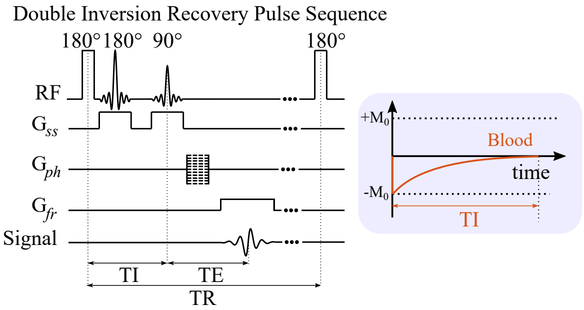

Figure 2.19: Double inversion recovery pulse sequence. Important delays, including the inversion time (TI), the repetition time (TR), and the echo time (TE), are shown.

Triple inversion recovery (TIR) sequences

TIR is an extended version of DIR. In DIR, only one component (i.e., blood) is suppressed. As shown in Figure 2.20, in TIR, the hard 180° pulse precedes two slice selective 180° pulses, resulting in the suppression of two components with two distinct T_1, mostly blood and fat. The performance of this pulse sequence is highly dependent on two delays, called TI_a and TI_b. TI_a is the delay between the first 180° and the beginning of the imaging pulse sequence (the 90° excitation pulse). TI_b is the delay the last 180° and the beginning of the imaging pulse sequence. These delays will be chosen based on the targeted value of T_1.

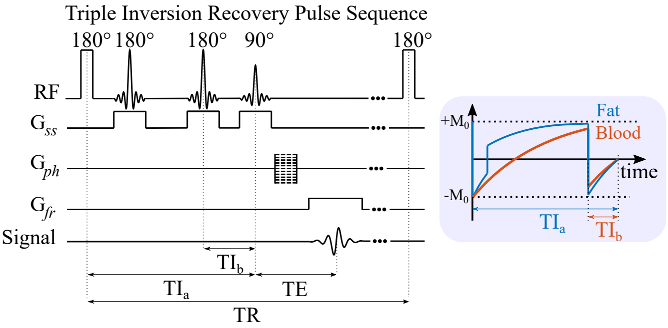

Figure 2.20: Triple inversion recovery pulse sequence. Important delays, including the inversion times (TI_a and TI_b), the repetition time (TR), and the echo time (TE), are shown.

Susceptibility weighted imaging (SWI)

SW images are very applicable in flow imaging, especially when it comes to blood flow experiments. Deoxyhemoglobin has a short T_2^*. So, if the image is taken by a long TE, it results in a T_2^* weighted image due to loss of signal as a result of short T_2^*. Due to the effect of susceptibility on the phase of the images, this technique benefits from a phase map as well. A high-pass filter will be applied on the phase map in order to remove the effect of any low-frequency distortion caused by other sources (i.e. B_0 inhomogeneity) other than the magnetic susceptibility. The resultant image will be used as a mask on the density/magnitude image to enhance the flow suppression and improve the contrast between blood and other tissues.

2.5.2 Time of flight (TOF) and contrast-enhanced MR angiography (CEMRA)

In opposite of black blood angiography, TOF and CEMRA are based on enhancing the signal coming from the blood. So, they provide white images from the vessels. The first method, TOF, works based on the effect of inflow to refresh the sample in the excited slice. After any excitation, it takes a while for the sample to polarize again along the longitudinal axis, conventionally z. So, if the next excitation is applied before this time, it excites a partially polarized magnetization, and therefore the signal attenuates. But in the case of flow, depending on the velocity, a part of the sample (or even the whole sample) would be replaced by fresh polarized spins, and the signal would be enhanced. This phenomenon is called Flow Related Enhancement (FRE). Employing the effect of FRE, TOF provides MR images with enhanced signals within the moving regions (i.e., vessels).

If we consider a stationary sample under a spoiled gradient echo pulse sequence, the MR signal after enough number excitations for reaching a steady-state condition can be calculated from the following equation [22],

$$S = \frac{M_0 \sin\theta \left(1 - e^{-\mathrm{TR}/T_1}\right)}{1 - \cos\theta \; e^{-\mathrm{TR}/T_1}} e^{-\mathrm{TE}/T_2^*} \equiv M_0 \sin\theta \; f_{z,ss} \; e^{-\mathrm{TE}/T_2^*}, \tag{2.18}$$

in which, S is signal, θ is the flip angle, M_0 is longitudinal magnetization in equilibrium, and $f_{z,ss}$ is dimensionless steady-state longitudinal magnetization. Two important facts can be concluded from Equation 2.18.

First, there is a certain value of θ at which the signal reaches its maximum. This angle is called the Ernst angle and can be obtained from the following equation,

$$\theta_E = \arccos\left(e^{-\mathrm{TR}/T_1}\right). \tag{2.19}$$

The corresponding graph for Equation 2.19, for $\mathrm{TR}/T_1 = 0.025$, is plotted in Figure 2.21. As shown, the Flip angle to have the maximum steady-state signal is 12.8°.

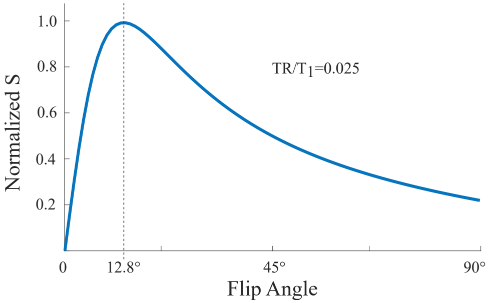

Figure 2.21: Steady-state signal for different values of Flip angle ($\mathrm{TR}/T_1 = 0.025$).

In conclusion, the signal attenuates when the Flip angle gets bigger than θ_E.

The second conclusion is that TR is in a monotonic, non-decreasing relationship with the signal intensity, meaning that, to some extent, increasing TR enhances the intensity. In other words, short TR results in signal attenuation due to the saturation. In case of flow, the saturated sample will be replaced by a fresh one and compensate for the effect of saturation. This is the principle of the TOF. This relationship between signal enhancement and flow holds until the sample is completely refreshed by the flow. If we increase the flow velocity further, it doesn't enhance the magnitude anymore. In fact, it might even decrease it due to dephasing within the voxels. So, the maximum measurable velocity by this method is the velocity at which the sample in the whole thickness is replaced by a fresh sample during the repetition time and can be obtained by the following equation,

$$V_{\max} = \frac{\Delta z}{\mathrm{TR}}. \tag{2.20}$$

Figure 2.18 can be further generalized. Depending on the velocity of the sample, spins that are within the excited slice during the first excitation go through a limited number of consecutive excitations. If spins in the slice go through j number of excitations, the signal can be calculated by the following equation,

$$S_j = M_0 \sin\theta \left[f_{z,\mathrm{ss}} + \left(cos\theta \; e^{-\mathrm{TR}/T_1} \right)^{j-1} \left(1 - f_{z,\mathrm{ss}} \right) \right] e^{-\mathrm{TE}/T_2^*}. \tag{2.21}$$

If $j \longrightarrow \infty$, Equation 2.21 turns to the form of Equation 2.18. So, an increase in the number of excitations results in a steady-state signal. That is the logic of having a number of dummy scans at the beginning of some pulse sequences to have a steady-state signal in all acquisitions.

In the absence of any flow, Equation 2.21 goes through an infinite number of iterations. In the presence of flow, the number of experienced excitations would be limited. Based on this fact, FRE, which is basically the increase in signal due to flow, is the signal difference between these two conditions. As a result, FRE can be calculated by the following equation,

$$\mathrm{FRE} = S - S_j = M_0 \sin\theta \; \left(cos\theta \; e^{-\mathrm{TR}/T_1} \right)^{j-1} \left(1 - f_{z,\mathrm{ss}} \right) e^{-\mathrm{TE}/T_2^*}. \tag{2.22}$$

In fact, Figure 2.22 gives us the Ernst angle for a flowing sample. This equation is plotted in Figure 2.22 for five different cases in which the sample experiences 1, 2, 4, 7, and 10 excitations. In this figure, the ratio of TR/T_1 is 0.025.

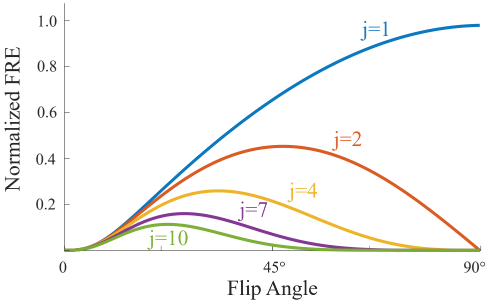

Figure 2.22: Flow related enhancement (FRE) for five different numbers of excitations, j=1, 2, 4, 7, 10 ($\mathrm{TR}/T_1 = 0.025$).

In Figure 2.22, j can be considered as an indicator of the flow rate. In fact, a higher flow rate leads to a smaller number of excitations. As shown in the figure, for any certain flow rate, there is a specific Flip angle to have the best signal enhancement. The greater the flow rate (equivalent to a smaller j), the greater the Flip angle is.

This method is divided into three main versions: two-dimensional TOF (2DTOF), three-dimensional TOF (3DTOF), and multiple overlapping thin-slab acquisition (MOTSA). 2DTOF divides the target volume into a number of 2D slices, while 3DTOF acquires 3D volumetric images. Each method has its own advantages and disadvantages.

In 3DTOF, weaker gradients are required to reach thin slices. It not only reduces the power of gradient oscillation but also results in shorter values of TE and, hence, intravoxel dephasing reduction. On the other hand, 2DTOF leads to a higher value of FRE since slices in a certain volume would be excited separately; therefore, they go through a smaller number of excitations compared to 3DTOF, in which the whole volume would be excited. MOTSA can be considered as a combination of the first two methods, in which the volume is divided into a number of slabs, and each slab is treated as a 3D volume. This method enables one to benefit from the advantages of both methods.

In addition to TOF, contrast-enhanced MR angiography (CEMRA) provides MR images in which the signal from the blood is enhanced. The difference between them is that the signal from CEMRA is not enhanced due to flow. Instead, the enhancement is achieved by adding a contrast agent to the blood and shortening its T_1 compared to the rest of the sample. As a result, acquiring 3D images with relatively short TR results in suppression of signal in the rest of the sample while the signal coming from the blood is still strong due to shorter longitudinal relaxation time (T_1). As implied by the explanation, signal enhancement is independent of the flow rate.

2.5.3 Phase contrast flow MRI (PC-MRI)

In the last section, it was explained that MR images are obtained by calculating the absolute value of the Fourier transformation (FT) of k-space. However, the phase of the FT has its own specific applications and contains invaluable information about the sample. Depending on the pulse sequence, the phase of the image can be used to decipher specific characteristics of the sample, including temperature, elasticity, and velocity. Magnetic resonance velocimetry (MRV), also called phase contrast flow MRI (PC-MRI), is in the interest of this study and will be explained in the following.

PC-MRI is based on the application of flow encoding bipolar gradient, which will be explained in the following.

Bipolar flow encoding gradient

Bipolar flow encoding gradient, or *Bipolar motion sensitizing gradient*, or just *bipolar gradient*, consists of two gradient lobes with the same amplitude but the opposite polarity. Each lobe injects a certain phase depending on the gyromagnetic ratio, magnitude, duration, and position of the voxel with respect to the isocenter of the gradient. Since the gyromagnetic ratio, magnitude, and duration are the same for both lobes, the only effective parameter on the injected phase is the location. For a stationary sample, the position is also the same. So, the injection and loss of phase will be the same, and the remaining phase will be zero. But, if a voxel is moving, the position of the voxel would be different for each lobe. So, there will be a remaining phase at the end. The amount of the phase depends on the difference in the position of the voxel in each lobe. In conclusion, the phase depends on the movement of the voxel between the lobes. This means that the phase is a function of velocity. To put it succinctly, applying a bipolar gradient makes the phase of the voxel an indicator of its velocity. This process is called *velocity* or *flow encoding*. In fact, velocity will be encoded in the MR phase. Figure 2.23 shows how a bipolar gradient can perform the encoding process.

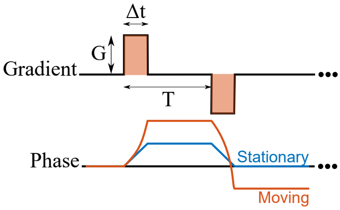

Figure 2.23: Flow encoding bipolar gradient technique. Important parameters, including the gradient strength G, the time of gradient oscillation Δt, and the gradients delay T, are shown.

By using a 180° refocusing pulse, flow encoding can be established by a similar technique called pulsed gradient spin echo (PGSE). In this method, the gradients are applied in the same direction. It is shown in Figure 2.24.

In the following, a mathematical description of flow encoding is presented. It was mentioned that the injected phase is a function of gyromagnetic ratio, magnitude, duration, and position. So, the following equation holds to calculate the phase,

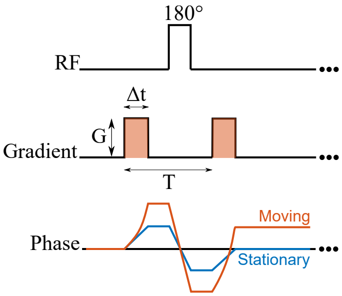

Figure 2.24: PGSE flow encoding technique. Important parameters, including the gradient strength G, the time of gradient oscillation Δt, and the gradients delay T, are shown.

$$\phi = \gamma \int_0^t G(t) \cdot x(t) dt = \gamma \left(m_0 x_0 + m_1 v_0 + \frac{1}{2} m_2 a_0 + \frac{1}{6} m_3 j_0 + \frac{1}{24} m_4 s_0 + \cdots \right), \tag{2.23}$$

where γ is gyromagnetic ratio, t is time, G is gradient, x is the position, m_n is the nth moment of gradient, and x_0, v_0, a_0, j_0, and s_0 are the initial position, velocity, acceleration, jerk, and snap respectively.

Since bipolar gradient consists of two lobes with the same magnitude and opposite polarity, m_0 in Equation 2.23 will be zero. If we assume that the derivatives of position higher than the first order are negligible, Equation 2.23 for bipolar gradient shown in Figure 2.23 can be rewritten in the following form,

$$\phi = \gamma m_1 v = \gamma G \Delta t T v. \tag{2.24}$$

$G \Delta t$ is the area under the gradient shown in Figure 2.23. So, Equation 2.24 can be written in the following form,

$$\phi = \gamma A T v. \tag{2.25}$$

In the experimental condition, some imperfections can affect the injected phase, i.e., magnetic field inhomogeneity. In order to remove the adverse effect on the phase map, *toggling* technique is used. In this technique, the experiment will be repeated again with the same parameters, yet with a bipolar gradient in the opposite direction. In the first experiment, the bipolar gradient consists of a positive and then a negative gradient $(+/-)$, but in the second one, first, it has a negative and then a positive gradient $(-/+)$. This technique is shown in Figure 2.25.

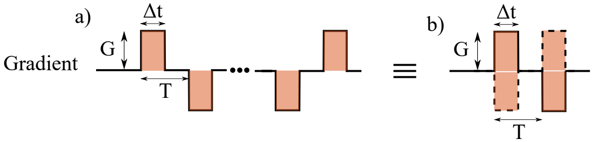

Figure 2.25: Toggling, as a technique to remove the unwanted phase. It consists of two measurements with the opposite precedence of positive and negative lobes. The toggling technique normally is shown in the second form (b).

After applying the toggling technique, the acquired signal will be subtracted from each other, and the resultant m_1 is the subtraction of both values of m_1. It is called Δm_1.

Bipolar gradient encodes velocity into the MR phase in a linear manner and based on Equation 2.25. Phase is always limited in the range of $[-\pi, \pi]$, which confines the measurable range of velocity. Based on this fact, the term V_{enc} is defined. V_{enc} is the maximum velocity that is expected to be encountered in the flow system. In fact, G, Δt, and t should be chosen such that $v = V_{enc}$ leads to $\phi = \pi$ in Equation 2.24. Any velocity greater than V_{enc} leads to aliasing. As an example, if $V_{\text{enc}} = 12\,\text{mm}\,\text{s}^{-1}$, phase of a voxel with the velocity of $14\,\text{mm}\,\text{s}^{-1}$ will be $7\pi/6$. Since phase is limited in the range of $[-\pi, \pi]$, the phase will be shown equal to $-5\pi/6$. So, the corresponding velocity will be interpreted to $-10\,\text{mm}\,\text{s}^{-1}$ instead of $14\,\text{mm}\,\text{s}^{-1}$. For a bipolar gradient with toggling technique, V_{enc} can be calculated by assigning phase equal to π and replacing m_1 by Δm_1 in Equation 2.23.

$$V_{\text{enc}} = \frac{\pi}{\gamma |\Delta m_1|}. \tag{2.26}$$

So, to avoid aliasing, V_{enc} has been chosen such that there is no velocity greater than that in the flow system. However, it has to be mentioned that choosing a V_{enc} much greater than needed results in low phase-SNR and decreases the phase-velocity resolution.

Based on Equation 2.26, Equation 2.24 can be represented in the following form,

$$\phi = \frac{v}{V_{\text{enc}}}\pi. \tag{2.27}$$

In order to have a better understanding, a numerical example is presented in the following. In this example, lobes of the bipolar gradient are applied consecutively, meaning that $\Delta t = T$. In the case of using the same bipolar gradient in both toggles, $\Delta m_1 = 2m_1$.

A bipolar gradient with the power of $G = 2.3487 \times 10^{-5}\,\mathrm{T\,mm^{-1}}$ and duration of 5 ms results in,

$$m_1 = GT^2 = 2.3487 \times 10^{-5} \times 0.005^2 = 5.8717 \times 10^{-10}\,\mathrm{T\,s^2\,mm^{-1}}. \tag{2.28}$$

Since $\Delta m_1 = 2m_1$, then,

$$\Delta m_1 = 1.1743 \times 10^{-9}\,\mathrm{T\,s^2\,mm^{-1}}. \tag{2.29}$$

Corresponding V_{enc} for the aforementioned bipolar gradient can be calculated from Equation 2.26.

$$\begin{aligned} V_{enc} &= \frac{\pi}{\gamma|\Delta m_1|} = \frac{\pi\,\mathrm{rad}}{267.522 \times 10^6\,\mathrm{rad\,T^{-1}\,s^{-1}} \times 1.1743 \times 10^{-9}\,\mathrm{T\,s^2\,mm^{-1}}} \Rightarrow \\ V_{enc} &= 10\,\mathrm{mm\,s^{-1}} \end{aligned} \tag{2.30}$$

The flow encoding bipolar gradient can be used with any imaging pulse sequence. In the following, a graphical presentation of using this technique in a FLASH pulse sequence is presented.

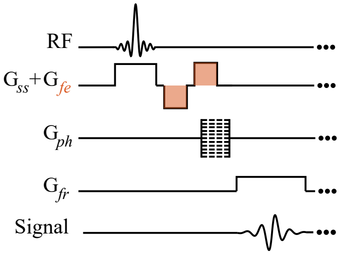

Figure 2.26: Graphical illustration of using a flow encoding bipolar gradient (shown by G_{fe}) in a FLASH pulse sequence. Here, flow encoding is performed in the direction of slice selection.

In Figure 2.26, the bipolar gradient is applied in the slice selection gradient. Therefore, it encodes only the corresponding component of the velocity. In general, the gradient can be applied in any direction.

3 MRV for compact flowmeters

This chapter is based on a collaboration with Dr. Pedro Silva [29]. Dr. Silva did the design of the hardware and flow channel and made the flowmeter [30]. The pulse sequence preparation, parameter optimization, and flow measurements were carried out in this research. The flow simulation is done by M.Sc. Andrea Cristina Hurtado Rivera; see Figure 3.5.

Nuclear magnetic resonance (NMR) has a variety of applications in both clinical [31, 32] and industrial fields [7, 33, 34] ranging from flow MRI evaluation [4] to nuclear magnetic resonance (NMR) in tissue metabolite detection and quantification [35]. The first imprints of motion on NMR signals were detected before the invention of MRI. In 1970, Morse, O.C., Singer, J.R. Morse showed that one can non-invasively measure blood velocity in a vein by using MR. This feature gives this technique more credit compared to invasive methods such as hot-film anemometry. In addition to being non-invasive, the MR technique has two more important characteristics. First, unlike particle imaging velocimetry, it doesn't need any tracer material. Second, there is no necessity to have optical access to the sample, which is an advantage for this method in comparison with other experimental techniques, i.e., laser Doppler anemometry (LDA). In addition to the three main benefits, this method has the following advantages compared to the conventional techniques in flow sensor technology. In Coriolis flowmeters, flow passage has to have a particular design to follow the principles of motion mechanics, which is not the case in the present method. Compared to electromagnetic flowmeters, there is no need to use conductive fluids. Furthermore, the ability to perform spectroscopy experiments is the most unique property of this technique. NMR spectrometers are able to perform very accurate flow measurements. Nevertheless, the sophisticated components required to perform magnetic resonance measurements put this technique in the category of high-cost methods and voluminous devices. Producing small and particularly inexpensive devices is an area of interest in the NMR industry [36]. However, such devices don't have the robustness of the standard spectrometers. The main target of the current chapter is to design a pulse sequence and optimize the parameters to perform robust flow measurement experiments with a low-cost and portable NMR-based flowmeter designed and manufactured by Dr. Silva. The device is made out of mass-produced, inexpensive, tiny parts.

3.1 Theoretical setup

Currently, MR is capable of performing even three-dimensional, three-component (3D-3C) velocimetry measurements. In such experiments, the sample is divided into several volumetric elements (voxels) in three-dimensional space. First, the targeted slice of the sample is selected, and then it goes through phase and frequency encoding to distinguish the signal coming from each voxel. As a consequence, the SNR of the signal has to be high enough such that it lasts until all the mentioned steps are taken. This means high values of SNR are required. It results in sophisticated, expensive, and voluminous hardware, which are the major limitations to doing onsite and reasonable experiments. In this study, instead of obtaining a velocity map, we focus on the mean flow measurement. In such a case, the spatial encodings are not needed, so we deal with the signal received from the whole sample. This reduces the needed SNR. In addition, removing the encodings enhances the time efficiency of the measurement, and it would be accomplished much faster than the 3D-3C experiment, which further decreases the required SNR. In such conditions, having a superconducting and highly homogeneous magnet or voluminous high-performance instrumentation is not necessary. Instead, a permanent magnet and portable electronics can do the job. To further facilitate the feasibility of the measurement, the signal comes from a well-engineered flow channel, which is designed to produce a laminar 2D-flow regime that provides higher SNR compared to cylindrical flow channels or turbulent cases. In many studies, the velocity is encoded into the magnitude of the signal [37, 38]. These techniques are mainly divided into two main categories, called *black blood angiography* and *time of flight* [39]. *Black blood angiography* is based on the saturation of signal coming from the moving sample while enhancing the one from the stationary part, and *time of flight* is the other way around. As a drawback, the magnitude of the signal is correlated either with lower or higher velocities, which results in the loss of SNR for a certain range of velocities. In this study, the velocity is linked with the phase of the NMR signal, resulting in high SNR for a much wider range of velocities.

3.2 Pulse sequence

To counteract the instability of a portable NMR-based flowmeter, the sequence shown in Figure 3.1 is employed. Using two acquisitions in a single measurement, to some extent, compensates for the adverse effect of the drift [30].

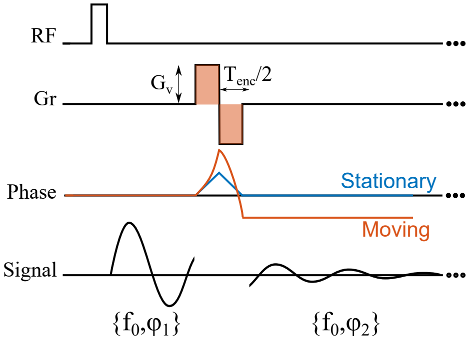

Figure 3.1: Schematic representation of a flow encoding bipolar gradient.

In Figure 3.1, G_v is the magnitude of the bipolar gradient, T_{enc} is bipolar gradient time, f_0 is the working frequency, and ϕ_1 and ϕ_2 are the phase of the signal in the first and second acquisitions respectively.

The pulse sequence consists of four parts. It starts with the excitation, which precedes the first acquisition. After that, a flow encoding bipolar gradient would be applied, which consists of two gradients with the same magnitude but the opposite directions. Such a gradient injects phase into the MR signal proportional to the velocity. The sequence ends with the second acquisition, which is supposed to be longer than the first one, in order to alleviate the loss of signal due to flow encoding, diffusion, and eddy currents. Having two acquisitions in the same measurement makes this method more robust against the instability of the static magnetic field. The injected phase $(\phi = \phi_2 - \phi_1)$ can be calculated from the following equation,

$$\begin{aligned} \phi &= \int_0^{T_\text{enc}} \gamma G(t) \cdot r(t)\, dt \approx \frac{-\gamma G_v T_\text{enc}^2}{4} \left(v_0 + \frac{1}{2} a_0 T_\text{enc} \right) = k_\text{enc} \overline{v}, \\ &\text{where, } k_\text{enc} = \frac{-\gamma G_v T_\text{enc}^2}{4}, \qquad \overline{v} = v_0 + \frac{1}{2} a_0 T_\text{enc}, \end{aligned} \tag{3.1}$$

in which γ is gyromagnetic ratio, v_0 is the velocity, and a_0 is the acceleration. Equation 3.1 shows the phase of each spin ensemble moving with the average velocity equal to $\overline{v}$. But, the spectrometer sees the vector summation of the signal emitted from all spin ensembles (called net signal). So, the phase response of the net signal (which is called net phase) is also a function of the flow profile, which shows the importance of the flow channel. As a result, in the next step, the goal is to evaluate the phase response of the available flow profile in the current flowmeter. Since the target is to have a portable one, the channel shape has to be a trade-off between a small flow channel and an ideal flow profile.

3.3 NMR response of the flow channel

In Equation 3.1, $\bar{v}$ is the average velocity. The equation stands in its ideal situation for a plug flow, which provides us with a uniform flow profile since, in this case, the signal coming from all the spins has the same phase and hence results in the highest possible SNR. But, in experimental conditions, such a case is not feasible. In this section, the flow channel designed by Pedro Silva [30], which has a rectangular cross-section, is presented and the corresponding NMR signal response is evaluated. It provides the flowmeter with a 2D flow so as to enhance the SNR, particularly for fast velocities. In order to show the superiority of this flow channel compared to the typical ones, which have mostly a cylindrical channel, a comparison is made in this research. A cylindrical flow channel provides us with a parabolic flow profile following the equation below,

$$v = 2\overline{v}\left(1-\left(\frac{r}{r_0}\right)^2\right), \tag{3.2}$$

where r is the distance from the center of the cylinder, and r_0 is the radius.
If the width-to-height ratio of a rectangular flow channel is big enough, the change in the flow profile close to the lateral sides would be negligible, and there would be a change just in one direction. So, the sample comes up with a near 2D-flow profile, which can be calculated by the following equation,

$$v = 1.5\overline{v}\left(1-\left(\frac{z}{z_0}\right)^2\right), \tag{3.3}$$

where z is the distance from the center of the channel, and z_0 is half of the height of the channel.
In Figure 3.2, the magnitude and phase response of the NMR signal emitted from three different flow profiles, including plug, 2D flow, and cylindrical, are shown. The average velocity in all cases is the same and equal to $\overline{v}$. Based on the simulations, the amplitude of the signal coming from a cylindrical flow channel has a significant drop-out (close to zero) for certain flow rates, but that of a rectangular one (2D flow) remains high for a wide range of flow rates. Also, regarding the phase response, it has a much better phase injection, which leads to greater phase-SNR and, hence, phase resolution versus velocity. Furthermore, since it is possible to adjust k_{enc}, a rectangular flow channel shifts the limit of

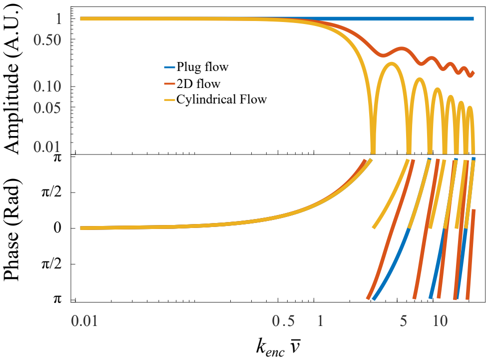

Figure 3.2: Magnitude and phase of the net MR signal after applying a flow encoding bipolar gradient. $\overline{v}$ is the mean velocity (Adapted from [29]).

the present method from the flow rate to first hardware limitations specifically regarding the gradient and then diffusion of the sample.

In order to evaluate the precision of the experiment, the signal-to-noise ratio of the flow measurement is defined as the following [30],

$$\mathrm{SNR}_Q = \frac{Q}{\sigma_Q}, \tag{3.4}$$

in which, Q is the flow rate, and σ_Q is uncertainty at Q. If the cross-section area of the flow channel is equal to A, SNR_Q holds [30],

$$\begin{aligned} \mathrm{SNR}_Q = \frac{Q}{\sigma_Q} = \frac{\cancel{A}\overline{v}}{\cancel{A}\sigma_{\overline{v}}} &= \frac{k_{enc}\overline{v}}{k_{enc}\frac{d\overline{v}}{d\phi_{2-1}}\sigma_{\phi_{2-1}}} \\ &= k_{enc}\overline{v}\ \mathrm{SNR}_0\sqrt{\frac{M^2}{M^2+1}\frac{d\phi_{2-1}}{d(k_{enc}\overline{v})}}, \end{aligned} \tag{3.5}$$

where SNR_0 is the SNR of the stationary measurement at $V = 0$, M is the ratio of the values of SNR in the first and second acquisitions, and $d\phi_{2-1}$ is the phase offset between the acquisitions. If the first and second acquisitions are performed with the same SNR, then $M = 1$. Considering $\phi = k_{\text{enc}}v$ and $\overline{v} = v$, one can rewrite the equation as 3.5 [30],

$$\text{SNR}_Q = \frac{\overline{v}}{\sigma_{\overline{v}}} = \frac{k_{enc}\overline{v}}{\sigma_{\phi_{2-1}}} = k_{enc}\overline{v}\frac{\text{SNR}_0}{\sqrt{2}}. \tag{3.6}$$

In Figure 3.3, the variation of $\text{SNR}_Q/\text{SNR}_0$ is plotted versus $k_{\text{enc}}\overline{v}$.

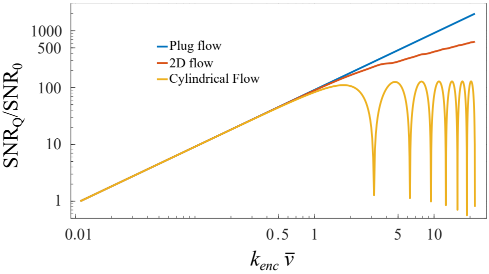

Figure 3.3: SNR of flow measurement versus $k_{\text{enc}}\overline{v}$ (Adapted from [29]).

In order to manufacture a compact NMR flowmeter, the volume of interest (VOI) is limited to $10 \times 10 \times 3\ \text{mm}^3$. A certain distance between the inlet/outlet of the chamber and VOI is necessary to let the flow develop to have a laminar uniform flow in the VOI. As a result, the chamber size of $27 \times 19 \times 4.2\ \text{mm}^3$ is considered for the flowmeter. The final design of the flow channel is shown in Figure 3.4.

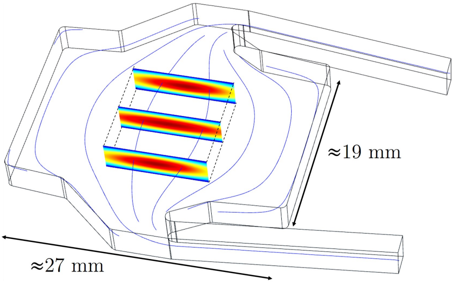

Figure 3.4: Expected flow profile within the volume of interest (VOI) (Reproduced from [29]).

As shown in Figure 3.4, the flow chamber is designed such that the VOI is provided by a laminar uniform flow field, resulting in a 2D flow used in Figures 3.2 and 3.3. Also, the flow channel is made out of PMMA to minimize the susceptibility mismatch issue [40]. The main frame of the flow channel is made out of a 3 mm PMMA sheet, and the upper and lower plates are made out of three laser-cut PMMA pieces (each one with 200 µm), glued together with UV-curable adhesive (Dymax 1187-M, Dymax Europe GmbH) to increase the rigidity of the upper and lower sides and avoid expansion under high pressure. The expected flow profile is shown in Figure 3.4. In order to evaluate the performance of the designed channel in reaching the desired flow profile, computational fluid dynamics (CFD) is used. Navier-Stokes equations are solved by the finite element method and using COMSOL Multiphysics to simulate the flow behavior. In these simulations, flow is considered laminar, incompressible, and no-slip condition at the walls.

The flow behavior is assessed for six different flow rates ranging from 0.1 to $2.0\,\mathrm{kg\,h^{-1}}$. The simulation shows good agreement between numerical results and the expected flow profile shown in Figure 3.4 up to a specific mass flow rate ($0.25\,\mathrm{kg\,h^{-1}}$). The result is shown in Figure 3.5 for six different flow rates.

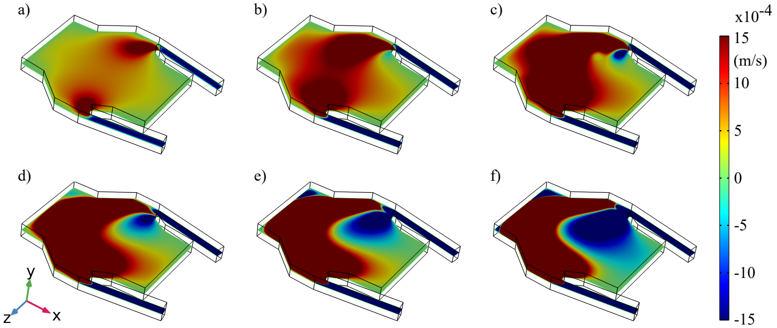

Figure 3.5: Simulation of the z-component of velocity in the central plane of the sample holder for six different flow rates, a) 0.1, b) 0.2, c) 0.3, d) 0.6, e) 1.2, and f) $2.0\,\mathrm{kg\,h^{-1}}$ (Adapted from [29]).

For flow rates higher than $0.25\,\mathrm{kg\,h^{-1}}$, there will be deviation due to the effect of recirculation which takes place below the inlet. By increasing the flow rate, the recirculation region expands and comes into the VOI. So, after this rate, deviation in phase response is expected, but it can still be useful to measure the flow rate even for higher flow rates.

3.4 NMR-based flowmeter

As mentioned at the beginning of this chapter, the hardware design and manufacturing of the flowmeter is done by Dr. Silva in the framework of his Ph.D. thesis [30]. However, the device is shown in Figure 3.6 and briefly introduced in this section.

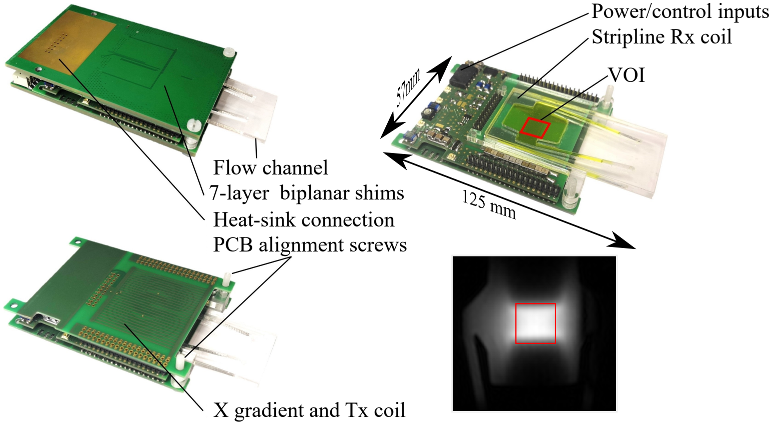

Figure 3.6: Demonstration of different parts of the setup. The PCBs, stripline and planar coils, flow channel, power/control inputs, and heat sink are shown in the figure. The VOI is displayed by a red rectangle. The prominence of the VOI in the MR signal is demonstrated by a stationary MR image (Adapted from [29]).

The device consists of three main parts. The first part is the coils. In order to achieve the best excitation-acquisition performance, two different coils are used for each purpose. For excitation, a solenoid coil is used to have a uniform excitation through the whole sample, and for acquisition, a stripline is employed. The use of a stripline enhances the signal acquisition from the VOI (in which the flow has the most uniform regime) and suppresses the signal of the volume out of the VOI (which is closer to the walls, inlet, and outlet and hence is not uniform). The enhancement of the signal from the VOI is demonstrated in the MR image in Figure 3.6. The second part is the shimming coils, which are used to improve the homogeneity within the VOI. Due to the fact that a permanent magnet is used to perform the measurements, having shimming coils is highly necessary. The performance of the shimming coils is demonstrated in Figure 3.7, and it is shown that these coils can significantly enhance the shimming. Based on the results, the FWHM decreases from 990 to 28 Hz, which approximately results in an increase in the length of T_2^* from 0.32 to 11.37 ms $\left(\mathrm{FWHM} \approx 1/\left(\pi T_2^*\right)\right)$.

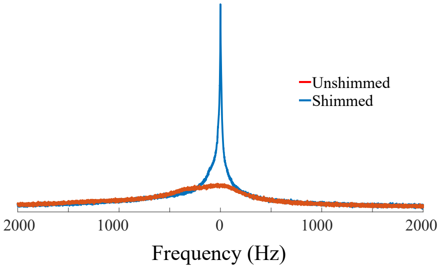

Figure 3.7: Comparison between the spectra before and after the shimming (Adapted from [29]).

The last part is the flow sample, which was already explained. The volume of the entire flowmeter, including all coils, flow channel, and all other components, is $125 \times 57 \times 15\,\mathrm{mm}^3$, such that it can be used in a 15 mm gap permanent magnet. Components of the device and corresponding dimensions, as well as parameters of the pulse sequence, are presented in Table 3.1.

Table 3.1: Geometrical and physical properties of the setup, as well as key parameters of the MR experiments (Adapted from [29]).

Item	Description
Device Mass	0.205 kg
Device Size	$125\times57\times15$ mm^3
Flow Channel Size (VOI)	$27\times19\times3$ ($10\times10\times3$ mm^3)
Detection Coil (VOI)	Stripline ($10\times7\times3$ mm^3)
Shimming Coil (VOI)	Biplanar ($10\times7\times3$ mm^3)
Transmitter Coil (VOI)	Solenoid (entire sample)
Magnetic Field	44.7 MHz
Gradient Power	14 165.19 Hz mm^{-1}
Gradient Duration	6 ms
First Acquisition Duration	0.2 ms
Second Acquisition Duration	12 ms
RF Pulse Duration	0.0256 ms
RF Pulse Bandwidth	50 kHz
Sampling Frequency	50 kHz
RF Pulse Power	0.52 W
SNR	260

3.5 Experimental results

In this section, the performance of the NMR-based flowmeter (shown in Figure 3.6) in experimental conditions in an 1.05 T Bruker® permanent magnet is evaluated. In order to encode the flow into the net-phase of the NMR signal, a pulse sequence based on the flow encoding bipolar gradient is used (shown in Figure 3.1). The first part of the pulse sequence is the excitation pulse. The use of a permanent magnet necessitates a wideband RF pulse to alleviate the frequency drift in such a magnet. That is why an RF pulse with the bandwidth of 50 kHz is used to fulfill the requirement. A *Drift Adjustment* has already been used to mitigate the frequency drift. This adjustment uses z_0 shim to return the magnetic field to the last value. However, it can't completely compensate for the drift. It is noteworthy that *Frequency Adjustment* has to be avoided during a set of measurements since, instead of returning the frequency to the last value, it just changes the working frequency in the software, which changes the phase response of the hardware and makes the phase response of the experiments unrelated.

The second part is the first acquisition. This step has to be performed as fast as possible to keep enough SNR for the second acquisition. In addition to the first acquisition, the flow encoding gradient is applied before the second acquisition, which causes a loss of SNR. During the first acquisition, the initial or reference phase is recorded.

After the first acquisition, the bipolar flow encoding gradient is applied. To enhance the phase-SNR and phase-velocity resolution, it is better to apply a strong bipolar gradient as long as the signal in the second acquisition has enough SNR. The strength of bipolar gradient depends on the magnitude and gradient oscillation time. To reduce the unfavorable effect of displacement during measurement performance, it is recommended to deliver the targeted k_{enc} by a strong magnitude (G_v) and a short time (T_{enc}), see Equation 3.1. That is why 90% of the available gradient is used ($14\,165.19\,\text{Hz}\,\text{mm}^{-1}$). So, the power of gradient is set to 90%, and then we try to use the longest possible time for bipolar gradient, by which SNR is still high enough to perform a reliable and robust measurement. Based on the evaluations, by applying 90% of the gradient for 6 ms, the SNR is still high enough.

The next step is the second acquisition. The second acquisition should be much longer than the first one. The MR signal loses its power due to flow encoding as well as diffusion and relaxation. So, the length of the second acquisition is 12 ms.

In the end, we expect the phase difference between the two acquisitions to be in a relationship with the flow rate. To have a reference, first, the experiment is run for a stationary sample. The resultant phase difference is deducted from the injected phases of the experiments with a non-zero flow rate. To perform a reliable measurement, the flow is provided by an Elveflow® OB1 Mk3+ pressure controller with the pressure stability of 0.006% FS[1] (500 µbar) for the pressure range of 0 to 8000 mbar to have a very stable flow rate. The mass flow rate is tracked by a (mini) Cori-Flow, Bronkhorst® flowmeter with the accuracy of 0.2%. The experiments are performed starting from a stationary measurement to the flow rate of $2\,\mathrm{kg\,h^{-1}}$ for 26 data points. For each flow rate, the measurement is repeated 10 times to evaluate the robustness of the setup. The results are presented in Figure 3.8.

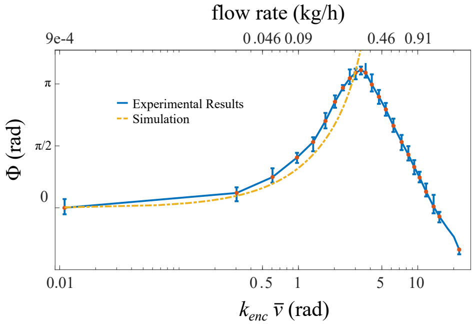

Figure 3.8: Phase response of the net MR signal versus $k_{\mathrm{enc}}\overline{v}$ and mass flow rate. The error bar shows the deviation for decuplicate measurements (Adapted from [29]).

The result presented in Figure 3.8 is in a meaningful relation with the result presented in Figure 3.5. Evaluating Figure 3.5 reveals three facts about the flow behavior. First, up to $0.2\,\mathrm{kg\,h^{-1}}$, the flow profile follows the ideal flow behavior shown in Figure 3.4. Second, starting from $0.3\,\mathrm{kg\,h^{-1}}$, a secondary flow region appears in the flow channel and grows as the flow rate increases. Third, at 1.2, the regions with negative and positive flow components are comparable. The consequence of these three facts is evident in Figure 3.8.

---

[1] FS stands for full scale.

It demonstrates good agreement between experimental results and simulation (see Figure 3.2) up to $k_{\mathrm{enc}}\overline{v} \approx 2.7$, which corresponds to the flow rate of $0.25\,\mathrm{kg\,h^{-1}}$ (or $69.444\,\mathrm{mm^3\,s^{-1}}$). It results in an average velocity of $0.857\,\mathrm{mm\,s^{-1}}$ in the sample. Starting from $0.3\,\mathrm{kg\,h^{-1}}$, and by appearing the secondary flow region, the phase injection reverses the trend. And finally, around $1.2\,\mathrm{kg\,h^{-1}}$, the injected phase reaches zero and continues the downward trend afterward. Despite the fact that the phase response deviates from the ideal streamlines after a certain flow rate, it can still be useful as long as it is locally bijective.

Also, based on Equation 3.5, the SNR of the measurement $\left(\mathrm{SNR}_Q\right)$ is calculated and presented in Figure 3.9.

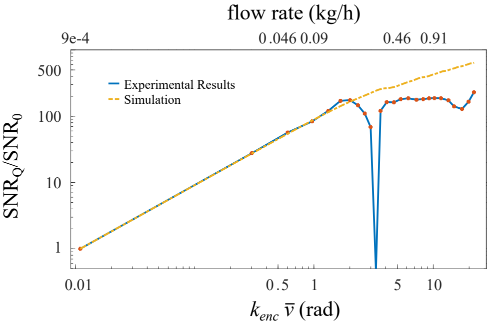

Figure 3.9: SNR of the flow measurement versus $k_{\mathrm{enc}}\overline{v}$ and mass flow rate. The SNR is calculated by Equation 3.5 (Adapted from [29]).

In addition to the phase response, the amplitude of the MR signal was also presented in Figure 3.2. In Figure 3.10, it is compared with the experimental results. It shows a slight discrepancy between the simulation and experimental results. By increasing the flow rate, the amplitude of the MR signal increases, and after a certain flow, it starts the sinusoidal trend. This disagreement can be due to field inhomogeneity or asymmetry of the lobes in the bipolar gradient.

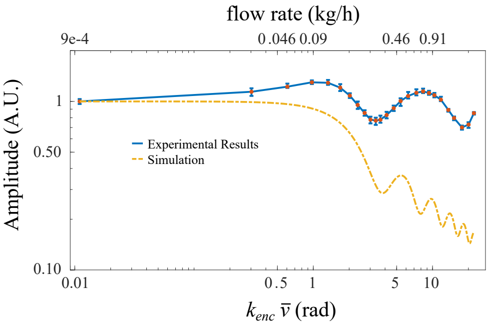

Figure 3.10: Magnitude of the net MR signal in the second acquisition versus $k_{\mathrm{enc}}\bar{v}$ and mass flow rate. The error bar shows the deviation for decuplicate measurements (Adapted from [29]).

3.6 Conclusion

NMR techniques are able to measure the flow rate in a non-invasive manner. Since this technique works based on the MR signal emitted directly from the nuclei, it is able to perform very reliable measurements. Standard NMR spectrometers are highly precise and reliable yet costly and bulky. That is why they are not widely used in the flowmeter industry. In this study, a compact device, which was made by Dr. Pedro Silva during his PhD [30], was used. The device is shown in Figure 3.6. In the design and development of the device, it is tried to minimize the costs and volume such that the total price stays below 1000 € and the device volume is $125 \times 57 \times 15\ \mathrm{mm}^3$. Using a permanent magnet makes this device portable but also less stable compared to the superconducting magnets. The main concept of this chapter was to compose a pulse sequence and optimize the parameters and adjustments to compensate for the instability in the compact portable NMR flow sensors.

The pulse sequence preparation (in ParaVision), choosing key parameters, and evaluating flow behavior were carried out in this study. First, the flow behavior was evaluated to check the uniformity of the flow profile in the VOI. Based on the results shown in Figure 3.5, the flow profile is in good agreement with the ideal case presented in Figure 3.4 up to around $0.25\,\mathrm{kg\,h^{-1}}$.

Then, a pulse sequence based on the flow encoding bipolar gradient technique was written in ParaVision imaging software. As shown in Figure 3.1, this pulse has two acquisitions. So, it is designed based on *Job Acquisition* technique, available by ParaVision software provided by Bruker®. The flow encoding gradient is situated between two acquisitions. As a result, the phase offset between the acquisitions should be a function of the flow rate. In many studies, the flow is encoded into the amplitude of the MR signal [41]. This technique leads to a considerable loss of SNR for a certain flow range, either for fast or slow flow rates. Encoding the flow rate in the phase of the MR signal keeps the SNR high for a very wide range of velocities.

In Figure 3.2, a comparison is made between the magnitude and phase of the MR response of the flow channel with three different cross-sections. Plug flow provides the best signal amplitude; however, it is not feasible in experimental conditions. It also shows that using a rectangular channel can keep the signal high for a much wider range of flow compared to a conventional cylindrical channel. It delivers a 2D flow profile, which provides us with a high signal and phase-SNR. Nevertheless, it can still be a useful study to optimize the cross-section of the flow channel even further. The best cross-section might be elliptic or even an irregular shape.

Another parameter to be further optimized is the change in the cross-section across the flow direction (z-axis in Figure 3.5). By increasing the flow rate, flow reversal disturbs the uniformity of the flow profile. Despite the fact that the result is still useful even after losing the uniformity, topology optimization of the flow channel can be very helpful in shifting the appearance of the recirculation and keeping the uniformity for a wider range of flow rates.

Here, we briefly mention some limitations of the present method. MR velocimetry mainly works based on flow encoding gradients. This can reduce the MR signal due to diffusion. So, when displacement is comparable with diffusion, the current method suffers from low SNR. On the other hand, based on Equation 3.1, the injected phase is directly related to γ. For liquids with low γ, strong gradients (G_r) are required. This can increase the adverse effect of diffusion and eddy current and even reach the upper limit of the gradient system.

The most unique potential advantage of the present method is the main application of NMR, namely spectroscopy. This can be very helpful in keeping track of the flow rate as well as the chemical reactions of the sample in the same measurement. It can even be used to measure the flow rate of two different chemicals within the same measurement in multiphase flow regimes.

4 Optimal control theory for time-efficient MRV

Optimal control theory (OCT) can be defined as a framework to obtain the required control variables for a dynamic system to reach a specific target state, starting from an initial condition, satisfying governing equations, and optimizing a defined cost function under specific optimality criteria. Any dynamic system can be controlled by a number of variables, and it will be extremely beneficial to find the required input parameters to optimize the performance of the system in reaching a certain target. OCT has been used in many scientific studies ranging from aerospace [42] and economics [43] to magnetic resonance [44].

To clarify the idea of OCT in a general way and define some terms and definitions, we can consider minimizing fuel consumption in a car journey. Let us assume that we want to find the optimized sequence of changing gears. There are some assumptions for this dynamic system. The car starts from a certain point and is supposed to go to a specific location. In such a case, the start point of the car is called *initial state* or *initial condition*, the endpoint is called *target state (TS)*, and the equations of motion would be the governing equations. Also, the sequence of changing gears would be the *control variables* or *control field*. It can also be called *controls*. The fuel consumption plus any deviation from the TS would be the *cost function*, which must be minimized. In such cases, OCT can help us to find the required sequence.

OCT has been widely used in magnetic resonance applications. It can be used to generate an RF pulse to manage the phase pattern of an MR image or even to perform elasticity measurement [44], or it can be employed to design a pulse to enhance the contrast in an MR image [45]. In such a case, the goal is to maximize the payoff function, which represents the contrast. In the current chapter, OCT is utilized to design an RF pulse able to perform two jobs at the same time. The first job is to excite a specific thickness of the sample (similar to any slice selective RF pulse. i.e., sinc pulses). The second job is to establish a bijective relationship between phase and velocity (comparable with the bipolar gradient technique). The goal is to replace the RF pulse and bipolar gradient with an OC RF pulse in a flow imaging pulse sequence. It can make the TE shorter, which enhances the SNR. In addition, a shorter TE makes the pulse sequence more appropriate for fast flow measurement [9].

4.1 Optimal control theory (OCT)

In MR, OC can be defined as a recipe to design the required shaped RF pulses to navigate the magnetization from an initial state (mostly equilibrium) to a desired TS while a user-defined cost function is optimized. The cost function can be defined based on the desired application. It can be designing an inversion pulse to have a uniform inversion in a certain bandwidth [46] or to generate a preparation pulse for a certain purpose [47]. OCT takes the chosen TS into account and finds the needed RF pulse. In fact, the components of the RF pulse are the control variables. TS plays a role in designing the cost function. The function is designed such that when it reaches the extremum, the TS is reached. OCT starts with the definition of the control variables. In the current study, they are the components of the excitation pulse and are represented in a vector form and denoted by B, which is a function of time.

$$\vec{B}(t) = \begin{pmatrix} B(t_1) \\ \vdots \\ B(t_n) \end{pmatrix}, \tag{4.1}$$

where n is the number of control variables; here, it is the number of time elements. For an excitation pulse, $B(t_i)$ is a complex number. Following the governing equations and satisfying the boundary conditions, the corresponding state of the system, $M(t)$, can be expressed as follows,

$$\vec{M}(t) = \begin{pmatrix} \vec{M}(t_1) \\ \vdots \\ \vec{M}(t_n) \end{pmatrix}. \tag{4.2}$$

In Equation 4.2, $\vec{M}(t)$ is the magnetization evolution, and $\vec{M}(t_i)$ is the magnetization state at i*th* time element, $\vec{M}(t_i) = \left(M_x(t_i), M_y(t_i), M_z(t_i)\right)$. In OC, commonly, a cost function is defined such that when the cost is zero, the final state and target state are the same[1]. If there is a control variable that guides the magnetization such that the cost is zero, it is called the optimal control field and is denoted by $\vec{B}^*$.

$$\text{If } \vec{B} = \vec{B}^* \;\Rightarrow\; C = 0 \;\Rightarrow\; \vec{M}\left(t_f\right) = \vec{M}_{\text{TS}}. \tag{4.3}$$

The goal of the OCT is to find the $\vec{B}^*$. To solve such a problem, the Pontryagin Maximum Principle (PMP) can be used.

4.1.1 Pontryagin Maximum Principle (PMP)

PMP is a remarkably powerful means to solve OC problems [48]. Initially, it was presented in mathematics [49] and space mechanics [45]. Recently, it has been broadly used in MR applications [46, 47]. In the following, it will be explained how PMP can help us to solve the problem. The dynamic system of a spin ensemble can be explained by the subsequent equations,

$$\begin{cases} \dot{\vec{M}} = f\left(\vec{M}, \vec{B}, t\right) \\ \vec{M}(t_0) = \vec{M}_0 \end{cases}, \tag{4.4}$$

---

[1] It is not always the case. For example, in some cases, a payoff function is defined, and the goal is to maximize it. For instance, if enhancing the contrast is favorable, such a function can be useful.

in which the first line represents the Bloch equations, and the second line indicates the initial condition at equilibrium. Correspondingly, $\vec{M}$ is the magnetization, $\vec{B}$ is the excitation pulse, and t is the time. The cost function of the optimal control problem (OCP) can be defined as follows,

$$J\left(\vec{B}\right)=\cancelto{0}{\int_0^{t_f} L\left(\vec{M},\vec{B}\right)dt}+C\left(\vec{M}\left(t_f\right)\right)=C\left(\vec{M}\left(t_f\right)\right), \tag{4.5}$$

where the first term, $\int_0^{t_f} L(\vec{M},\vec{B})dt$, is the integrated or running cost and represents the deviation between the desired evolution and the targeted one. As indicated in the equation, the integrated cost is zero since, in the current case, we just care about the final state of the magnetization. The second term, $C(\vec{M}(t_f))$, is called the final cost, which is defined based on the deviation between the magnetization at t_f and the TS, $\vec{M}_{\mathrm{TS}}$. The definition of PMP is formulated based on the definition of pseudo-Hamiltonian,

$$H=\vec{P}\cdot\dot{\vec{M}}, \tag{4.6}$$

where $\vec{P}$ is the adjoint state, and $\vec{M}$ is the state of the system. Based on PMP, optimal control field $\vec{B}^{*}$, and corresponding $\vec{M}^{*}$ and $\vec{P}^{*}$, which are optimal state and optimal adjoint state, must maximize the Hamiltonian at every time element between t_0 and t_f:

$$H\left(\vec{M}^{*},\vec{P}^{*},\vec{B}^{*}\right)=\max_{B\in B_{ad}} H\left(\vec{M},\vec{P},\vec{B}\right), \tag{4.7}$$

where, $B_{ad}\in\mathbb{R}$ is the admissible control field. Also, optimal state and adjoint state ($\vec{M}^{*}$ and $\vec{P}^{*}$) must fulfill the following equations,

$$\dot{\vec{M}}^{*}=\frac{\partial H}{\partial\vec{P}^{*}}, \tag{4.8}$$

$$\dot{\vec{P}}^{*}=-\frac{\partial H}{\partial\vec{M}^{*}}, \tag{4.9}$$

and satisfy the following boundary conditions,

$$\vec{M}^{*}\left(t_0\right) = \vec{M}_0, \tag{4.10}$$

$$\vec{P}^{*}\left(t_f\right) = -\frac{\partial C}{\partial \vec{M}^{*}\left(t_f\right)}. \tag{4.11}$$

Equation 4.8 gives us the trajectory of the state of the system, which is also called forward propagation, and Equation 4.10 defines its boundary condition. Equation 4.9 results in the trajectory of the adjoint state of the system, which is also called backward propagation, and Equation 4.11 defines its boundary condition. To maximize the Hamiltonian and satisfy Equation 4.7 GRadient Ascent Pulse Engineering (GRAPE) algorithm is employed, which will be explained in Subsection 4.3.3. Also, to solve the differential equations and calculate the forward and backward propagation, a numerical method called the differential quadrature method (DQM) is used.

4.2 Differential quadrature method (DQM)

Numerical solutions have many applications to solve differential equations in engineering problems. Classical methods, i.e., finite elements, are very well-known and developed. In these methods, using a large number of elements leads to accurate results, but it demands supercomputers with high computational performance. That is why it is always tried to find cheaper numerical methods. One of these methods is called the differential quadrature method (DQM). This method was first used by Bellman and Casti [50] in 1971 as a numerical method to solve partial differential equations. Since then, this method has been widely used in many different applications ranging from biosciences [51] and fluid dynamics [52] to chemical engineering [53]. In this study, this method has been used to solve Bloch equations.

4.2.1 DQM governing equations

The differential quadrature method is based upon the fact that the value of a function derivative with respect to a certain variable at a specific discrete point can be approximated by the weighted sum of values of the function at all discrete points in that direction,

$$\frac{\partial^m M(t)}{\partial t^m}|_{t_i} = \sum_{j=1}^{N} C_{\mathrm{ij}}^m M(t_j), \tag{4.12}$$

where m is the order of derivative, $M(t)$ is the function (magnetization in our case), t_i is the ith discrete point in the time domain, C_{ij}^m is the weighting coefficients, and N is the number of points (or elements) in the time domain. The main point in the DQM is that the value of weighting coefficients doesn't depend on the function but rather depends on the distribution of discrete points. Bellman introduced two methods to calculate weighting coefficients. The first one was based on a system of algebraic equations, which could lead to ill-conditioning. To avoid this problem, the second method was introduced, which was based on Lagrange interpolation functions [53],

$$M_k(t) = \prod_{i \neq k}^{N} \frac{t - t_i}{t_k - t_i}. \tag{4.13}$$

If we substitute Equation 4.13 into Equation 4.12, weighting coefficients corresponding to the first-order derivative can be calculated from the following equations,

$$C_{\mathrm{ij}} = \frac{\prod(t_i)}{(t_i - t_j)\prod(t_j)}, \qquad i, j = 1, 2, ..., N, \quad \text{and} \quad j \neq i,$$

$$\tag{4.14}$$

$$\text{where,} \quad \prod(t_i) = \prod_{k=1,\ k\neq i}^{N} (t_i - t_k),$$

$$C_{\mathrm{ii}} = -\sum_{k=1,\ k\neq i}^{N} \frac{1}{t_i - t_k}, \qquad i = 1, 2, ..., N. \tag{4.15}$$

4.2.2 Sampling points selection

The accuracy of DQM is highly dependent on the distribution of sampling points. Despite the fact that uniform distribution of grid points has been widely used by many researchers, it has turned out that a non-uniform distribution leads to more accurate results and enhances the consistency of the method [54].

Present studies show that Chebyshev-Gauss-Lobatto distribution Type II is effective in avoiding ill-conditioning [55]. In this method, the distribution of nodes is presented as the following,

$$t_i = \frac{1 - \cos\left[(i-1)\pi/(N-1)\right]}{2}, \qquad i = 1, 2, ..., N. \tag{4.16}$$

This method was used firstly by Shu and Richards [52]; and Bert and Malik found this method better than the alternative ones, i.e., the equally spaced, Legendre, and Chebyshev methods in many cases [54].

In Section 4.1, it was explained how OCT could help us design an RF pulse to reach a certain TS at the end of the excitation time (t_f). Then, in Section 4.2, the application of DQM was introduced as a numerical tool to solve the corresponding differential equations. In the next section, the application of OCT in the design of RF pulses in MRI will be explained.

4.3 Application of optimal control theory in MRI

OCT has many implementations in MRI applications ranging from contrast enhancement [47] to phase map control and MR Elastography [44]. The application of OCT consists of several steps. First, based on the objective of the OCP, a mathematical model has to be designed. Accordingly, the TS and cost function will be defined. Then, the GRAPE algorithm will be used to minimize the cost function and generate the RF pulse. In this section, OCT is employed to design an RF pulse to control the phase map and reach a certain phase pattern in the phase encoding direction of an MR image. Then, in Section 4.4, the theory is used to design a flow-encoding excitation pulse.

The objective of the OCP in this section is to inject the phase pattern shown in Figure 4.1 in the phase encoding direction of an MR image. A standard image, taken in ideal situations, has a constant phase value along this direction. But, using OCT, we would like to design an RF pulse that is able to inject the targeted phase pattern.

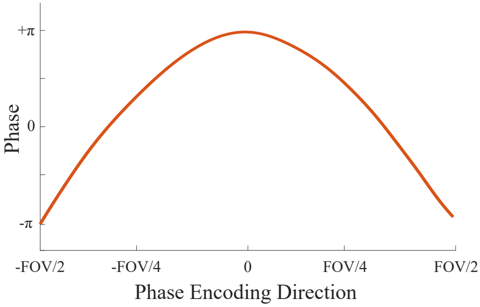

Figure 4.1: Illustration of the desired phase profile.

4.3.1 Mathematical model

First, we need to design a mathematical model. As implied by Figure 4.1, voxels in the phase encoding direction are wished to have different phases, meaning that the desired final state of each voxel is different. In order to reach a different final state for each voxel, the OC RF pulse needs a dissimilarity between the voxels to evolve their magnetizations differently. During the application of the RF pulse, a gradient is applied in the phase encoding direction to cause such a dissimilarity; as a result, voxels will experience different frequencies. So far, in the pulse sequence, the slice selection gradient and RF pulse are replaced by the OC gradient, which is applied in the phase encoding direction, and the

OC RF pulse. Now, the question is how we can perform the slice selection. In order to achieve the slice selectivity, one can use the saturation modules. In fact, the volume before and after the targeted slice would be saturated before the excitation. As a result, at the beginning of the OC RF pulse, only the targeted slice is polarized. The sequence shown in Figure 4.2 would be the complete form of the pulse sequence.

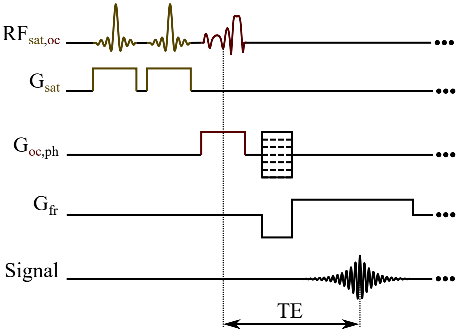

Figure 4.2: Schematic representation of the optimal control pulse sequence, including saturation pulses.

4.3.2 Target state and cost function definition

After designing the mathematical model, the TS and cost function must be defined. The objective is to reach the phase pattern shown in Figure 4.1. So, the phase of the TS will be defined as the following,

$$\phi_i = -2\pi \left(\frac{\delta_i}{G_{\mathrm{oc}} \times \frac{\mathrm{FOV}_{\mathrm{ph}}}{2}} \right)^2 + \pi, \quad \delta_i = G_{\mathrm{oc}} \times x_i \tag{4.17}$$

where ϕ_i is the phase of the voxel, δ_i is the frequency offset, G_{oc} is the OC gradient, $\mathrm{FOV}_{\mathrm{ph}}$ is the FOV in the phase encoding direction, and x_i is the distance between the center of the voxel and the isocenter of the gradient. Also, in the TS, the z-component of the magnetization is zero, meaning that the magnetization is desired to be at the XY-plane at t_f.

Accordingly, the cost function would be defined as the quadratic difference of any deviation from this relationship,

$$C\left(\vec{B}_x,\vec{B}_y\right)=\frac{1}{N}\sum_{i=1}^{N}\left\|\vec{M}_i\left(t_f\right)-\vec{M}_{\mathrm{TS}_i}\right\|^2, \tag{4.18}$$

in which C is the cost, B_x and B_y are the x and y components of the RF pulse, N is the number of voxels in the phase encoding direction, i is the voxel counter, $\vec{M}_i\left(t_f\right)$ is the magnetization of the ith voxel at the end of excitation time t_f, and $\vec{M}_{\mathrm{TS}_i}$ is the TS of the ith voxel. In the following, the GRAPE algorithm will be used to minimize the cost function.

4.3.3 GRAPE algorithm

In this study, in order to minimize the cost function (Equation 4.18), the GRadient Ascent Pulse Engineering (GRAPE) algorithm [56] is used. The steps of the algorithm are explained in Algorithm 1.

Algorithm 1: GRAPE (Adapted from [57]).

```
Result: The optimal control variables $\vec{B}^*$
1. Set the counter k equal to 1 and the control variables $\vec{B}^{(k)}$ equal to
   the initial guess;
while $C\left(\vec{B}^{(k)}\right) > \varepsilon$ do
    2. Calculate the forward propagation $\vec{M}^{(k)}$ by solving Equation 4.8
       and fulfilling the start condition 4.10 based on the control
       variables $\vec{B}^{(k)}$;
    3. Calculate the backward propagation $\vec{P}^{(k)}$ by solving Equation
       4.9 and fulfilling the end condition 4.11 based on the control
       variables $\vec{B}^{(k)}$;
    4. Calculate $\partial C/\partial\vec{B}^{(k)}$ based on the forward and backward
       propagation;
    5. Adjust the control variables based on the derivatives and the
       step size: $\vec{B}^{(k+1)}=\vec{B}^{(k)}-\eta\partial C/\partial\vec{B}^{(k)}$. Set the counter $k+=1$;
end
```

The idea of this algorithm is based on taking steps in the opposite direction of the gradient to find the local minimum of the function; see Figure 4.3.

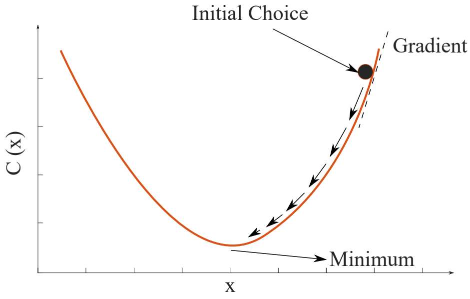

Figure 4.3: Gradient ascent algorithm.

Since the algorithm is based upon a gradient ascent algorithm, reaching the global minimum is not guaranteed. An inappropriate initial guess in the GRAPE algorithm can make the OC problem converge to a local minimum; see Figure 4.4.

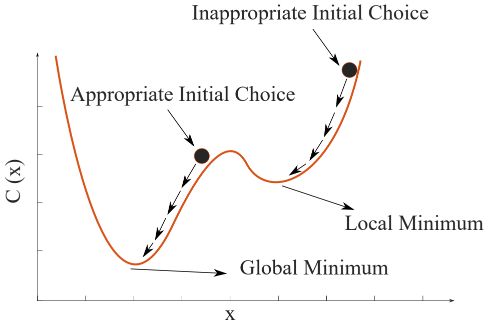

Figure 4.4: Local and global minimum in gradient ascent algorithm.

The cost function is defined based on the quadratic difference between the TS and the final state; consequently, it doesn't take negative values. So, when the cost function converges to zero, it ensures that it states at its global minimum. Nonetheless, it has to be mentioned that even with an appropriate initial guess,

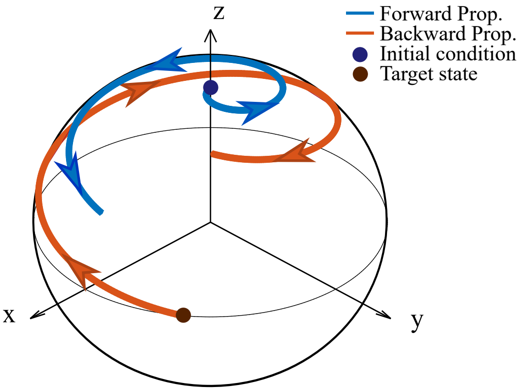

Figure 4.5: Schematic representation of forward and backward propagations used in the GRAPE algorithm.

the global minimum is not necessarily zero. Depending on different parameters, an OCP can become over-constrained. In such a case, the global minimum of the cost function would be a non-zero value. Very short or long excitation times and extremely weak or strong OC gradients are among the most influential reasons for an over-constrained OCP.

Algorithm 1 consists of five steps. The first step is to choose the initial guess, which was explained before. The second step is to calculate forward propagation, which can be achieved by solving the Bloch equation, fulfilling the initial boundary condition at equilibrium. The third step is to calculate the backward propagation, which can be obtained by solving the Bloch equation satisfying the TS as the end condition. A schematic representation of the forward and backward propagations is presented in Figure 4.5. It is shown in the figure that forward propagation satisfies the initial condition, and backward propagation fulfills the end condition (TS).

In the next step, based on the forward $\vec{M}^{(k)}$ and backward $\vec{P}^{(k)}$ propagation, the derivative of the cost function with respect to the components of the control field is computed by the following equation [58],

$$\frac{\partial C}{\partial \vec{B}^{(k)}} = \vec{P}^{(k)} \times \vec{M}^{(k)}, \tag{4.19}$$

and then the control variable will be updated for the next iteration.
Another term in the GRAPE algorithm is the step size η, mentioned in the $5th$ line. The value of η has to be optimized. On the one hand, small values result in a slow convergence and hence the need for many iterations. On the other hand, large values lead to overshooting and divergence of the algorithm. In the end, the algorithm will be repeated until the convergence criterion is reached.

4.3.4 OC gradient selection and RF pulse generation

The optimal control gradient (G_{oc}) shown in Figure 4.2 is chosen such that it applies a total range of 600 Hz of frequency offset over the FOV, which means that the voxels at the most right and left side of the FOV respectively experience 300 Hz and -300 Hz frequency offset during the excitation time. The excitation time is considered to be 10 ms and is discretized into 300 time elements. Based on these assumptions and by using the GRAPE algorithm, the RF pulse shown in Figure 4.6 is designed. In the next subsection, it will be employed in both simulation and experimental evaluations.

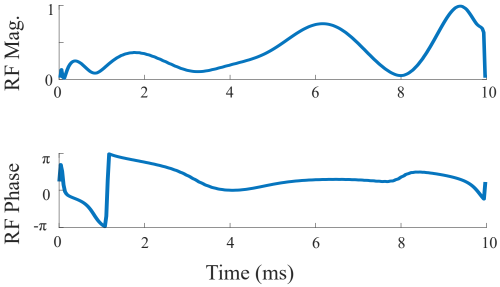

Figure 4.6: Magnitude and phase of the OC excitation pulse to reach the TS shown in Figure 4.1 (Adapted from [57]).

4.3.5 Results and discussion

In the first step, the Jülich Extensible MRI Simulator (JEMRIS), which is an open-source MRI simulator [59], is used to verify the functionality of the pulse. In this simulator, first, the pulse sequence should be implemented in the JEMRIS_seq framework (Figure 4.7).

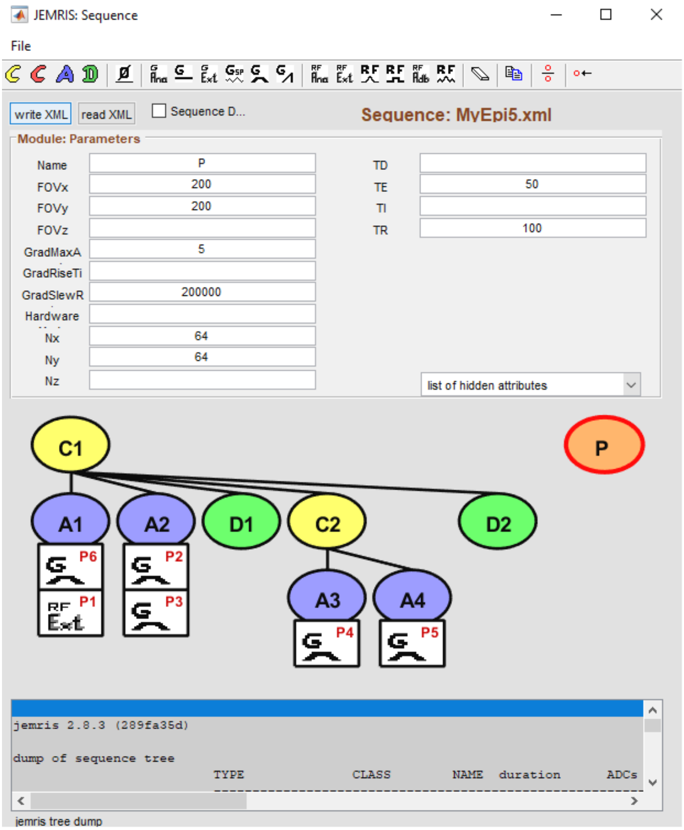

Sequence: MyEpi5.xml

Name: P
FOVx: 200
FOVy: 200
FOVz:
GradMaxA: 5
GradRiseTi:
GradSlewR: 200000
Hardware:
Nx: 64
Ny: 64
Nz:
TD:
TE: 50
TI:
TR: 100

```
jemris 2.8.3 (289fa35d)

dump of sequence tree
                          TYPE              CLASS        NAME  duration        ADCs
                          ----------------------------------------------------------
```

Figure 4.7: JEMRIS sequence framework.

All parts of the sequence, including the shape of the OC pulse, OC gradient, phase and frequency encoding gradients, and all other parameters regarding the pulse sequence, are supposed to be chosen in this graphical user interface (GUI). The sequence is designed based on an Echo planar imaging (EPI) pulse sequence, in which field of view (FOV) is equal to 200 mm, the number of voxels in each direction is 64, TE is 50 ms, and TR is 100 ms (Figure 4.8).

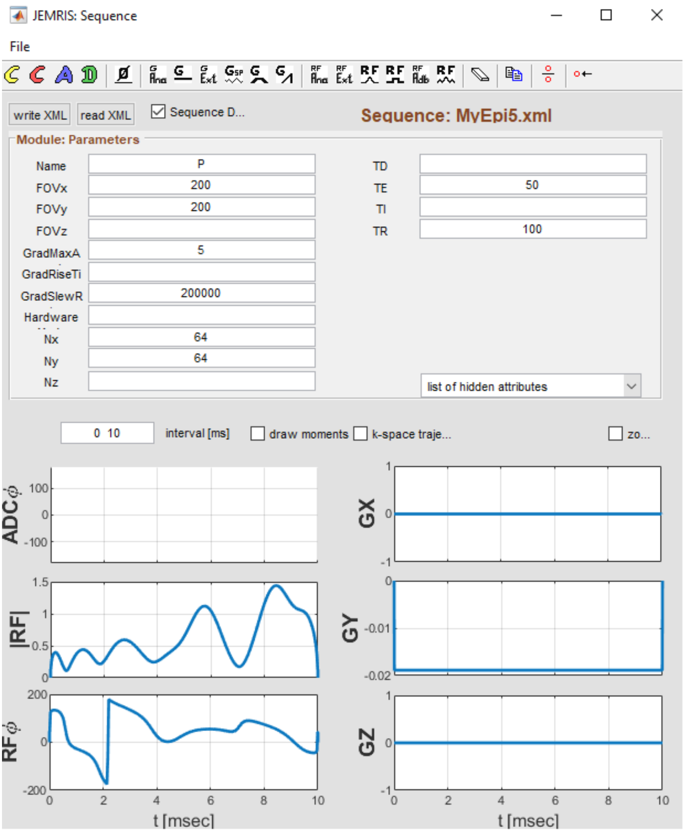

Sequence: MyEpi5.xml

Module: Parameters

Name	P	TD	
FOVx	200	TE	50
FOVy	200	TI	
FOVz		TR	100
GradMaxA	5		
GradRiseTi			
GradSlewR	200000		
Hardware			
Nx	64		
Ny	64		
Nz			

0 10 interval [ms]

Figure 4.8: JEMRIS sequence framework.

In the next step, the pulse sequence should be imported in another GUI called JEMRIS_sim (Figure 4.9).

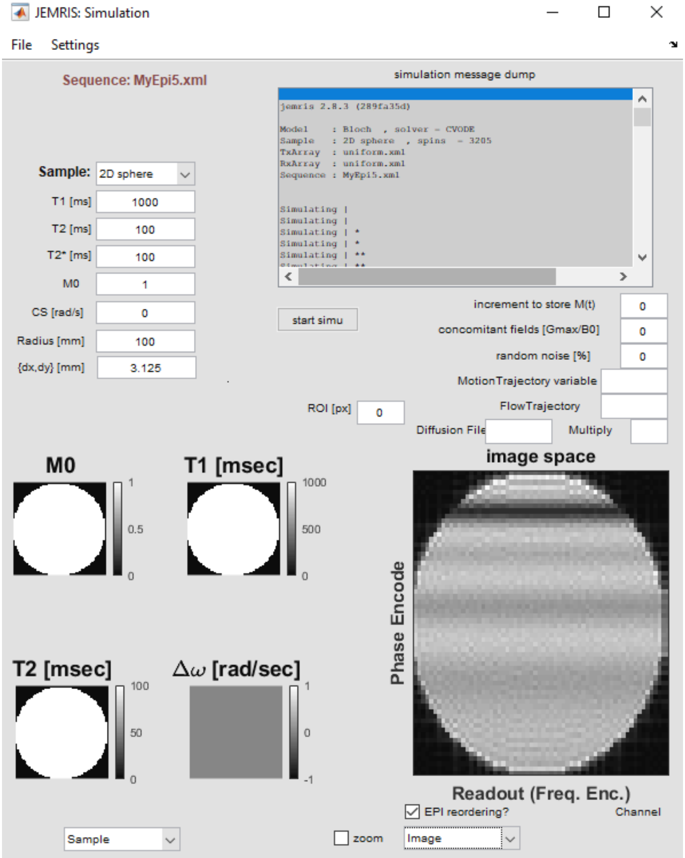

```
jemris 2.8.3 (289fa35d)

Model    : Bloch  , solver = CVODE
Sample   : 2D sphere  , spins  = 3205
TxArray  : uniform.xml
RxArray  : uniform.xml
Sequence : MyEpi5.xml


Simulating |
Simulating |
Simulating | *
Simulating | *
Simulating | **
```

Sample: 2D sphere
T1 [ms] 1000
T2 [ms] 100
T2* [ms] 100
M0 1
CS [rad/s] 0
Radius [mm] 100
{dx,dy} [mm] 3.125
increment to store M(t) 0
concomitant fields [Gmax/B0] 0
random noise [%] 0
MotionTrajectory variable
FlowTrajectory
ROI [px] 0
Diffusion File
Multiply
☑ EPI reordering?
Sample
Image

Figure 4.9: JEMRIS simulator framework.

In this GUI, mostly the parameters about the sample should be set. In the present case, in order to compensate for the effect of long acquisition in EPI and check the results in an ideal situation, T_2 and T_2^* are considered to be the same and equal to 100 ms. T_1 is 1000 ms, the sample is a 200 mm cylinder which is made out of voxels with the size of 3.125 mm. After running the simulation, the results can be seen as the magnitude and phase of the image, signal, or k-space. In Figure 4.10, the phase and magnitude of the MR image are shown.

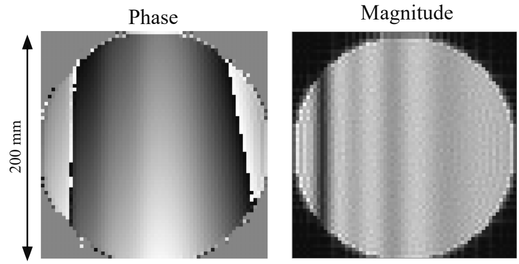

Figure 4.10: Magnitude and phase of the image obtained from the JEMRIS simulator.

After doing postprocessing, the result is compared with desired TS, and the comparison shows good agreement (Figure 4.11).

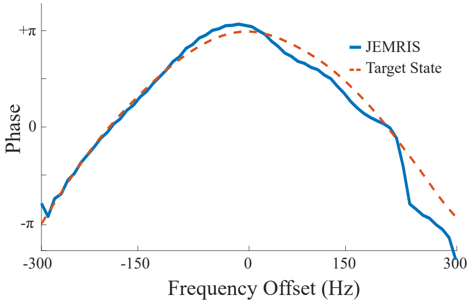

Figure 4.11: Comparison between the phase profile obtained from JEMRIS and the TS.

In the next step, the sequence is written in the imaging software ParaVision 360® of an 11.74 T Bruker® NMR spectrometer in order to evaluate the feasibility of the pulse in experimental situations. A pulse sequence is designed upon a standard FLASH (Fast Low Angle SHot) imaging pulse sequence, in which the excitation pulse and slice selection gradient are replaced by OC RF pulse and OC gradient, respectively. The sample is a 5 mm NMR tube with the inner diameter of 4.375 mm. The OC gradient is set such that it produces a range of 600 Hz (from -300 to 300) over the entire sample (in 4.375 mm). The phase and magnitude of the MR image are shown in Figure 4.12.

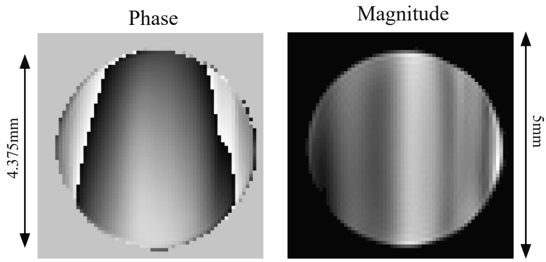

Figure 4.12: Magnitude and phase of the image obtained from experimental results.

In Figure 4.13, experimental and simulation results are compared with the TS. The comparison shows good agreement between them.

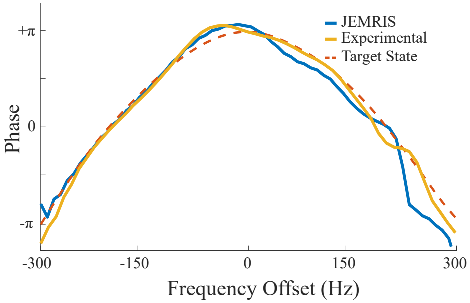

Figure 4.13: Comparison between the phase profile from JEMRIS, experimental results, and the TS.

In the end, it has to be mentioned that one of the most important parameters that must be taken into account is the power of the OC RF pulse. Due to the importance of this issue, it will be explained in the ensuing section separately.

4.3.6 Power adjustment of OC excitation pulses

In the design of an OC excitation pulse, the phase pattern of the TS would be obtained at a certain flip angle. That is why it is essential to calculate the required excitation power. By convention, the reference power is calculated by the following equation [60],

$$P_{\text{ref}} = \left(\frac{90^\circ}{\theta}\right)^2 \times \left(\frac{\tau}{1ms}\right)^2 \times S_{\text{int}}^2 \times P, \tag{4.20}$$

where P_{ref} is the reference power, θ is the flip angle, S_{int} is the normalized shape integral of the pulse (which is 1 for a block pulse), and P is the power. For an OC RF pulse, Equation 4.20 might be misleading. The reason is that, in the opposite of traditional RF pulses, an OC RF pulse needs to go through an unconventional trajectory. In order to make this issue clearer, we will take a look at the trajectory of an on-resonance voxel under the OC RF pulse shown in the last subsection (Figure 4.6). The trajectory looks like the following in Figure 4.14 IF we use the correct power for the excitation pulse.

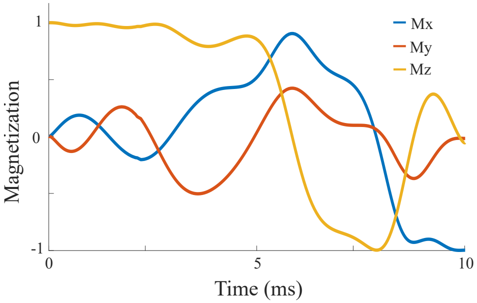

Figure 4.14: Magnetization evolution of an on-resonance spin isochromat excited by the OC pulse shown in Figure 4.6 (Adapted from [57]).

In the current case study, the TS would be attained at the XY-plane, which is conventionally considered as a 90° flip angle or one of its multiples.

However, in case we consider the flip angle equal to 90° and calculate the reference power from Equation 4.20, the magnetization would have the evolution shown in Figure 4.15.

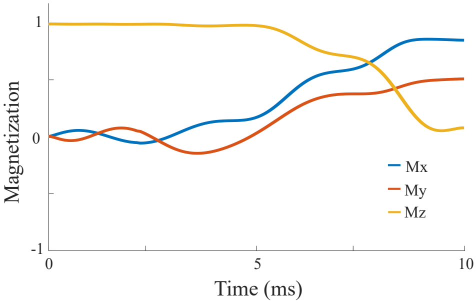

Figure 4.15: Magnetization evolution of an on-resonance spin isochromat excited by the OC pulse shown in Figure 4.6 yet with the incorrect reference power (calculated from Equation 4.20 based on a 90° excitation).

Making a comparison between Figures 4.14 and 4.15 reveals that although they both end up at the XY-plane, they have different trajectories. Even though following the former leads to the correct phase pattern, which was shown in Figure 4.13, going through the latter results in the phase pattern shown in Figure 4.16.

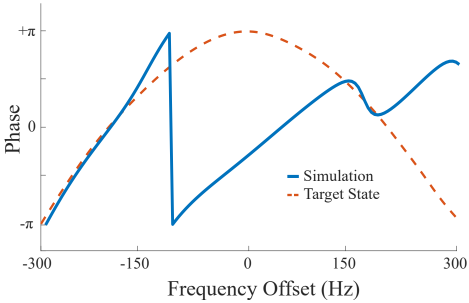

Figure 4.16: Comparison between the phase profile resulting from the OC pulse with the incorrect reference power and the TS.

Also, the effect of using the incorrect power is proved by the JEMRIS simulator and experimental results as well.

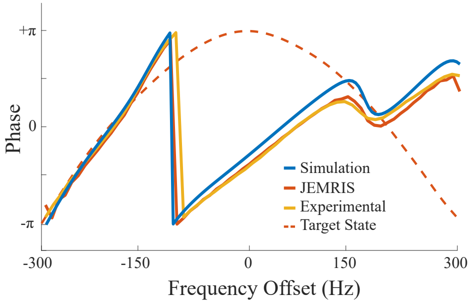

Figure 4.17: Comparison between the phase profiles resulting from the OC pulse with the incorrect power in simulation, JEMRIS, and experimental results.

From Figure 4.17, it is clear that an incorrect power doesn't lead to the aimed TS. In the current OC problem, the TS is designed such that the desired phase pattern would be achieved at XY-plane, which is normally considered as one of the multiples of a 90° flip angle. But if we take a closer look at the evolution in Figure 4.14, we see that it is actually not a normal 90° excitation. It passes through the 90° then goes to 180° and finally comes back to an angle even smaller than 90°, and finally ends up at the XY-plane. So, if we set the flip angle equal to 90°, the power calculated from Equation 4.20 is enough for the evolution shown in Figure 4.15 but not for the one in Figure 4.14. Now, the question is how we can calculate the correct reference power in such cases.

First, it has to be explained how an RF pulse is stored in the ParaVision® imaging software and how the automatic power adjustment routine available in ParaVision® works. The pulse is stored as a text file and consists of two columns, including the normalized magnitude and phase of the pulse. When we run the adjustment routine, it runs a nutation spectrum experiment based on a block pulse, in which τ is 1, θ is 90, S_{int} is 1. As a result, the power found from the nutation spectrum is the reference power (P_{ref}) in Equation 4.20. Now, suppose we aim to use any other pulse for any value for θ and pulse duration τ. In that case, we can calculate the corresponding required power P since we already have P_{ref}, and S_{int} can be calculated from the shape of the pulse.

To calculate the required power for an OC RF pulse, there are two solutions. The first one is to use the simulator to find a correction factor between the power calculated by Equation 4.20 and the correct power. After obtaining the shape of the OC RF pulse, it has to be normalized and then stored as an RF pulse in ParaVision®. To calculate the correction factor by the simulator, first, we need to find the reference power of the simulator. By using a block pulse (bp) and based on Equation 4.20, we can calculate the reference power P_{ref}. Using the calculated P_{ref}, we can obtain the required power P for the OC pulse from Equation 4.20. The ratio between the value of P and the maximum value in the non-normalized OC pulse would be the correction factor by which the reference power must be multiplied. The same calculations show that the calculated P_{ref} of OC pulse (Figure 4.6) must increase by a factor of 12.5 to result in the correct magnetization evolution. It corresponds to a flip angle of 318°.

Another solution would be to do a nutation spectrum with the simulator and mark the point that it reaches 100% of the power. Then, the same evaluation can be carried out experimentally by the spectrometer. By comparing the nutation spectra, the required power can be found directly. Such a comparison is shown in Figure 4.18.

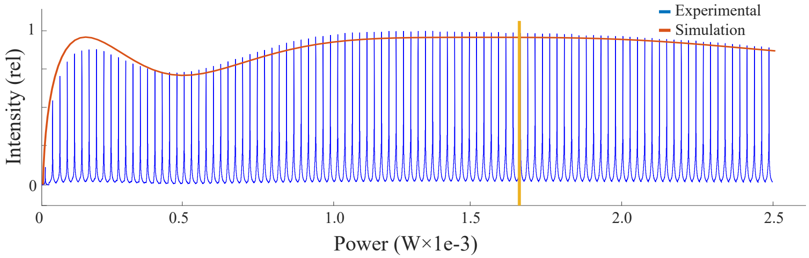

Figure 4.18: Experimental nutation spectrum (blue curve) versus simulation (orange curve). The yellow line shows the required power.

As it can be concluded from Figure 4.18, in this case, the required power for a 90° excitation is $1.66\,\mathrm{W}$.

4.4 Application of optimal control theory in flow MRI

As mentioned at the beginning of the chapter, in MR, OCT is a recipe to design the required shaped excitation pulses to reach the desired state at the end of the excitation time. In other words, OCT helps us to find the requisite components of the excitation pulse $\left(\vec{B}_x, \vec{B}_y\right)$ at each time element to reach the needed position in the Bloch sphere.

In applying OCT to flow MRI, there are a number of challenges. First, we need a mathematical model that explains how the velocity can be encoded into the phase of the signal. Then, we need to deal with slice selectivity. In the end, the phase uniformity along the slice thickness has to be taken into account, which is the most challenging part of the OCP. All of these aspects make the problem sophisticated and even over-constrained. That is why, in this study, the OCP is divided into two steps. In the first step, we just focus on the velocity encoding of the central plane of the slice, and in the second one, encoding of the rest of the slice is addressed.

4.4.1 Mathematical model

To apply the OCT to any application, the first requirement is a mathematical model. In the current section, the designed pulse is supposed to make a phase contrast between voxels with different velocities, and in order to establish the contrast, the pulse needs to see a difference between voxels with distinct velocities. To make this difference, a gradient is applied in the velocity encoding direction. As a result of the gradient, voxels with dissimilar velocities go through non-identical ranges of frequencies, starting from 0 to a certain frequency. At $t = 0$, the center of all voxels is considered to be on-resonance. While during the excitation, the stationary voxel will remain still on-resonance, a voxel with a certain velocity goes through a certain frequency range depending on its velocity.

The OC RF pulse benefits from this dissimilarity to produce the required contrast in the image. So, it helps the pulse to guide the magnetization and establish a relationship between the velocity of the voxel and its phase. As an instance, the voxel with V_{enc} velocity ends up with the phase equal to π at $t = t_f$ and the one with $-V_{\text{enc}}$ comes to phase of $-\pi$. By analogy, the voxels that flow between the range of $-V_{\text{enc}}$ to V_{enc} would have the phase between $-\pi$ and π. The relationship doesn't need to be necessarily linear yet bijective. In the following, a graphical description shows how flow in a pipe can be encoded into the phase of signal (Figure 4.19). It shows that the same flow profile is imprinted into the phase of the image. So, it follows a linear relationship despite the fact that it is not necessarily required.

4.4.2 Optimal control problem definition – 1st step

In the first step of OCP, only the magnetization evolution of the pixels of the central plane, which is on-resonance at $t = 0$, is taken into account. However, by applying the slice selectivity, a certain thickness will be excited. The magnetization evolution of the rest of the slice will be discussed at the end of the current section (Section 4.4.2) and will be addressed in the second step of OCP, Section 4.4.3.

Slice selection

In the previous section, the mathematical model of OCT was explained. The next challenge will be the slice selectivity. As discussed, the applied gradient is used to encode velocity into phase. Now, the question is how we can achieve the slice selectivity. In order to fulfill this requirement, a constraint is applied to the OCP in order to restrict the bandwidth of the excitation pulse (Figure 4.20). As a result, just a certain thickness of the sample will be excited, and the OC pulse will be a slice-selective pulse.

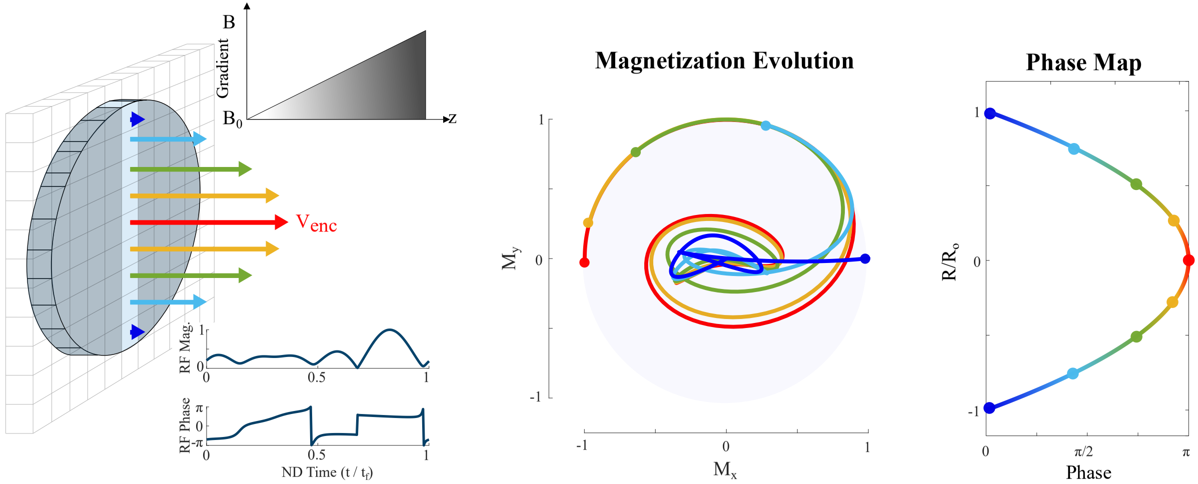

Figure 4.19: Graphical representation of the mathematical model of optimal control problem (OCP). A gradient is applied in the velocity encoding direction. As a result, voxels with different velocities go through unique ranges of frequencies. The OC excitation pulse, which is applied during the gradient oscillation, uses this uniqueness to guide them through distinct trajectories in order to place them at the specific points that are already defined in the TS. The magnetization evolution for the voxels with different velocities is shown in the middle. Also, the final phase profile is presented at the right. As indicated by the figure, a parabolic flow profile leads to a parabolic phase profile. It means a linear relationship between velocity and phase is established by the OC excitation pulse and gradient (Adapted from [57]).

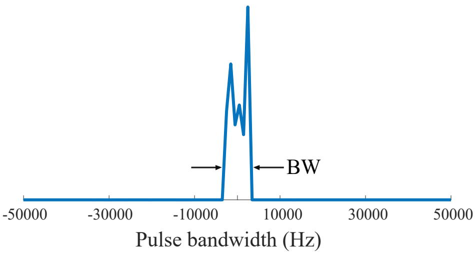

Figure 4.20: Fourier transformation of the OC flow encoding excitation pulse with the duration of 1 ms. The bandwidth (BW) is limited to make the pulse slice selective (Adapted from [57]).

Target state and cost function definition

Now that we determined the mathematical model, we are able to define the TS. In the first step of the OCP, a linear relationship between the velocity and phase of the pixels is considered; see Figure 4.21.

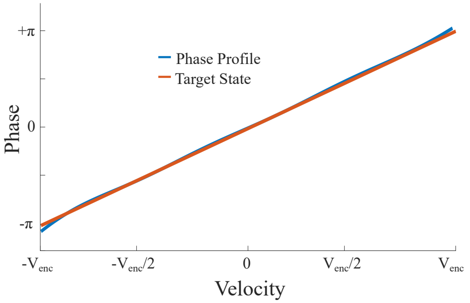

Figure 4.21: Relationship between phase and velocity of the central plane. The orange line shows the TS, and the blue curve represents the achieved relationship (Adapted from [57]).

Since this study is based on the finite element method (FEM), the range of velocities has to be divided into a number of elements, here 127. The velocity discretization is accomplished by the following equation,

$$V_i = \frac{i-64}{63} V_{\text{enc}}, \qquad i = 1:127, \tag{4.21}$$

in which i is the pixel counter, and V_i is the velocity.
As it was explained in the mathematical model, due to the gradient, each pixel goes through a specific range of frequencies starting from 0 to a certain value (depending on its velocity). In this study, the multiplication of the maximum value of this range by the excitation time is defined as a dimensionless key parameter and is denoted by Δ_i. The reason for such a definition is that if the effect of relaxations is negligible, an excitation pulse with the length of t_f under the gradient with the power of G performs the same job with another excitation pulse with the same shape and the length of $t_f/2$ which is under gradient with the power of *2G*. Based on the definition, Δ_i would be a function of Gyromagnetic ratio γ, applied gradient G, excitation (encoding) time t_f, and displacement over the excitation time δx_i. So, it can be calculated by the following equation,

$$\Delta_\mathrm{i} = \frac{\gamma}{2\pi} G \cdot \delta x_\mathrm{i} \cdot t_f = \frac{\gamma}{2\pi} G \cdot V_\mathrm{i} \cdot t_f^2. \tag{4.22}$$

Based on Equation 4.22, a new term, namely Δ_enc, which is the maximum frequency experienced by the fastest pixel, is defined,

$$\Delta_\mathrm{enc} = \frac{\gamma}{2\pi} G \cdot V_\mathrm{enc} \cdot t_f^2. \tag{4.23}$$

As shown in Figure 4.21, the goal is to establish a linear relationship between velocity and phase, which leads to phase equal to π for a voxel with the velocity of V_enc and $-\pi$ for the one with the velocity of $-V_\mathrm{enc}$. As a result, the TS can be defined as the following,

$$\phi_\mathrm{i} = \frac{V_\mathrm{i}}{V_\mathrm{enc}} \pi, \tag{4.24}$$

where ϕ_i is the phase of the pixel, and V_i is the velocity. In addition, the flip angle is considered equal to 90°. The quadratic difference of any deviation from this relationship is defined as the cost function.

$$C\left(\vec{B}_x,\vec{B}_y\right)=\frac{1}{N}\sum_{\nu=1}^{N}\left\|\vec{M}_\nu\left(t_f\right)-\vec{M}_{\mathrm{TS}_\nu}\right\|^2, \tag{4.25}$$

where C is the cost function, B_x and B_y are the x and y components of the RF pulse, $\nu \in \{1,\ldots N\}$ is the index of pixels, $\vec{M}_\nu\left(t_f\right)$ is the magnetisation at t_f for pixel ν, and $\vec{M}_{\mathrm{TS}_\nu}$ is the TS of the pixel ν. As it is implied from Equation 4.25, the goal is to minimize and preferably zero out the cost function since it means that the state at $t=t_f$ is the TS.

OC gradient selection and RF pulse generation

The excitation pulse is discretized into 300 time elements. So, in total, the control field has 600 variables as x and y components of the RF pulse $\left(B_x(t),B_y(t)\right), t\in(t_1,t_2,\ldots,t_{300})$. In the first try, the duration of the pulse t_f is considered to be equal to 1 ms.

The next step would be choosing Δ_{enc}. A series of simulations are run, and the value of Δ_{enc} is sweeping over experiments in order to find the best value to zero out the cost function since unsuitable values of gradient can make the problem over-constrained. The pulse length is 1 ms, and the maximum range of frequency is being swept from 300 to 8200 Hz which corresponds to Δ_{enc} from 0.30 to 8.2. The simulations are run for 40 iterations. The value of cost versus the value of Δ_{enc} is presented in Figure 4.22.

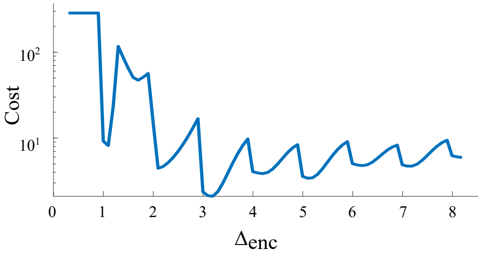

Figure 4.22: Value of cost function after 40 iterations versus Δ_{enc} (Adapted from [57]).

As it is shown in Figure 4.22, at Δ_{enc} equal to 3.2, the cost function takes its minimum.

Also, it is noteworthy to mention that the excitation time and experienced range of frequency, and hence corresponding Δ_{enc}, don't correspond to any specific V_{enc}. Here, an example is provided to clarify the idea. First, we should set the V_{enc}, for example $1\,\text{mm}\,\text{s}^{-1}$. Then, we can set the excitation time, for example, 1 ms. Based on the definition, $\Delta_{\text{enc}} = \gamma/2\pi \cdot G \cdot V_{\text{enc}} \cdot t_f^2$, and it is equal to 3.2. So, the applied gradient, $\gamma/2\pi \cdot G$, would be $3.2/0.001^2/1$, equal to $3200\,\text{kHz}\,\text{mm}^{-1}$. The same calculation applies for any other value of V_{enc}.

As a result of the evaluation shown in Figure 4.22, $\Delta_{\text{enc}} = 3.2$ is chosen. After running Algorithm 1 for 100 iterations, the cost drops to 0.0054, which can be considered as a negligible deviation from the TS. The convergence of the cost function is shown in Figure 4.23.

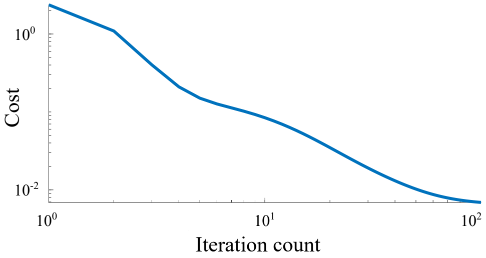

Figure 4.23: Convergence of the cost function versus the number of iterations (Adapted from [57]).

Also, the magnitude and phase of the generated RF pulse are shown in Figure 4.24. It was explained that it is possible to exchange the excitation time and OC gradient, which means that, using the same excitation shape, we can reduce the time and increase the gradient or vice versa. So, the time axis is shown in the dimensionless time units (ND).

So far, an RF pulse has been designed in order to encode the velocity of the pixels on the central plane into the phase of the signal. But, the effect of the pulse on the rest of the sample should be evaluated as well. Assuming

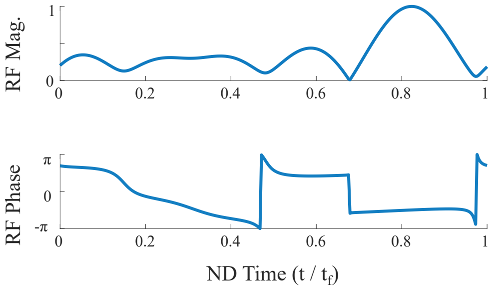

Figure 4.24: Magnitude and phase of the OC flow encoding excitation pulse to reach the relationship shown in Figure 4.21 (Adapted from [57]).

that the velocity change along the thickness is negligible, the off-resonance planes of the sample experience the same frequency range plus/minus a certain offset. The offset would be bigger for the planes that are placed farther from the central one and less for the ones that are closer. For example, the pixel which states at the central slice and moves with V_{enc} velocity goes through $[0\,,\Delta_{\text{enc}}]\,/t_f$ range of frequency and consequently has the phase equal to π at t_f, but a pixel with the same velocity which is not placed at the central plane goes through $[0+X\ ,\ \Delta_{\text{enc}}+X]\,/t_f$; as a result of the offset (X), the pixel would not have the same phase. It means that there will be phase dispersion in the slice direction. At first, this phase dispersion should be assessed, and then OCT would be used again to minimize the corresponding adverse effects.

The magnetization evolution is simulated, and the results for three different velocities, $-V_{\text{enc}}$, 0, and V_{enc} are presented in Figure 4.25. The profile of the signal magnitude in the slice direction is shown in orange, and it shows the slice selectivity of the OC RF pulse. The phase profile is illustrated in blue. The phase of the central plane is indicated by a yellow dash. As expected, the phase of the corresponding pixels is equal to $-\pi$, 0, and π, respectively; however, the phase of off-center planes is different. There is an almost linear change in the value of phase over the slice direction.

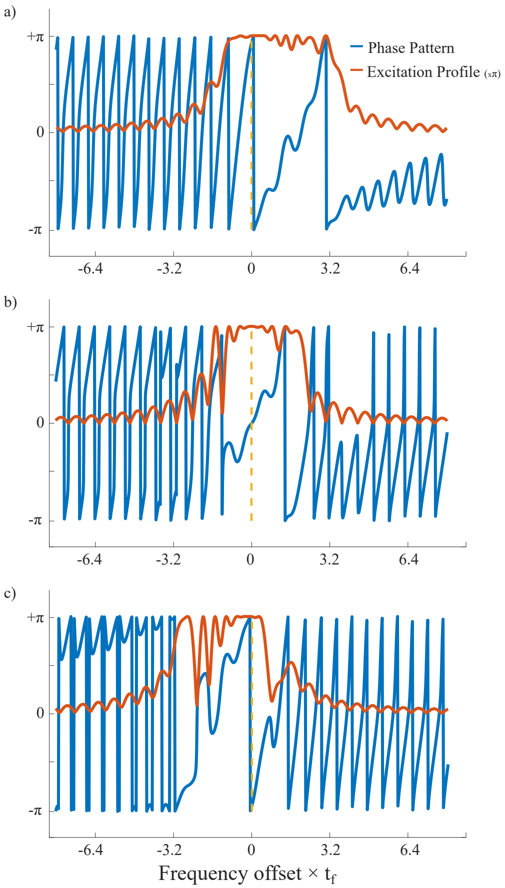

Figure 4.25: Phase and magnitude profile of the MR signal along the slice direction for three different velocities, a) $-V_{\mathrm{enc}}$, b) 0, and c) $+V_{\mathrm{enc}}$. The yellow dashed line shows the on-resonance plane (Adapted from [57]).

Nevertheless, in the end, what is detected by the spectrometer is the vector summation of the signal emitted from the whole slice. So, the summation over the thickness is calculated, and its phase is shown in Figure 4.26.

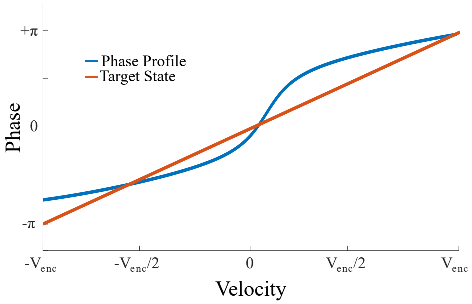

Figure 4.26: Relationship between phase and velocity (Adapted from [57]).

As the results show, the RF pulse establishes a non-linear yet bijective relationship between phase and velocity. The nonlinearity is not an issue and can even be helpful in some cases to enhance the SNR for voxels with a certain range of velocity (in this case, for slow-moving voxels). But, bijectivity is necessary, which has been achieved by the pulse.

Also, the magnitude of the vector summation is evaluated as well. The relationship between magnitude and velocity is shown in Figure 4.27.

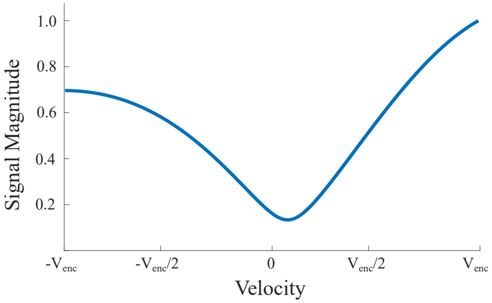

Figure 4.27: Magnitude of the MR signal versus velocity (Adapted from [57]).

The results in Figure 4.27 show that there is a signal dropout, especially in the voxels with slow velocities. The designed pulse is used to perform some experiments and evaluate the feasibility of the pulse. The results are shown in the following subsection.

Results and discussion – 1st step

In this subsection, the RF pulse, designed in the last section, is used to perform some experimental assessments. The RF pulse is imported in ParaVision®, and experiments are performed on an 11.74 T Bruker ® spectrometer. The sample is 3D printed by a Creality LD-002H resin 3D printer and consists of two cylindrical channels with 3.3 mm diameters. The pulse length is 2 ms, $V_{\text{enc}} = 50\,\text{mm}\,\text{s}^{-1}$, and hence the gradient is $16\,\text{kHz}\,\text{mm}^{-1}$. The phase and magnitude of the corresponding MR image are shown in Figure 4.28.

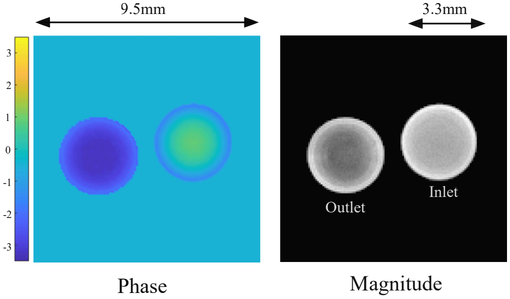

Figure 4.28: Phase and magnitude of the image taken by the OC pulse shown in Figure 4.24 at $V_{\text{enc}} = 50\,\text{mm}\,\text{s}^{-1}$. The sample holder is shown in Figure 4.40 a).

The result is evaluated in Figure 4.29, and it shows that it is not in good agreement with the reference line shown in the figure.

To find out the reason for this mismatch, we have to take a closer look at the flow encoding process. In order to do so, the flow is simulated in a different way. To explain it, we get back to the mathematical model of flow encoding (Subsection 4.4.1). As explained, due to the movement, the voxels go through a certain range of frequencies. In the end, the vector summation of all planes, including central and off-center ones, leads to the non-linear relationship between phase

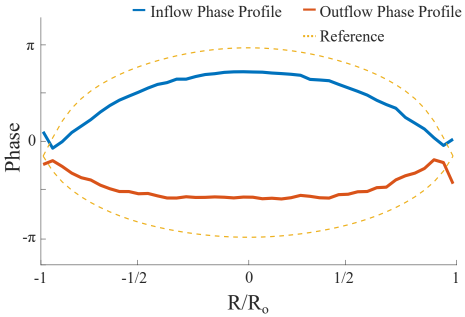

Figure 4.29: Phase profile of the MR image shown in Figure 4.28.

and velocity (Figure. 4.26). We need to check the encoding process in the off-center and central planes in more detail, but the problem is that what the coil detects is the summation of all of them. In the following, to reveal more details about them, flow is simulated on a stationary sample.

In the current model, instead of the sample moving through the gradient direction, the sample is stationary, but the gradient is increasing. A sagittal image is obtained, in which, during the excitation time, an increasing gradient is applied in the axial direction to mimic the effect of movement, and a constant gradient is applied in the coronal direction to simulate the effect of the gradient on the off-center planes.

In Figure 4.30, the configuration of the gradients is shown. The effect of all on-center and off-center flowing planes under OC RF pulse is mimicked by an increasing gradient. In this simulation, the flow profile is considered to be linear along the y direction. The effect of being off-center will be presented in the x direction by the constant gradient.

Suppose we apply the gradient shown in Figure 4.30 during the excitation and perform an imaging sequence afterward. In that case, due to the increasing gradient, the row in the coronal direction has the same situation as the central plane in flow encoding and experiences the frequency range of $[0\,, \Delta_{\text{enc}}]\,/t_f$. Due to the constant gradient, any shift in that direction adds an offset to the

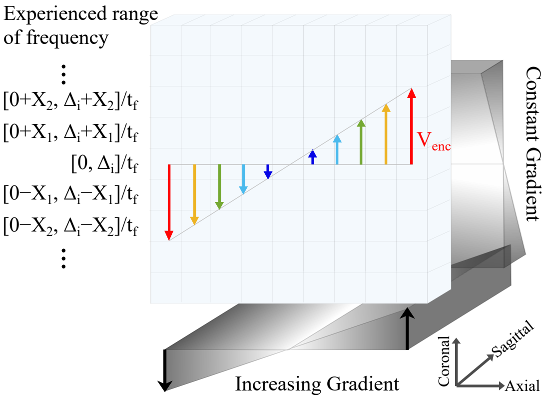

Figure 4.30: Explanatory illustration of simulating flow encoding on a stationary sample.

experienced range of frequency $[0+X_i\ ,\ \Delta_{\text{enc}}+X_i]/t_f$. This image gives us a comprehensive conception of the magnetization evolution along the thickness direction.

To evaluate the validity of the results in Figure 4.25, the same pulse sequence is simulated in JEMRIS. The results shown in the following figures are compared with the present simulation.

Figure 4.31 shows a very good agreement between the current simulation and the one from JEMRIS. In the next step, the pulse is imported in ParaVision®, and the measurements are performed in experimental conditions with an 11.74 T Bruker® spectrometer on a 5 mm NMR tube filled with distilled water. In order to eliminate the effect of any imperfection, an experiment is performed without increasing the gradient and used as a reference. The results of experiments with increasing gradients will be deducted by the reference.

Even though Figure 4.32 b) to d) and g) to i) show just a small deviation from the simulation in experimental results, the corresponding phase of vector summation of the signal shown in Figure 4.32 j) shows a considerable deviation. As shown in the figure, the experiment is repeated two times.

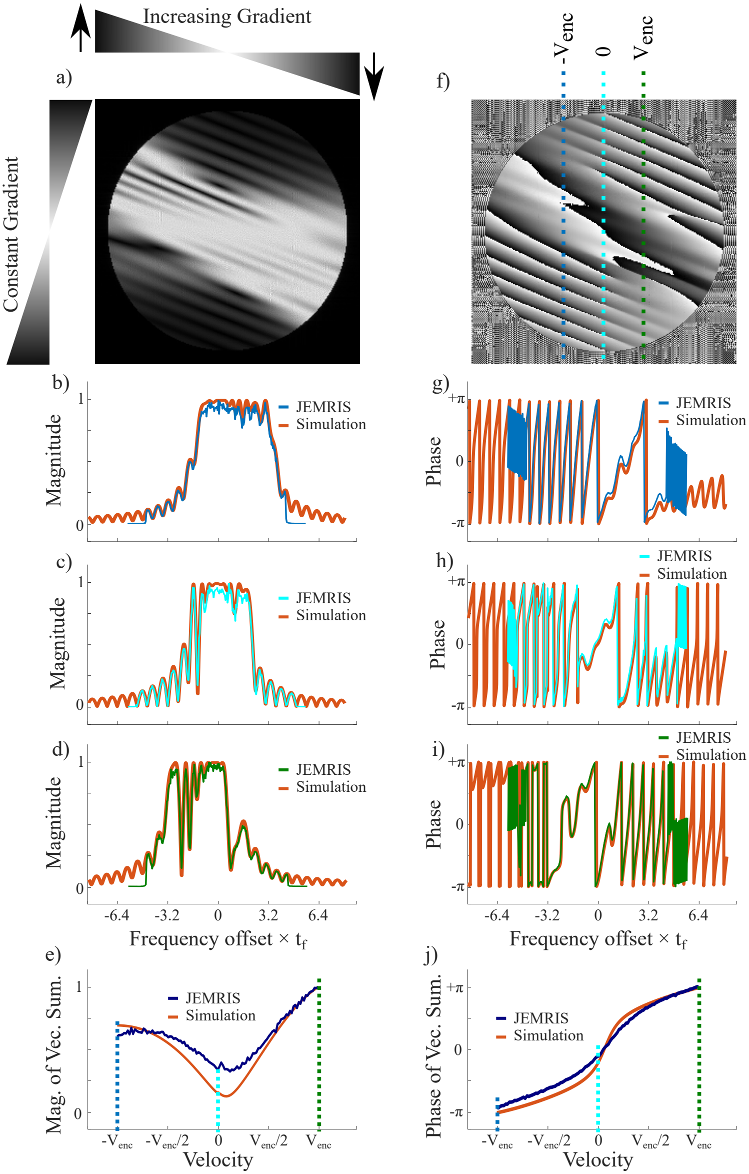

Figure 4.31: Magnitude (a) and phase (f) of the MR image obtained from the JEMRIS simulator. The magnitude (b-d) and phase (g-i) are plotted for three different velocities ($-V_{\text{enc}}$, 0, and $+V_{\text{enc}}$). Also, the magnitude (e) and phase (j) of the vector summations of the whole slice are presented.

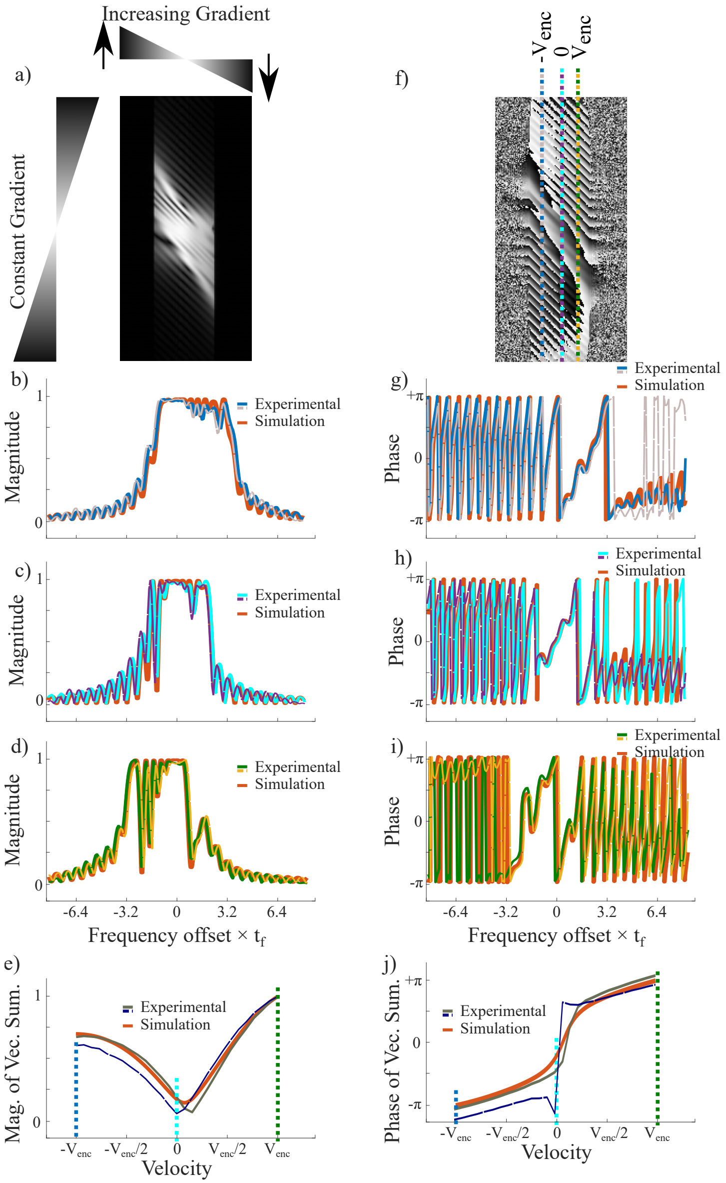

Figure 4.32: Magnitude (a) and phase (f) of the MR image obtained from the experimental results. The magnitude (b-d) and phase (g-i) are plotted for three different velocities ($-V_{\mathrm{enc}}$, 0, and $+V_{\mathrm{enc}}$). Also, the magnitude (e) and phase (j) of the vector summations of the whole slice are presented.

Although there is just a small difference between the two experimental cases, the final result, shown in Figure 4.32 j), looks different. The main reason for this mismatch is assumed to be the loss of signal in the slice direction, which results in low SNR and makes the final phase response inconsistent.

The non-uniformity in phase profile across the thickness, which causes inconsistency in net-phase response, is clear in Figure 4.25. The second step of OCP is to enhance the uniformity of the phase so as to improve the SNR and make the phase of vector summation of the signal more consistent.

4.4.3 Optimal control problem definition – 2nd step

In the first step of OCP, the OC RF pulse is able to encode the velocity of the sample into the MR phase in the theoretical conditions. However, due to the non-uniformity in the phase profile across the slice thickness, the pulse doesn't perform the same job in the experimental condition. In the second step of OCP, OCT is utilized again in order to improve the phase uniformity; see Figure 4.25. Clearly, the ideal situation is to have a completely uniform phase profile. But, the problem is that such a TS generates an over-constrained OCP. To avoid this issue, it is tried to make the minimum changes in the results which were already achieved. Taking a look at the phase dispersion in Figure 4.25 shows that there is an almost linear phase dispersion for voxels with different velocities. In order to make the problem less constrained, the new RF pulse is asked to produce the same phase profile plus (just) a linear change in the slice direction. Based on that, the new TS is defined. In Figure 4.33, a comparison is made between the current phase profile and the newly targeted one.

As Figure 4.33 shows, adding a linear change to the phase profile makes it much more uniform. Also, the ideal case is shown by a yellow dashed line, but since it leads to an over-constrained OCP, it is not considered the TS. In the following, the RF pulse designed in the first step is used as the initial guess in the GRAPE algorithm.

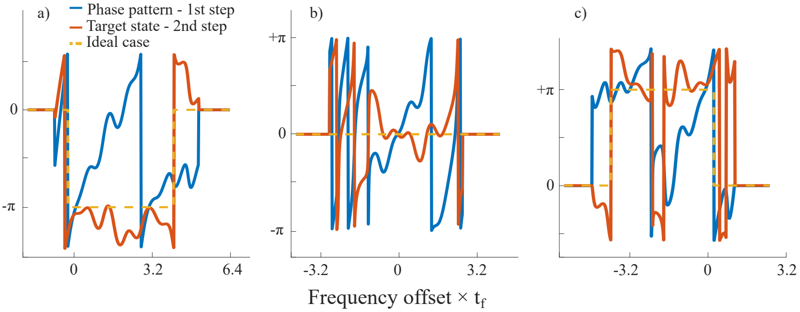

Figure 4.33: Phase profile of the MR signal along the slice direction for three different velocities, a) $-V_{\mathrm{enc}}$, b) 0, and c) $+V_{\mathrm{enc}}$. The profile is shown for the TS of the 2nd step of OCP and the one achieved after the 1st step. The yellow dashed line shows the ideal phase profile.

The convergence of the cost function to its minimum is shown in Figure 4.34. It shows that after 100 iterations, the cost function holds its minimum. The issue is that the cost doesn't go to zero, which means that the OCP is still over-constrained. But, since there is a reduction in the cost function, there should be an improvement in the uniformity. In Figure 4.35, the improvement is evaluated by making a comparison between the results of the second step and that of the first step. The results show a considerable improvement in the uniformity of phase along the slice direction.

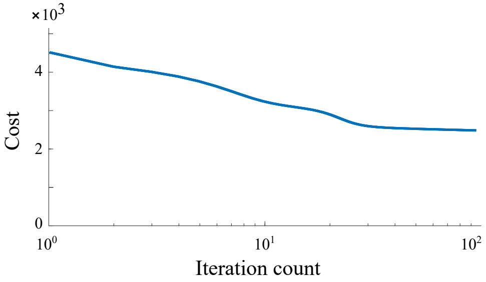

Figure 4.34: Convergence of the cost function versus the number of iterations (2nd step of OCP).

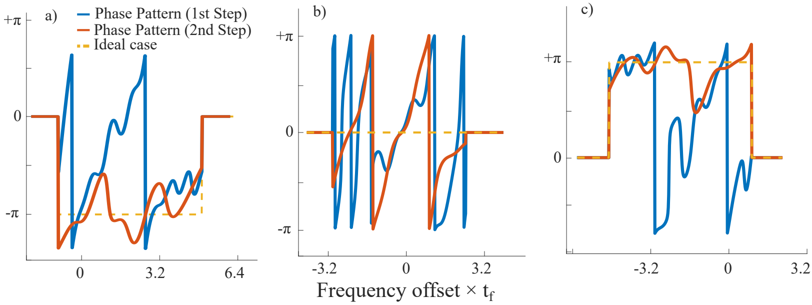

Figure 4.35: Phase profile of the MR signal along the slice direction after the 1st and 2nd step of OCP for three different velocities, a) $-V_{\text{enc}}$, b) 0, and c) $+V_{\text{enc}}$. The yellow dashed line shows an ideally uniform phase profile (Adapted from [57]).

In the following, the phase of vector summation of the signal emitted from the whole slice is assessed to check the relationship between velocity and phase, particularly the bijectivity. In Figure 4.36, the dependence of the injected phase on the velocity is illustrated, showing a bijective nonlinear relationship between the phase and velocity.

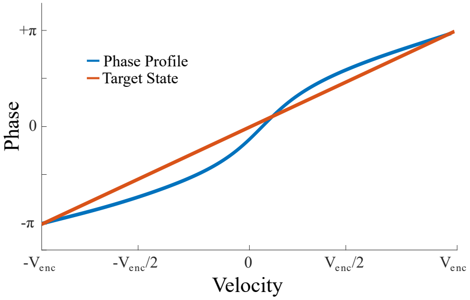

Figure 4.36: Relationship between phase and velocity after the second step of OCP (Adapted from [57]).

In Figure 4.37, the magnitude of the signal is compared with that of the first step, demonstrating a substantial enhancement in the SNR. Also, the final shape of the optimal control flow encoding excitation pulse is shown in Figure 4.38.

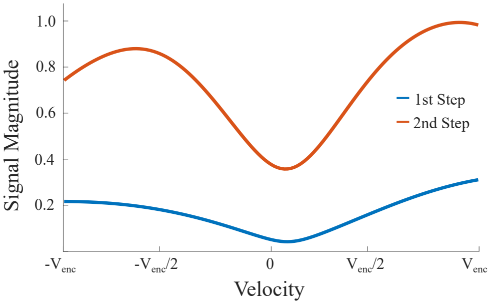

Figure 4.37: Magnitude of the MR signal versus the velocity after the 1st and 2nd step of OCP (Adapted from [57]).

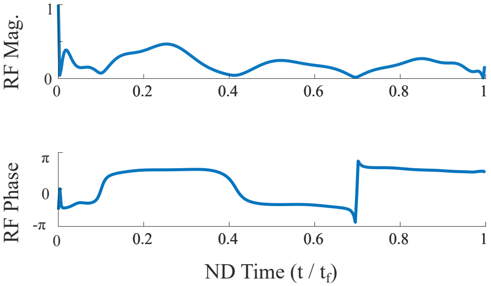

Figure 4.38: Magnitude and phase of the OC pulse after the 2nd step of OCP (Adapted from [57]).

In Section 4.3.6, the power adjustment of OC excitation pulses was discussed. It must be checked if the adjustment of the power is required. A similar simulation is performed for the OC pulse. The important point in the power adjustment of the current pulse is that the cost function of the second step of the OCP didn't go to zero, and hence, there is a deviation from the TS, which is designed to reach the desired phase profile at a 90° flip angle. But, due to the deviation, the phase profile would be achieved at 115°. Figure 4.39 shows the trajectory of an on-resonance voxel under the excitation pulse shown in Figure 4.38. Therefore, the power has to be multiplied by 1.65 to reach the required flip angle (115°).

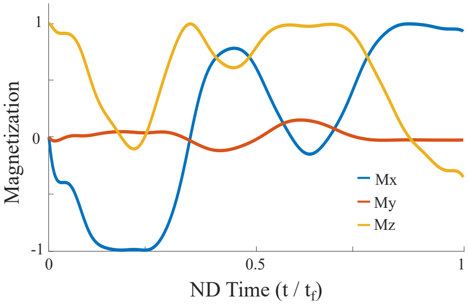

Figure 4.39: Magnetization evolution of an on-resonance spin isochromat excited by the OC pulse shown in Figure 4.38 (Adapted from [57]).

4.4.4 Results and discussion

In this section, the designed pulse is tested in experimental conditions. Measurements are carried out on a Bruker® 11.74 T vertical wide bore superconducting magnet with a 10 mm insert mounted on a Micro5 probe equipped with a 3-axis gradient.

In order to have a completely stable flow behavior and to avoid any fluctuation in the flow rate, a syringe pump is used. Two sample holders are 3D-printed by a Creality LD-002H resin printer to perform the measurements. A graphical illustration of the samples is presented in Figure 4.40. The first one consists of two identical straight channels, one as the inlet and the other one as the outlet of flow. The diameter of the channels is 3.3 mm. In the second sample holder, the cylindrical volume is divided into a central cylindrical channel as the inlet and an annular channel as the outlet.

The next step is pulse sequence compilation. The OC excitation pulse can be used on any imaging pulse sequence. However, some modifications are needed. In this study, the RF pulse is used on a FLASH pulse sequence, in which the RF pulse, slice selection, and refocusing gradients are replaced by the OC RF pulse and OC gradient. Compared to a conventional flow MRI pulse sequence, in which a bipolar gradient is added to a traditional imaging sequence, slice selective excitation pulse is replaced by an OC RF pulse, and slice selection and

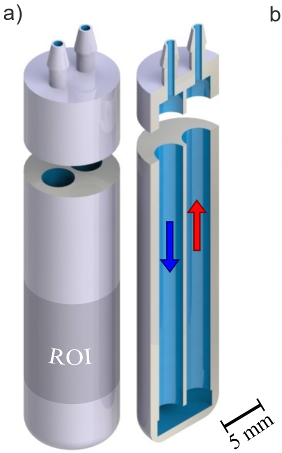

Figure 4.40: Illustration of the two flow measurement sample holders. The first one (a) has two identical cylindrical channels with the inner diameter of 3.3 mm, and the second one (b) has an annular cross-section whose inner channel has the diameter of 3.7 mm, and the outer channel has the inner diameter of 5.2 mm and outer diameter of 7.5 mm. The outer diameter of both sample holders is 10 mm (Adapted from [57]).

bipolar gradients are replaced by the OC gradient. A comparison between the pulse sequence used in the current method and conventional flow MRI is made in Figure 4.41.

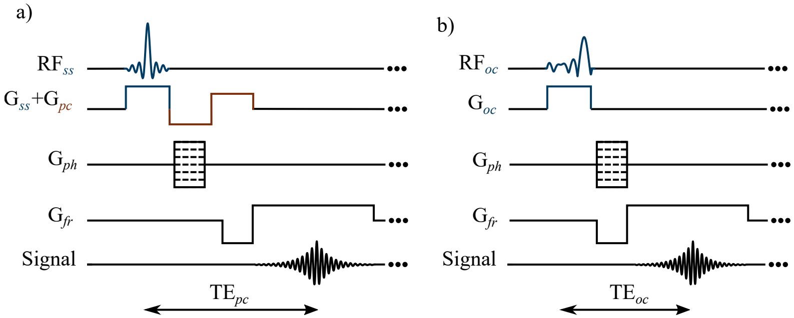

Figure 4.41: Schematic representation of a) a phase contrast and b) an optimal control flow imaging sequence (Adapted from [57]).

As a proof of concept, the first experiment is performed on the sample holder a) in Figure 4.40. In this experiment, the flow rate in the syringe pump is $13\,\mathrm{mL\,min^{-1}}$, which results in the maximum velocity of $50\,\mathrm{mm\,s^{-1}}$ in the center of the parabola of the flow profile. The corresponding Reynolds number is $\mathrm{Re} = 63$. The OC pulse length is $2\,\mathrm{ms}$ and corresponding OC gradient is $16\,\mathrm{kHz\,mm^{-1}}$ to reach $\Delta_{enc} = 3.2$ since $V_{\mathrm{enc}} = 50\,\mathrm{mm\,s^{-1}}$. As discussed, the pulse is designed based on experiencing a certain range of frequencies by the fastest voxel. Any field inhomogeneity can disturb this assumption. In order to address this issue, a measurement is performed on a stationary sample, and the phase map will be used as a reference. In the following, phase maps of the measurements will be deducted by the reference map to eliminate the undesired effects of inhomogeneities. In the end, a signal mask (threshold$=3\%$) is used to remove the voxels with a high effect of partial volume from the phase map. The experimental results, including phase maps and magnitude, are presented in Figure 4.42.

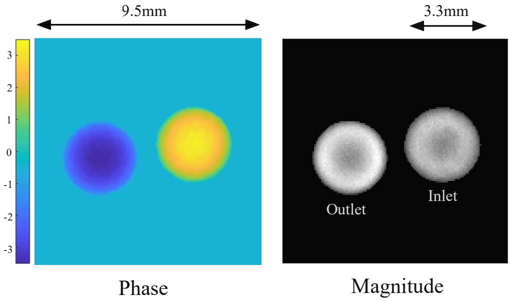

Figure 4.42: Phase and magnitude of the image taken by the OC pulse shown in Figure 4.38 at $V_{\mathrm{enc}} = 50\,\mathrm{mm\,s^{-1}}$. The sample holder is shown in Figure 4.40 a) (Adapted from [57]).

The relationship between phase and velocity is not linear. So, the phase map shown in Figure 4.42 has to be interpreted to velocity based on the relation shown in Figure 4.36. The phase profile and interpreted velocity profile are shown in Figure 4.43 a) and b), respectively. Making a comparison between the experimental and analytical results shows that the experimental velocity profile is

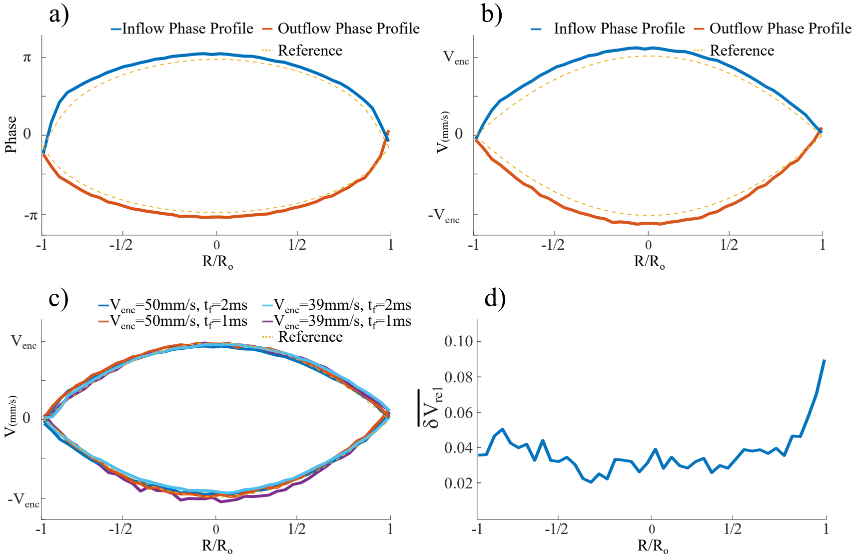

Figure 4.43: Phase map analysis of the MR image at the inlet and outlet of the sample holder with identical channels. a) The phase profile of the image for $V_{\text{enc}} = 50\,\text{mm}\,\text{s}^{-1}$ and $t_f = 2\,\text{ms}$. b) Velocity profile interpreted based on the relationship between phase and velocity shown in Figure 4.36. c) Velocity profile for four different settings of V_{enc} and t_f after applying the correction factor. d) Average relative error of the flow measurement based on the following equation, $\overline{\delta V}_{\text{rel}} = \left|\overline{V_i} - V_{\text{ref}}\right| / V_{\text{enc}}$ (Adapted from [57]).

1.15 times greater than the analytical one. This value is constant for all velocities, and the reason could be the response function of the electronics. So, this number is considered as a rescaling coefficient and is taken into consideration for the next measurements.

In the following, in order to check the generality of the pulse, the pulse is used for three distinct cases. In these experiments, the duration of the pulse for the first and the second one is 1 and for the third one is 2 ms, and corresponding V_{enc} is 50 for the first one and 39 $\text{mm}\,\text{s}^{-1}$ for the second and third one. The velocity profile of all cases is shown in Figure 4.43 c) and demonstrates a good accuracy for the present method. Also, the relative error in Figure 4.43 d) shows that for most voxels, the error fluctuates around 4 percent, except for some voxels close

to the wall. There can be two reasons for that. First, velocity reduction, which results in loss of signal (see Figure 4.37). The second issue could be the partial volume effect, which can still be the case despite applying a 3% signal mask.
In order to evaluate the validity of the present method for different geometries, the flow profile in another sample holder with a cylindrical inlet and annular outlet, shown in Figure 4.40 b), is obtained for four different cases. The V_{enc} of first and second case is $30\,\text{mm}\,\text{s}^{-1}$, and for the third and fourth one, it is $39\,\text{mm}\,\text{s}^{-1}$. The pulse duration of the first and third one is 2 ms, and that of the second and fourth one is 1 ms. The acquired image and corresponding phase map are illustrated in Figure 4.44.

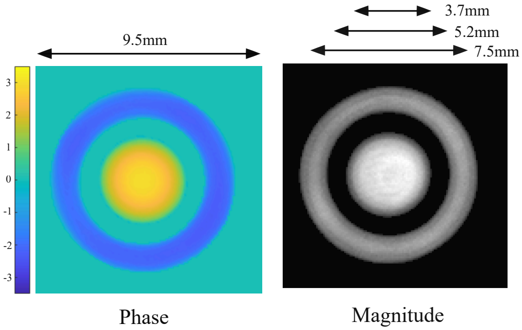

Figure 4.44: Phase and magnitude of the image taken by the OC pulse shown in Figure 4.38 at $V_{\text{enc}} = 30\,\text{mm}\,\text{s}^{-1}$. The sample holder is shown in Figure 4.40 b). The inner channel is the inlet, and the outer one is the outlet (Adapted from [57]).

The velocity profile is derived based on the relationship between phase and velocity shown in Figure 4.36, and it is demonstrated in Figure 4.45. The relative error, plotted in Figure 4.46, shows an increase in the error for voxels close to the walls, which can be due to the same issues mentioned for the first sample holder (reduction in velocity and partial volume effect).
Here, it is explained how the same excitation pulse can be employed for any value of V_{enc}. As mentioned before, the OC flow encoding RF pulse is designed for a certain value of Δ_{enc} which is equal to 3.2 in this study. It means, using

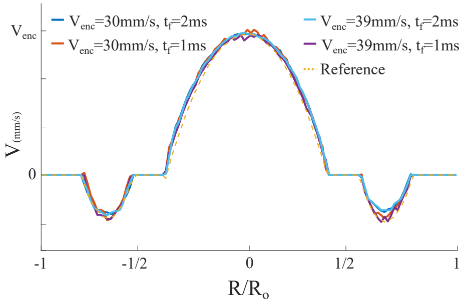

Figure 4.45: Velocity profile obtained from the results presented in Figure 4.44 (Adapted from [57]).

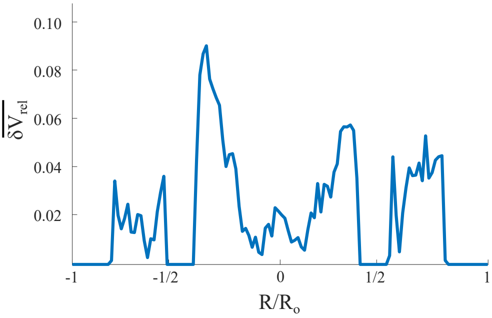

Figure 4.46: Average relative errors of flow measurement obtained from the results presented in Figure 4.45. The error is calculated based on the following equation, $\overline{\delta V_{\text{rel}}} = \left|\overline{V_i} - V_{\text{ref}}\right| / V_{\text{enc}}$ (Adapted from [57]).

the same excitation pulse with the duration of t_f, the OC gradient should be adjusted such that the fastest voxel (whose velocity is equal to V_{enc}) goes through a certain range of frequencies ranging from zero to $3.2/t_f$ Hz. As a numerical example, the first experiment, whose result is shown in Figure 4.43 c), is explained here in more detail. V_{enc} is $50\,\text{mm}\,\text{s}^{-1}$, and pulse length is 2 ms. So, the fastest voxel moves 0.1 mm during the excitation. On the other hand, it should experience $3.2/2\,\text{ms} = 1.6$ kHz. So, the gradient must be 1.6 kHz / 0.1 mm or $16\,\text{kHz}\,\text{mm}^{-1}$. The same calculation results in $64\,\text{kHz}\,\text{mm}^{-1}$ for the same V_{enc} and the pulse duration of 1 ms. For the third and fourth experimental cases in Figure 4.43, in which $V_{\text{enc}} = 39\,\text{mm}\,\text{s}^{-1}$ and $t_f = 2$ and $1\,\text{mm}\,\text{s}^{-1}$, the applied gradients are $20.5\,\text{kHz}\,\text{mm}^{-1}$ and $82\,\text{kHz}\,\text{mm}^{-1}$.

The next point is the slice thickness. The slice selectivity is achieved by limiting the bandwidth of the OC pulse. In this study, it is limited to the maximum frequency experienced by the fastest voxel. For a pulse with the duration of 2 ms, it is limited to $\pm 1600\,\text{Hz}$ when $V_{\text{enc}} = 50\,\text{mm}\,\text{s}^{-1}$. So, it results in the thickness of 0.1 mm. The thickness for the second to fourth experimental cases would be 0.05 mm, 0.078 mm, and 0.039 mm, in which the excitation times are 1, 2, and 2 ms, and V_{enc} values are 50, 39, and $39\,\text{mm}\,\text{s}^{-1}$ respectively. As Figure 4.43 c) implies, the last case with the thickness of 0.039 mm has less accuracy compared to the other ones.

4.5 Conclusion

Conventionally, in flow MRI, a bipolar gradient gradient is applied after a slice selective excitation pulse to encode velocity into the phase of the MR signal. Then, spatial encoding is performed to provide the MR image. As a result, the phase of each voxel in the MR image will be used as an indicator of its velocity, and hence, the phase map represents the velocity map of the sample. In this research, excitation and flow encoding steps are accomplished simultaneously by designing an RF pulse, which is not only slice selective but also able to perform the job of bipolar gradient (flow encoding).

The OCP is divided into two steps. The first step focuses on exciting and encoding the central plane of the slice placed at the isocenter of the gradient at $t = 0$. In addition, a constraint is added to the OCP to confine the bandwidth of the pulse so as to make it slice selective. The simulation results show that the pulse is capable of performing the flow encoding (Figure 4.21). Then, the performance of the pulse on the rest of the sample, and not only the central plane, is evaluated. The results presented in Figure 4.25 show that there is a linear change in phase along the slice direction. The net-phase from the whole thickness of the sample (corresponding to each velocity) is shown in

Figure 4.26. Although there is phase deviation in off-center planes compared to the central one, the OC pulse injects a bijective relationship between the velocity and phase of the MR signal. The magnitude of the MR signal is also calculated and shown in Figure 4.27, which shows a reduction in SNR for stationary and slow-moving voxels. The experimental evaluations show that due to SNR reduction, the method is not consistent (Figure 4.29). Therefore, the second step of OCP was initiated, in which the target is to minimize the phase non-uniformity shown in Figure 4.25. To do so, the whole volume is divided into 51 sub-slices, 25 of which are upstream and 25 downstream of the central slice, and a new TS is defined, in which there is much less phase dispersion. The difference between the current TS and the last phase dispersion is defined as the cost function. Despite the fact that, even after the second step, there is still phase dispersion left, and the TS is not completely achieved, the SNR enhancement is considerable, see Figure 4.37. Finally, experimental results show the feasibility and consistency of the present method for a number of experimental cases.

In this section, a comparison is made between the present and the conventional flow MRI method, namely phase contrast flow MRI based on the application of bipolar gradient. One of the most important parameters in flow MRI is time efficiency, more specifically, TE. In the design of OC pulse, it was mentioned that Δ_{enc} plays a major role. Based on Equation 4.23, it defines the encoding time (t_f), which contributes to the TE. A comparison between the delay caused by the conventional method, called phase contrast, and that of the current method is made in the following.

The encoding time or the delay caused in TE by the phase contrast flow encoding technique can be calculated by the following equation [22],

$$D_{\mathrm{PC}} = \sqrt{\frac{2}{\frac{\gamma}{2\pi} \cdot G \cdot V_{\mathrm{enc}}}}. \tag{4.26}$$

The delay that is caused in the TE by OC method flow encoding is half of the encoding (excitation) time. Based on Equation 4.23, the delay can be calculated by the following equation,

$$D_{\mathrm{OC}} = \frac{1}{2}\sqrt{\frac{\Delta_{\mathrm{enc}}}{\frac{\gamma}{2\pi}G \cdot V_{\mathrm{enc}}}}. \tag{4.27}$$

Replacing Δ_{enc} equal to 3.2 in Equation 4.27 and compare it with Equation 4.26 results in the following ratio between the delays,

$$R_D = \frac{D_{\mathrm{PC}}}{D_{\mathrm{OC}}} = 1.58, \tag{4.28}$$

where R_D is the ratio between two delays and is equal to 1.58. This means that in any pulse sequence in which flow encoding is longer compared to phase encoding, the OC flow encoding method is 1.58 times faster than the phase contrast technique.

The time efficiency of the methods is compared on an 11.74 T Bruker® with the imaging software ParaVision 360®. In this comparison, V_{enc} is $40\,\mathrm{mm\,s^{-1}}$, and the maximum gradient is limited to $61\,408\,\mathrm{Hz\,mm^{-1}}$. Based on Equation 4.27 and 4.26, the flow encoding delays for OC and PC methods are respectively 0.57 and 0.9 ms. Taking frequency encoding and rise time into account, the final echo time is 2.26 for the OC method. For the PC method, the time of excitation and refocusing gradient should be taken into account. Using a FLOWMAP pulse sequence, provided by Bruker® in ParaVision 360® imaging software, the minimum TE for such an experiment is 6.00 ms. A detailed comparison between the delays that take part in the TE of each method is presented in the following. The delays in the optimal control method are half of the excitation, phase encoding, half of the frequency encoding, and the rise time of gradients. The ones in the bipolar gradient method are half of the excitation, slice refocusing, flow compensation, flow encoding, half of the frequency encoding, and the rise time of gradients.

$$\mathrm{TE_{OC}} = \underbrace{1.1414}_{\text{Excitation}}/2 + \underbrace{0.12}_{\text{Phase Enc.}} + \underbrace{2.56}_{\text{Frq. Enc.}}/2 + \underbrace{0.29}_{\text{Rise time}} = 2.26\,\mathrm{ms}$$

$$\mathrm{TE_{BG}} = \underbrace{1.5}_{\text{Excitation}}/2 + \underbrace{0.75}_{\text{Slice Ref.}} + \underbrace{1.5}_{\text{Flow Comp.}} + \underbrace{0.9}_{\text{Flow Enc.}} + \underbrace{2.56}_{\text{Frq. Enc.}}/2 + \underbrace{0.82}_{\text{Rise time}} \Rightarrow$$

$$\mathrm{TE_{BG}} = 6.0\,\mathrm{ms}$$

The experimental results are shown in Figure 4.47 and demonstrate a good agreement between OC and PC methods.

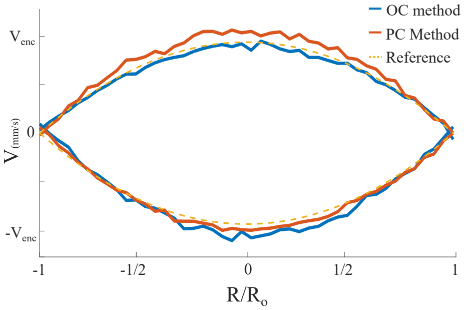

Figure 4.47: Comparison of velocity profiles measured by OC and PC methods at $V_{\mathrm{enc}} = 40\,\mathrm{mm\,s^{-1}}$.

Also, the relative error for both methods is calculated based on the deviation from a reference parabolic profile. The comparison shown in Figure 4.48 demonstrates a comparable accuracy for both methods.

In addition, as Figure 4.41 indicates, compared to the PC technique, the current technique demands less gradient switching, which decreases the adverse effects of eddy currents.

As Equation 4.27 indicates, the delay is in a direct relationship with the Δ_{enc}, which is equal to 3.2 in this study. Choosing a smaller value and redesigning the OC pulse can further enhance the time efficiency of the present method. In addition, based on Equation 4.23, it decreases the gradient needed for a specific t_f and V_{enc}. However, it would be challenging to avoid an over-constrained OCP

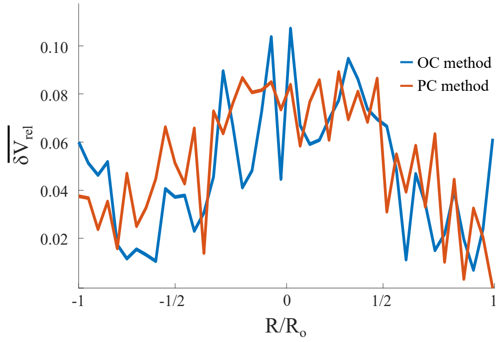

Figure 4.48: Comparison of average relative errors of OC and PC flow measurement at $V_{\text{enc}} = 40\,\text{mm}\,\text{s}^{-1}$.

for small values of Δ_{enc}. Establishing a bijective relationship between phase and velocity would be another challenge for small values of Δ_{enc}.

Another topic for further studies is to improve the phase non-uniformity in the slice direction. Despite the fact that the second step of the OCP significantly helped to enhance the uniformity, it is still not completely uniform; see Figure 4.35. Reducing this non-uniformity can enhance the SNR.

The design of the OC pulse in this study is based on FEM. This gives us a lot of freedom to customize the pulse depending on the case study demand. As shown in Figure 4.36, the relationship between phase and velocity is already nonlinear and not even symmetric. In fact, this feature can be employed to enhance phase-SNR for a certain velocity range. For example, if more resolution is needed for slow-moving voxels, the TS can be defined accordingly. This feature can help specific cases. For instance, in clinical applications, it can enhance the resolution of slow-moving voxels to detect blood behavior close to the walls.

Another potential application for OC is to design an RF pulse for any customized homemade gradient system. To use this method, one doesn't need a precisely linear and symmetric gradient. Instead, just the output shape is needed to put into the mathematical model of OCP and design the required RF pulse.

OC pulse can be designed in a highly targeted manner for a specific issue. One of the challenging case studies in flow MRI is turbulent flows. In such cases, higher-order terms (HOT) of the Taylor expansion come into play. The effect of these parameters can be taken into consideration, and an RF pulse can be designed to exclusively tackle their unfavorable effects. In the following, the effect of HOT of the Taylor expansion on the current OC method is evaluated. The Taylor expansion of displacement can be written as the following,

$$x(t) = x_0 + v_0 t + \frac{1}{2} a_0 t^2 + \frac{1}{6} j_0 t^3 + \frac{1}{24} s_0 t^4 + \cdots , \tag{4.29}$$

in which x_0 is displacement, v_0 is the velocity, a_0 is acceleration, j_0 is jerk, and s_0 is snap. The HOT are normally ignored, but they play a role in highly turbulent cases and can reduce the precision of measurement. An assessment is made to evaluate the effect of HOT terms, up to the fourth order, on the OC method, and it is compared with the phase contrast technique.

In order to evaluate the effect, the linear movement of the voxels is replaced by a random movement up to an order of four, and this simulation is repeated for 100 different random movements. To make a valid comparison with the previous results, the total displacement is the same. Also, in this assessment, the maximum deviation is limited to up to 10% of the total movement. The trajectory of one of the fourth-order displacements is shown in Figure 4.49.

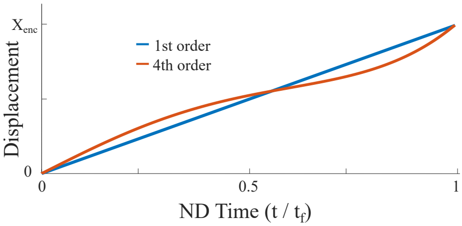

Figure 4.49: Displacement of a voxel with the 1st and 4th order of movement (Adapted from [57]).

Ideally, the phase response should be the same value as the previous results. But, as shown in Figure 4.50, HOT cause deviation from the ideal response.

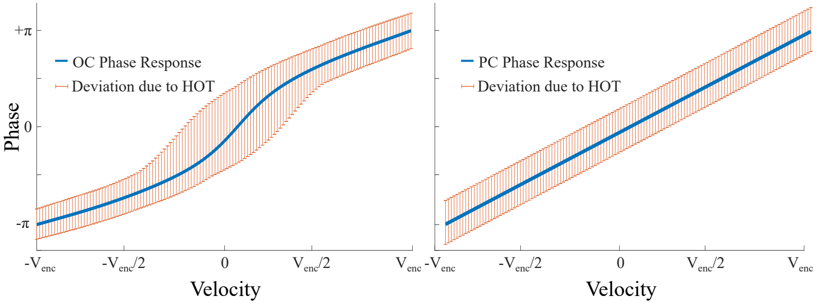

Figure 4.50: Deviation in phase response due to higher-order terms (HOT) of displacement. The deviation is lower in PC for slow-moving voxels, while, for fast-moving voxels, the OC method shows better robustness against HOT (Adapted from [57]).

The results in Figure 4.50 show phase deviation for 100 random movement trajectories. In Figure 4.51, the maximum phase deviations of both methods are compared together.

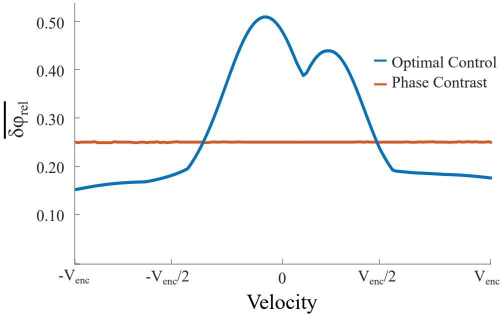

Figure 4.51: Maximum relative errors due to HOT of displacement, calculated based on the following equation, $\delta\phi_{\text{rel}} = |\phi_i - \phi_{\text{ref}}|/\pi$ (Adapted from [57]).

The results show that the OC method demonstrates better robustness against HOT for fast voxels. However, phase contrast seems to be more robust for slow voxels. In future studies, the same mathematical model, which includes different non-linear displacements, can be used in OCP to make the method more resilient even for slow voxels.

5 Application of selective excitation in MRV

This chapter consists of two main sections, which are about the application of selective excitation in diffusion and flow measurement. My contribution to the first one was to optimize the parameters and perform some of the experiments in cooperation with Dr. Neil MacKinnon [61]. For the second section, I designed the flow channel, wrote the pulse sequences, performed the measurements, and post-processed the data. The concept of the bipolar selective flow encoding (BSFE) pulse sequence (Figure 5.16) is from me, and the idea of unipolar selective flow encoding (USFE) sequence is from Dr. Lehmkohl (Figure 5.15).

Selective excitation pulses can be divided into two main categories: spatial and spectral selective pulses. Spatial selective RF pulses are coupled with a gradient and have many applications. The most widely used one is slice selection in MRI. Another application of spatially selective pulses is Ramp, or *tilted optimized non-saturating excitation* (TONE) pulses, shown in Figure 5.1.

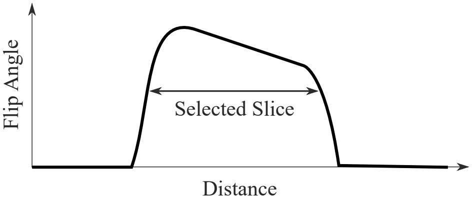

Figure 5.1: Exemplar of a TONE excitation pulse. It shows the tilted excitation profile over the imaging slice.

TONE pulses have an uneven excitation profile to compensate for the non-uniform condition over the slice and are designed to homogenize the signal from the excitation region [22]. For example, they are applicable in the 3D-TOF method to counteract the adverse effect of flow on the uniformity of the excited slice. Spatial selective pulses can also be used to saturate an unwanted slice. For instance, to remove the undesirable effect of inflow to the imaging slice. The spectral selective pulses have many applications as well. They can be used to suppress the signal of a certain chemical group, i.e. water. It helps to detect the signal coming from small metabolites, which are difficult to discover in the presence of water signals. In addition, selective excitation can help us to excite just a specific chemical species with a certain chemical shift. It provides us with an image of the species i.e. fat. The utilization of selective excitation is further enhanced in this study. Instead of performing just one measurement in each experiment, it tried to run a different measurement on each chemical group in each experiment. This invention is applied to two MR applications, including diffusion and flow NMR.

5.1 Application of selective excitation on diffusion NMR

By definition, diffusion is the movement of molecules from an area of higher concentration (Region A in Figure 5.2) to an area of lower concentration (Region B in Figure 5.2) without any external forces [62].

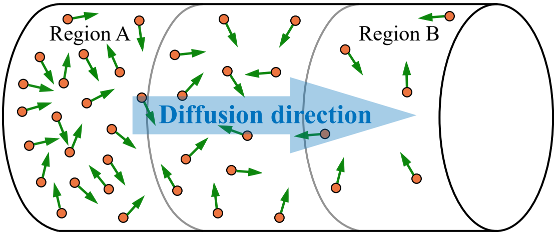

Figure 5.2: Illustration of the diffusion process.

MR diffusion measurement gained popularity due to beneficial applications such as fiber tracking and brain stroke evaluation [63]. NMR has demonstrated precise diffusion measurement capability. However, there are some limitations, particularly in the case of chemical mixtures. Pulse sequence parameters, including gradient time and power, have to be optimized exclusively for each chemical group. In the presence of a number of groups with different diffusion coefficients, parameter optimization would be challenging. In the current study, selective excitation is employed as a remedy.

5.1.1 Diffusion measurement by NMR

As shown in Figure 5.3, by applying a motion-sensitizing gradient, movement leads to phase injection. The movement of molecules due to diffusion is a random process. So, it results in a random phase injection, which leads to signal attenuation. The greater the value of the diffusion coefficient, the more the displacement and, hence, the more signal attenuation. This feature is employed to calculate the diffusion coefficient by NMR experiments. Excluding T_1 relaxation, the signal magnitude in an echo attenuates due to three mechanisms T_2 relaxation, molecular diffusion, and B_0 inhomogeneity. While T_2 is an intrinsic property of the nuclei, applying a refocusing RF pulse reduces the effect of the inhomogeneity. The *pulsed gradient spin echo (PGSE)* technique was first developed by Edward Stejskal and John Tanner [64] to measure the diffusion coefficient of the sample, and upon which modern diffusion-weighted (DW) sequences are designed. PGSE consists of a pair of symmetric motion-sensitizing gradients, which are separated by a 180°-pulse (Figure 5.3).

PGSE makes a direct relationship between signal intensity and the diffusion coefficient of the solvent. The relationship between the normalized signal and diffusion coefficient is as follows,

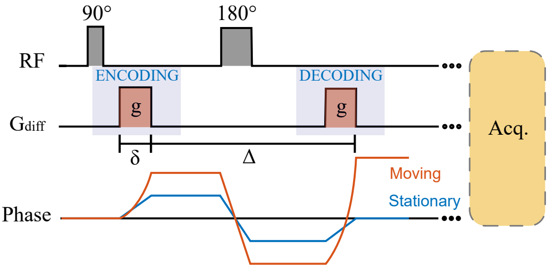

Figure 5.3: Schematic representation of a PGSE motion-sensitizing gradients.

$$\begin{aligned} I &= \exp\left(-\gamma^2 G^2 \delta^2 D \left(\Delta - \frac{\delta}{3}\right)\right) = \exp\left(-kD\right), \\ \text{where, } k &= \gamma^2 G^2 \delta^2 \left(\Delta - \frac{\delta}{3}\right), \end{aligned} \tag{5.1}$$

where I is the normalized NMR signal intensity, γ is the gyromagnetic ratio, δ is the diffusion gradient pulse length, D is the diffusion coefficient, Δ is the diffusion time, G is the applied gradient strength, and k is the diffusion experiment parameter. Equation 5.1 indicates that, for a certain value of D, if we perform several experiments over which the value of k increases, the signal density I decreases. A schematic representation of the intensity versus the value of k is shown in Figure 5.4.

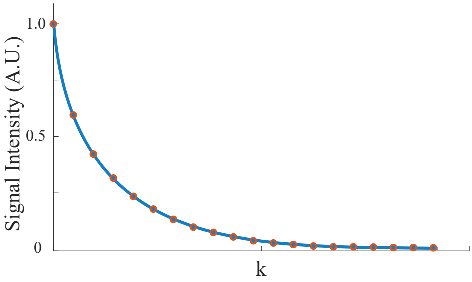

Figure 5.4: Exemplar of signal intensity versus the value of k (Equation 5.1). The intensity attenuates due to diffusion.

As shown, the intensity attenuates as the gradient increases. By repeating the experiment for different values of k, the curve of signal intensity versus k can be plotted. Consequently, knowing I and k and based on Equation 5.1, the diffusion coefficient D can be extracted using a fit function.

Diffusion encoding can be performed by application of PGSE pulse sequence. However, the problem is that during the time delay between two gradients (Δ), magnetization is situated at xy-plane, which means that the signal will be attenuated not only by diffusion but also by spin-spin coupling or T_2 relaxation. To tackle this issue, the *pulsed-field gradient stimulated echo* (PFG-STE) is designed in which 180°-pulse is replaced by two 90°-pulses. As a result, magnetization would be along the z direction during the time delay Δ. The pulse sequence is shown in Figure 5.5.

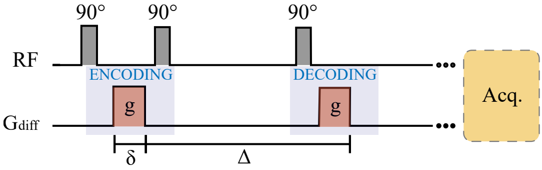

Figure 5.5: Schematic representation of a PFG-STE motion-sensitizing gradients.

The issue of PFG-STE is that the encoding and decoding gradients are applied in the same direction, which leads to the collective effect of eddy current. To tackle the issue, the next version of the diffusion pulse sequence is modified, called *bipolar pulse longitudinal eddy-current delay* (BPP-LED) [65]; see Figure 5.6. In this pulse sequence, diffusion-encoding gradients are applied equally in opposite directions. Consequently, the effects of eddy current due to encoding and decoding gradients cancel each other. In the current study, this version is further modified and used to perform diffusion measurements.

5.1.2 Selective excitation diffusion measurement

In the present research, a selective version of the BPP-LED sequence, shown in Figure 5.7, is used. The goal of this sequence is to have a selective diffusion

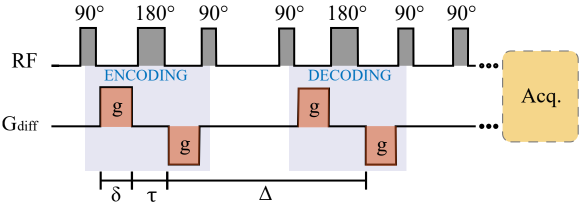

Figure 5.6: Schematic representation of a BPP-LED motion-sensitizing gradient.

measurement for three different spin isochromats with the Larmor frequencies of ν_1, ν_2, and ν_3. The pulse sequence consists of two main blocks, which precede a hard 90°-pulse. The first block performs encoding, and the second one accomplishes decoding. Each block has three steps to perform the encoding/decoding for each of the three isochromats. Each step starts with a selective 90°-RF pulse to excite the corresponding spin isochromat. Then, the next two gradients and the selective 180°-pulse accomplish diffusion encoding/decoding. At the end of this step, another selective 90°-pulse stores the magnetization along the z-axis. It keeps the magnetization untouched when the next encoding/decoding gradients are applied to the next isochromat. In the second and third steps, the same task is implemented for the second and third isochromats. Each step ends with a spoiler gradient to remove any residual signal due to any nonideality. Also, there is a certain delay between the two blocks. After the second block, all isochromats are stored in the z-direction. In the end, a hard 90°-pulse excites the whole sample.

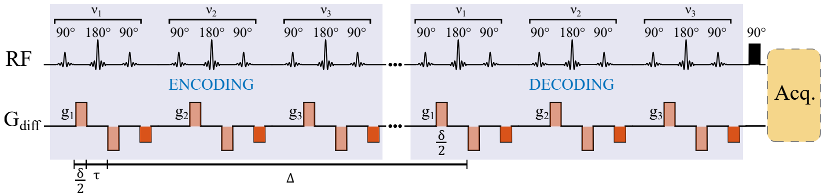

Figure 5.7: Schematic representation of a Sel-BPP-LED (selective-BPP-LED) diffusion pulse sequence [61].

By applying the selective version of the BPP-LED sequence (Sel-BPP-LED), all isochromats go through diffusion measurement in a selective manner. It lets us use individual parameters for each isochromat. For instance, the power of the diffusion gradient can vary for each one.

Using the pulse sequence shown in Figure 5.7, Equation 5.1 has to be replaced by the following equation [66],

$$\begin{aligned} &I = \exp\left(-\gamma^2 G^2 \delta^2 D\left(\Delta - \frac{\delta}{3} - \frac{\tau}{2}\right)\right) = \exp\left(-kD\right), \\ &\text{where, } k = \gamma^2 G^2 \delta^2 \left(\Delta - \frac{\delta}{3} - \frac{\tau}{2}\right). \end{aligned} \tag{5.2}$$

5.1.3 Materials and methods

The sample consists of 10 mg of tripeptide Met-Ala-Ser (MAS) dissolved in 0.5 mL of 10:90 H_2O:D_2O. The targeted chemical groups to perform selective excitation diffusion measurements are the water signal at 4.8 ppm, the signal from methionine methyl at 2.1 ppm, and that of alanine methyl at 1.45 ppm.

All measurements are conducted on an 11.74 T Bruker® spectrometer equipped with a Micro5 micro-imaging probe, a three-axis imaging gradient, and a 5 mm insert. In TopSpin 3.6.3 software, the parameter optimization (popt) function is used to sweep the gradient power, and the Shape Tool is employed to calculate the length and power of the excitation pulses. A smoothed square (SMSQ10.100) shape is used for diffusion encoding gradients, which leads to a small deviation from an ideal sharp square shape. To take this deviation into account, a calibration experiment is performed, in which the diffusion coefficient of water is considered equal to $2.02 \times 10^{-9}\,\mathrm{m}^2\,\mathrm{s}^{-1}$[67] and the corresponding value of the gradient power is calculated as if the shape was a sharp square. Based on this evaluation, the maximum gradient of the system can be considered $110.7\,\mathrm{kHz\,mm}^{-1}$ (instead of the original value $122.816\,\mathrm{kHz\,mm}^{-1}$). The gradient is linearly sweeping from 1 to either 60 or 95% of the maximum power, and, in order to have enough data points in the diffusion curve, the experiments are performed for 16 different values within this range. The acquisition time is 1.6 s and detection bandwidth is 10 kHz. Also, zero-filling is performed by a factor of 2, and the exponential multiplication technique by a linebroadening factor of 0.3 Hz is used to improve SNR. All experiments are repeated three times to calculate the corresponding standard deviation.

Three sets of experiments are performed. First, the non-selective BPP-LED pulse sequence, shown in Figure 5.6, is used to perform diffusion measurement experiments, in which $\delta = 2\,\mathrm{ms}$, $\Delta = 250\,\mathrm{ms}$, number of sampling (ns)=8, and gradient power increases from 1 to 95%. Second, the Sel-BPP-LED pulse sequence, presented in Figure 5.7, is used to perform the same experiments but in a selective manner. The measurement parameters are the same. But, the hard pulses are replaced by selective ones. For 90°-pulses, a sinc-based excitation pulse (Sinc1.1000) with the duration of 26.8 ms, resulting in 60 Hz of bandwidth, is used, and for the 180°-ones, a Gaussian pulse with the length of 14.7 ms, corresponding to the bandwidth of 144 Hz, is employed (Gaus1_180r.1000). The last set of experiments is the same with the second one, except the diffusion gradient for water. The selective excitation technique lets us apply diffusion gradients with different values of power on each signal. On the MAS, the same gradient is applied (1 to 95%), but on the water, the gradient increases from 1 to 60%.

5.1.4 Results and discussion

The results of three sets of experiments are presented in Figure 5.8. Signal intensity versus the value of k, presented in Equation 5.2, is plotted in Figure 5.9. It illustrates a comparison between the first and second sets of experiments, which are non-selective and selective, respectively. In both, the gradient amplitude increases from 1 to 95%. As shown, the results present good agreement between them.

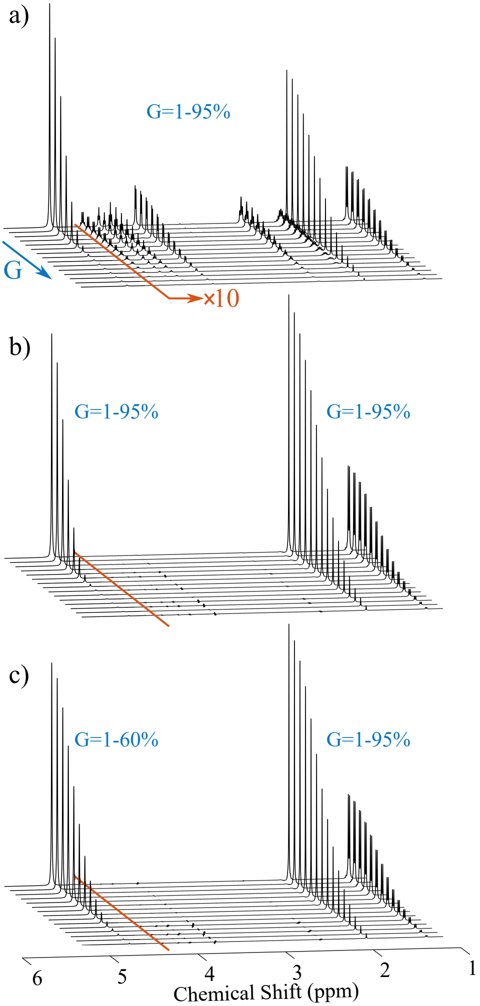

Figure 5.8: Experimental results of three sets of NMR diffusion measurements. The first set of experiments (a) is performed using the non-selective BPP-LED pulse sequence (Figure 5.6). The second one (b) is based on the selective version, called Sel-BPP-LED (Figure 5.7), in which the same range of diffusion gradients are used for three individual signals (H_2O, methionine methyl, and alanine methyl) but in a selective manner. The last one (c) is also based on the selective version, however, in which the diffusion gradient varies from 1 to 95% for methionine methyl and alanine methyl, yet from 1 to 60% for water.

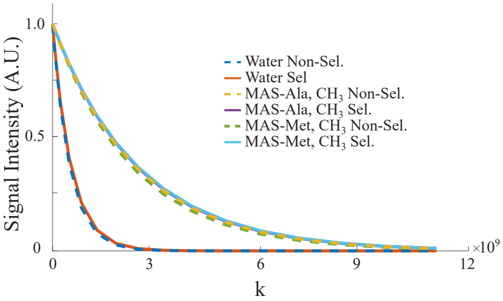

Figure 5.9: Signal intensity in dependence of the value of k (defined in Equation 5.2). The power of diffusion gradient increases from 1 to 95% in all experiments. The solid lines represent the selective experiments, and the dashed lines show the results of the non-selective experiments.

Figure 5.10 compares the results of the second and third sets of experiments, which are both selective, but in the first one, the gradient of H_2O increases from 1 to 95%, and in the second one, it increases from 1 to 60%. In both of them, the diffusion encoding gradient sweeps from 1 to 95% for Met and Ala.

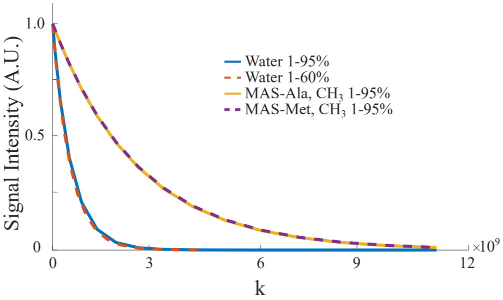

Figure 5.10: Signal intensity in dependence of the value of k (defined in Equation 5.2). All experiments are carried out in a selective manner. The solid lines show the results of the experiments in which the amplitude of diffusion gradient of H_2O, Met, and Ala increases from 1-95%. In the experiments shown by dashed lines, the gradient of Met and Ala increases from 1 to 95% while that of H_2O sweeps from 1 to 60%.

Figure 5.10 shows the feasibility of selectively encoding the diffusion of different signals with an exclusive setting of the gradients for each signal. In this

Chemical group	SNR $\left(\times 10^3\right)$	D $\left(\times 10^{-10} m^2\, s^{-1}\right)$	Selectivity
Water	2700 ± 700	20.0 ± 0.6	×
	1800 ± 130	19.3 ± 0.07	✓
Methionine	100 ± 30	4.33 ± 0.03	×
	102 ± 8	4.17 ± 0.01	✓
Alanine	90 ± 20	4.14 ± 0.02	×
	86 ± 6	4.20 ± 0.01	✓

Table 5.1: Numerical results including SNR, diffusion coefficient (D), and corresponding standard deviation obtained from the first and third sets of experiments, which are non-selective and selective, respectively. In the first set, the gradient is the same for all components (1 to 95%). But, in the third one, the gradient power increases from 1 to 95% for methionine and alanine, yet from 1 to 60% for H_2O.

figure, it is shown that, in the same experiment, the power of diffusion encoding gradient of H_2O can be different from that of Met and Ala.

The results shown in Figure 5.9 and 5.10 are further analyzed, and the diffusion coefficients are obtained using a fit function by MATLAB. The numerical results of the first and third sets of experiments are compared in Table 5.1. It shows that when the experiment is performed in a selective way, there is a 33% reduction in the SNR of H_2O signal. However, the change in that of MAS is negligible (-4 and +2% for Met and Ala, respectively). The cause could be the delay between H_2O diffusion encoding and the readout since H_2O is the first encoded chemical group. The SNR reduction can be due to any imperfection in the selectivity of the pulses as well. Making a comparison between selective and non-selective diffusion measurements shows that the results are in good agreement. The resultant diffusion coefficients from the non-selective experiments are 20.0×10^{-10}, 4.33×10^{-10}, and $4.14 \times 10^{-10}\ \mathrm{m^2\,s^{-1}}$ for H_2O, Met, and Ala respectively. The coefficients calculated from the selective ones are 19.3×10^{-10}, 4.17×10^{-10}, and $4.20 \times 10^{-10}\ \mathrm{m^2\,s^{-1}}$, which shows 3.3, 3.9, and -1.5% deviation. The cause can also be any imperfection in the selectivity.

The diffusion coefficient is calculated by the results of the second set of experiments as well, which gives us D=19.2×10^{-10}, 4.16×10^{-10}, and $4.20 \times 10^{-10}\,\mathrm{m^2\,s^{-1}}$ for H_2O, Met, and Ala.

5.1.5 Conclusion

This study shows the feasibility of taking advantage of selective excitation to selectively encode diffusion coefficients in the magnitude of the MR signal. This invention enables us to use exclusive encoding settings for each signal. Figure 5.10 shows that, using the mentioned delays $(\Delta, \delta, \text{and}\,\tau)$, increasing gradient power from 1 to 60% is enough to achieve a complete decay in H_2O signal, while, for Met and Ala, it is needed to increase it to 95%. In fact, selectivity gives us a better degree of freedom to encode more parameters in the same experiment. In this study, the degree of freedom is three. The degree can increase as long as the length of selective pulses doesn't result in T_1 relaxation. In this research, selectivity was employed to perform parallel diffusion measurements on different signals. However, this idea can be further generalized to the other MR fields. From a broader perspective, in MR, the properties of the sample are encoded in the phase or magnitude of the signal. These properties can include density, diffusion, temperature, or velocity. There are specific pulse sequences to measure these characteristics. The key point of the current chapter is that when there are more than one signal in the sample, selective pulses enable us to perform customized pulse sequence for each signal in the same measurement. Each sequence can be optimized depending on the desired outcome and signal condition. For instance, in diffusion measurement, a chemical group might need a stronger gradient to reach a complete decay. This invention can be used in other fields. In the next section, the application of selective excitation is discussed in MR flow measurement.

5.2 Application of selective excitation on MR flow measurement

MR flow measurement is a unique experimental method to evaluate flow behavior in industrial and clinical applications. Three main characteristics make this method exceptional. First, it is a non-invasive method, which means that there is no need to have access to the inner side of the sample. It contrasts with some other experimental approaches, i.e., *hot-wire anemometer* (HWA), in which it is needed to put a probe exposed to the flow. This is not a favorable characteristic since it not only limits the feasibility but also can disturb the flow behavior. Second, in this method, there is no necessity to add tracing particles. *Particle image velocimetry* (PIV) is an experimental method to measure the flow behavior, however, in which entrained particles are needed to do the experiment. It limits the method's applicability in clinical applications and decreases the robustness since there might be differences between particles and liquid streamlines. The last superiority of MR flow measurement is that there is no requirement to have optical access, which is not offered by some other experimental methods, including *laser Doppler anemometry* (LDA). In MR, the measurement signal is a magnetic signal received directly from the nuclei, and it is collected by a coil placed outside the sample.

5.2.1 NMR flow encoding

MR flow measurement can be divided into two main categories, in which velocity is encoded in the magnitude and phase of the signal, respectively. Although it is easy to implement, the former suffers from losing SNR either for the fast or slow range of velocities. The latter, called phase contrast (PC) flow MRI, keeps the SNR high for a broader velocity range and is more favorable. The principles of the PC method are similar to diffusion measurement and based on the application of motion-sensitizing gradient; see Figure 5.3. As shown in the figure, having applied the motion-sensitizing gradient, a movement-dependent phase is injected into the MR signal. The following equation calculates the injected phase due to motion [22],

$$\phi = \int_0^{t_f} \gamma\, g(t)\, r(t)\, dt \approx -\gamma\, g\, \Delta\, \delta\, v = k_{\text{enc}}\, v, \quad k_{\text{enc}} = -\gamma\, g\, \Delta\, \delta, \tag{5.3}$$

where ϕ is the injected phase, γ is the gyromagnetic ratio, g is the applied gradient strength, Δ is the encoding time, δ is the gradient pulse length, and k_{enc} is the flow experiment parameter.

The phase is always limited between $-\pi$ and π. So, the maximum velocity in the flow system should be correlated to π. We should make sure that there is no velocity beyond this limit. Based on this fact, a very important parameter is defined in PC flow measurement, called V_{enc}, which is the maximum velocity to encounter in the flow system. The motion-sensitizing gradient should be designed such that:

$$V_{\text{enc}} = \frac{\pi}{k_{\text{enc}}}. \tag{5.4}$$

The value of V_{enc} has to be defined first. Then, based on Equation 5.4, the required k_{enc} can be calculated. Then, based on Equation 5.3, the value of g, Δ, and δ can be obtained.

There should be no velocity larger than V_{enc} in the system. Otherwise, it leads to *aliasing*. Any phase greater than π, or smaller than $-\pi$ can't be recognized correctly by the system and will be shifted by multiples of 2π. For example, assume $V_{\text{enc}} = 12\,\text{mm}\,\text{s}^{-1}$. The resultant phase of a voxel with the velocity of $V_{\text{i}} = 14\,\text{mm}\,\text{s}^{-1}$ is $7\pi/6$. But, by a 2π offset, it will be recognized as $\phi = -5\pi/6$ and results in $V_{\text{i}} = -10\,\text{mm}\,\text{s}^{-1}$. This issue is called wrapping as well.

On the contrary, the value of V_{enc} should not be chosen far bigger than the maximum velocity since it increases the standard deviation [12].

$$\text{StdDev} = \frac{\sqrt{2}}{\pi} \cdot \frac{V_{\text{enc}}}{\text{SNR}} \tag{5.5}$$

In the case of big values of V_{enc}, the injected phase would be very low, reducing the phase-SNR and phase resolution versus velocity. In fact, changes in phase due to velocity would be dominated by noise. Depending on the hardware, experimental condition, pulse sequence, and measurement parameters, any spectrometer gives us a specific resolution over the range of $-\pi$ to π. In other words, it gives us a specific resolution to differentiate voxels with a particular velocity offset.

Briefly, a smaller value of V_{enc} is preferred as long as it doesn't lead to aliasing. There are some techniques to unwrap the velocity map. But none of them is entirely reliable, especially when velocity fluctuation in the adjacent voxels is considerable.

5.2.2 Selective excitation flow NMR

Choosing V_{enc} is always challenging in MR flow measurement. Small values have the risk of aliasing, and big values decrease the measurement resolution. In the current chapter, selective excitation is used as a remedy to tackle this issue. In the presence of two chemical groups with nonidentical chemical shifts, a different value of V_{enc} can be chosen for each one. This technique can exceptionally enhance the accuracy of PC flow measurements. While the small value of V_{enc} can provide us with a very high phase-SNR and phase resolution versus velocity, the big one can be used to unwrap the phase map of the small one and avoid aliasing. This scheme resembles a clockwork of a watch. The chemical groups play the role of the hands. In a watch with just one hand, the minimum resolution is 1 s, and the V_{enc} is 60 s. Adding the second hand keeps the resolution still the same but extends the V_{enc} to 3600 s. Adding the third one increases it to 43 200 s. In fact, the second hand is used to unwrap the first one, and the third one is employed to unwrap the second. Using three spectral regions, the same technique could be applied to a flow system. In a PC flow measurement system, whose resolution and initial V_{enc} are 1 and 60 $\mathrm{mm\,s^{-1}}$, the V_{enc} could be extended to 43 200 $\mathrm{mm\,s^{-1}}$ while the resolution is still the same.

Based on Equation 5.5, the standard deviation remains the same while the V_{enc} is increased by a factor of 720.

5.2.3 Materials and methods

Having shown the tremendous advantage of the present invention in MR flow measurement, the feasibility is evaluated in the following. The idea is to prepare a sample containing two chemical species with different values of chemical shift. Then, a sample holder is designed and 3D printed to deliver a steady-state laminar flow. Finally, two selective pulse sequences are composed to measure the flow rate by defining a specific V_{enc} for each chemical. As a result, although the chemicals have the same flow rate, they inject different phases as the flow rate increases. Then, the phase value of the one with bigger V_{enc} is used to unwrap the phase of the other one. The sample provided for the experiment contains 2M of sodium acetate (NaOAc) dissolved in 23:77 H_2O:D_2O. Also, to provide a non-pulsatile stable flow rate, a syringe pump is used.

3D-printed sample holder

The sample holder is 3D-printed by rapidobject® company by the resin *Medizinisch MED-AMB*. It shows excellent compatibility with NMR measurements. Regarding the sample holder, there are two critical points: first, inertness, and second, background signal.

In Figure 5.11, a comparison is made between two sample holders. The first one is 3D-printed by *Phrozen Aqua Resin Ivory 4K* and the second one by *Medizinisch MED-AMB* resin. As shown in the figure, the second resin has almost no background signal.

In addition, doing some experiments in a one-day time span shows the reactiveness of the *Phrozen Aqua Resin Ivory 4K* against the sample; see Figure 5.12. No changes were noticed during performing the experiments with the sample printed with the *Medizinisch MED-AMB* resin.

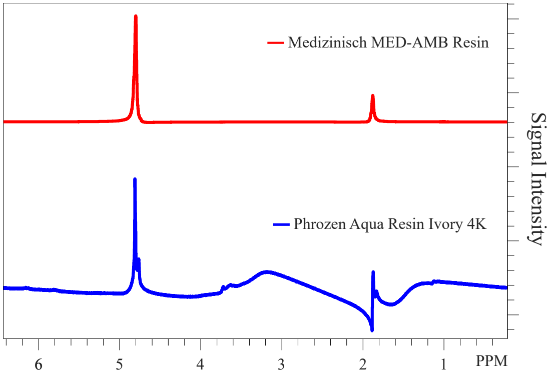

Figure 5.11: Comparison between the background signal of the sample holders 3D-printed by the *Phrozen Aqua Resin Ivory 4K* and *Medizinisch MED-AMB* resin.

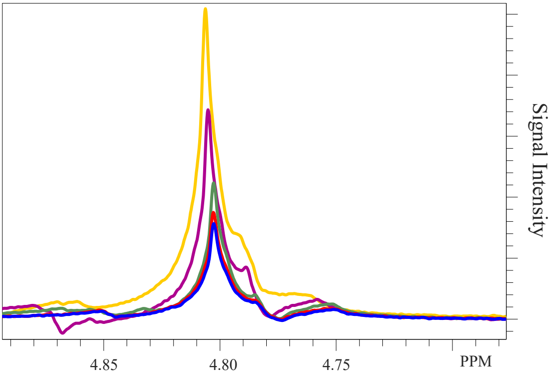

Figure 5.12: Water peak of the sample holder 3D-printed by *Phrozen Aqua Resin Ivory 4K* containing D_2O, H_2O, and NaOAc. It shows that the water signal increases over time, which is because of the reactiveness of the resin against the sample.

Recently, 3D printers have been massively used to produce complicated designs to perform different types of experiments. Also, different types of materials, including resins and filaments, are available. These results show the necessity of more evaluations regarding the compatibility of different materials for 3D-

printing NMR sample holders. The material can be assessed for background signal, inertness against different chemicals, susceptibility mismatch, etc.
The next step is to find the geometry of the sample holder. The experiments are carried out in an 11.74 T Bruker® spectrometer, using a Micro5 micro-imaging probe, a three-axis imaging gradient, and a 10 mm insert. Since the probe is a close-end one, the inlet and outlet of the sample have to be on the same side. So, the signal of both inlet and outlet would be collected by the spectrometer. They inject phases the opposite of each other. To have a non-zero net phase, different cross-sections are considered for the inlet and outlet since the cross-section of the channel strongly impacts its phase response [29]. Also, due to the inner diameter of the insert (10 mm), the outer diameter of the sample holder is limited to 9.7 mm. A schematic representation of the sample holder is shown in Figure 5.13. The size of the rectangular channel is 2 × 7 mm, and the diameter of the cylindrical channel is 1.3 mm. The total length of the channel is 18 mm to let the flow profile fully develop.

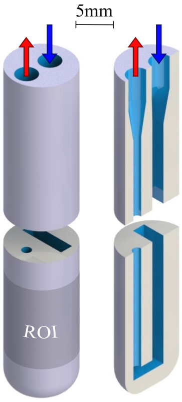

Figure 5.13: Graphical representation of the sample holder. It has a rectangular inlet and a cylindrical outlet. The region of interest (ROI) is shown in the figure.

The net MR response of the flow in the sample holder is evaluated by simulating the magnetization evolution of the MR signal from each channel and illustrated in Figure 5.14. The flow in channels moves in opposite directions. As a result, to some extent, they cancel each other. The cylindrical channel injects more phase than the rectangular one. Still, since its signal attenuates much faster, the net phase would be controlled by the signal emitted from the rectangular one. This simulation is performed based on the assumption of having a uniform flow profile along the longer side of the channel, which means that the drop in the velocity field close to the lateral walls is neglected. Since the ratio between the width and length of the rectangular cross-section is not very small (2 over 7 mm), a small deviation from this simulation is expected. In addition, some other parameters, including the exact shape of the applied gradient (which is not necessarily the same as a rectangle shape) and imperfections in 3D-printing the sample, can cause deviation from this simulation. So, even though this simulation gives us a good conception of the phase response, a benchmark measurement will be performed to have a reliable evaluation of the precision of the proposed pulse sequences.

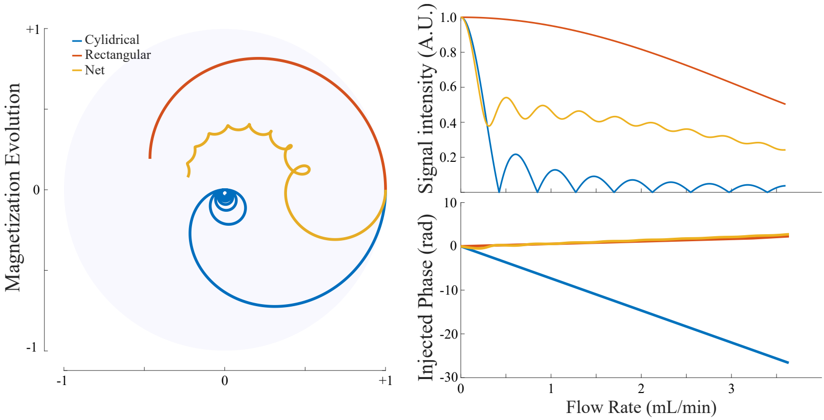

Figure 5.14: Magnetization evolution, signal intensity, and phase response of the MR signal emitted from a sample with a rectangular inlet (2 × 7 mm) and a cylindrical outlet (D=1.3 mm).

Flow encoding pulse sequence

All of the motion-sensitizing pulse sequences presented in this chapter, including *pulsed gradient spin echo* (PGSE), *pulsed-field gradient stimulated echo* (PFG-STE), and *bipolar pulse longitudinal eddy-current delay* (BPP-LED), as well as the bipolar gradient pulse sequence (Figure 2.23) can be employed to establish a linear relationship between MR phase and flow rate.
In the current section, two pulse sequences are presented to establish selective excitation flow encoding with a specific value of V_{enc} for each chemical group.

1. **Unipolar selective flow encoding (USFE) pulse sequence**: The first sequence is based on the application of unipolar flow encoding gradient and refocusing RF pulses. It is a hybrid of PFG-STE and PGSE that applies the former on the first signal and the latter on the second signal. A schematic representation of the pulse sequence is presented in Figure 5.15.

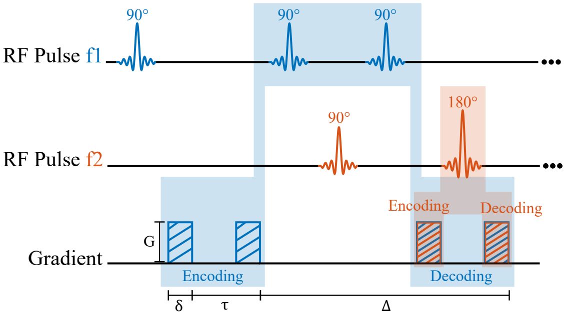

Figure 5.15: Schematic illustration of a unipolar selective flow encoding (USFE) pulse sequence. The sequence is designed for a sample containing two chemical groups with f1 and f2 Larmor frequencies.

The pulse sequence consists of four gradient lobes and five selective excitation pulses. The first and third RF pulses are just to excite the signal selectively. As shown in Figure 5.15, The first and second gradients *encode* the first signal, the second and fourth RF pulses flip its magnetization, and the third and fourth gradients decode the magnetization. So, we can say they play the role of a PFG-

STE pulse sequence for the first signal. Regarding the second signal, after it is excited by the third RF pulse, it will be encoded by the third gradient, flipped by the only 180° pulse, and decoded by the last gradient. So, the third and fourth gradients coupled with the 180° RF pulse mimic a PGSE pulse sequence for the second signal. Based on the parameters shown in Figure 5.15, the injected phase due to movement for each frequency can be calculated by the following Equations,

$$\phi_{f1} = -2\gamma\, G\, \delta\, \Delta\, v, \tag{5.6}$$

$$\phi_{f2} = -\gamma\, G\, \delta\, \tau\, v, \tag{5.7}$$

where ϕ_{f1} and ϕ_{f2} are the injected phase in the first and the second signal, respectively.

2. Bipolar selective flow encoding (BSFE) pulse sequence: The second pulse sequence doesn't have any refocusing RF pulse and is based on the bipolar motion sensitizing gradient, presented in Figure 2.23. A graphical illustration of the pulse sequence is presented in Figure 5.16.

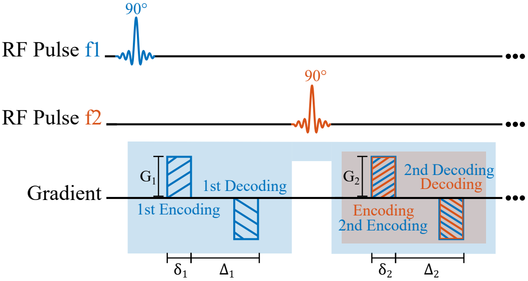

Figure 5.16: Schematic representation of a bipolar selective flow encoding (BSFE) pulse sequence. The sequence is designed for a sample containing two chemical groups with f1 and f2 Larmor frequencies.

As shown in Figure 5.16, the pulse sequence consists of two bipolar gradients. The first one is applied after exciting the first signal, and the second one is applied after exciting the second one. As a result, the first signal experiences both bipolar gradients, while the second one experiences only the second one. Compared to the USFE, this pulse sequence doesn't benefit from the refocusing pulses. However, the flow encoding gradients are completely independent of each other, and gradient power and delays can be chosen more freely. Also, the TE will be shorter and the measurement can be performed faster. Using this pulse sequence, the injected phase in each signal can be calculated by the following equations,

$$\phi_{f1} = -\gamma \left(G_1\ \delta_1\ \Delta_1 + G_2\ \delta_2\ \Delta_2 \right)\ v, \tag{5.8}$$

$$\phi_{f2} = -\gamma\, G_2\ \delta_2\ \Delta_2\ v, \tag{5.9}$$

where ϕ_{f1} and ϕ_{f2} are the injected phase in the first and the second signal, respectively.

In the next section, the pulse sequence, the printed sample holder, and the sample containing both chemical groups are used to run the selective excitation flow measurements.

5.2.4 Results and discussion

The sample holder shown in Figure 5.13 is 3D-printed by the resin *Medizinisch MED-AMB*. An MR image is taken from the sample to check the geometry of the channels. The image is shown in Figure 5.17.

As we can see, there are some resin residuals in the rectangular channel. However, the sample holder must fulfill the task. As mentioned, the sample consists of D_2O, H_2O, and NaOAc. There is a 2.9 ppm chemical shift between H_2O and NaOAc, whose effect appears as a shadow of the sample shifted above.

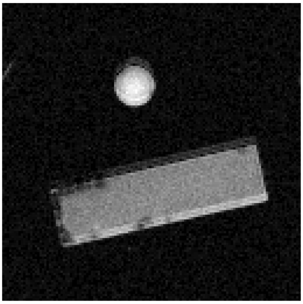

Figure 5.17: MR image of the sample containing H_2O, D_2O, and NaOAc. It shows that there is a bit of residual resin in the rectangular channel. Also, the effect of the chemical shift offset between H_2O and NaOAc can be seen in the figure.

In addition, the flow behavior is evaluated by the FLOWMAP pulse sequence available in ParaVision 360®. The result is presented in Figure 5.18.

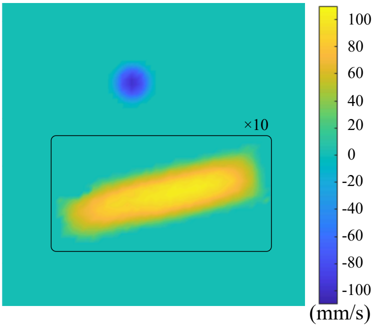

Figure 5.18: Velocity map of the sample at the flow rate of 4 mL min^{-1}. The value in the rectangular channel is multiplied by 10. The actual peak velocity is 10.3 mm s^{-1} in the rectangular channel and 97.3 mm s^{-1} in the cylindrical one.

The experimental result shows a parabolic profile in the cylindrical channel. The flow profile in the rectangular channel shows deviation from a 2D flow, which was already expected due to the fact that the ratio between the width and length of the cross-section of the channel is not very small (2/7). This deviation results in more phase injection in the net phase response versus flow rate.

In order to evaluate the experimental results of the selective pulse sequence, two sets of non-selective flow encoding experiments are carried out as benchmarks, whose pulse sequence is based on the bipolar gradient technique and is presented in Figure 5.19.

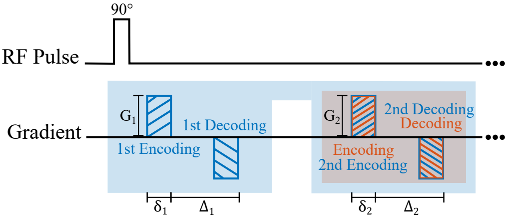

Figure 5.19: Schematic illustration of a flow encoding pulse sequence based on the bipolar gradient technique.

The sequence starts with a hard RF pulse, which precedes two bipolar gradients. In both sets, the duration of the pulse is 42.5 µs, and δ_i and Δ_i are the same. In the first set, , $G_1 = 16\%$ (equivalent to $19\,650.56\,\mathrm{Hz\,mm^{-1}}$), $G_2 = 0\%$, $\delta_1 = 2183\,\mu\mathrm{s}$. In the second one, $G_1 = G_2 = 16\%$, $\delta_1 = 2183\,\mu\mathrm{s}$, and $\delta_2 = 5555.5\,\mu\mathrm{s}$.
Based on the experimental results, these parameters generate $V_{\mathrm{enc1}} = 0.52\,\mathrm{mL\,min^{-1}}$ and $V_{\mathrm{enc2}} = 3.65\,\mathrm{mL\,min^{-1}}$ equivalent to the mean velocity of $V_{\mathrm{enc1}} = 0.62\,\mathrm{mm\,s^{-1}}$ and $V_{\mathrm{enc2}} = 4.35\,\mathrm{mm\,s^{-1}}$ in the rectangular channel. A comparison between the benchmark results and the simulation shows that the sample injects phase almost 20% more than the simulation, which was already expected. The increase in the injected phase is due to neglecting the velocity drop close to the short sides of the channel. It results in higher velocity around the center of the channel, which increases the net phase response. As a result, a correction factor of 1.2 is taken into account, and the results are compared together in Figure 5.20.
Later on, the benchmark experiments will be used as a reference to evaluate the precision of the selective measurements.
To perform the selective experiments, USFE and BSFE pulse sequences are composed in TopSpin software. Also, the reference power is obtained by the

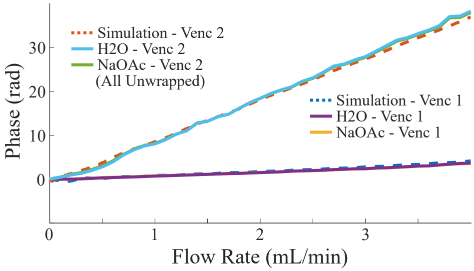

Figure 5.20: Comparison between the experimental results of the non-selective flow encoding pulse sequence and the simulation. The experiments are performed for two values of V_{enc}, $V_{\mathrm{enc}\,1} = 0.62\,\mathrm{mm\,s^{-1}}$ and $V_{\mathrm{enc}\,2} = 4.35\,\mathrm{mm\,s^{-1}}$. A correction factor of 1.2 is taken into account to compensate for the deviation from the assumption of having a 2D-flow in the rectangular channel. The phase response of the smaller V_{enc} is unwrapped.

parameter optimization tool (popt), and the power of the pulses is calibrated by the Shape Tool available by Bruker® in TopSpin 3.6.3.

The experimental parameters of the USFE pulse sequence are as follows: $G = 16\%$, $\delta = 0.5\,\mathrm{ms}$, $\tau = 9.530\,\mathrm{ms}$, $\Delta = 35.629\,\mathrm{ms}$. The shape of the selective pulses is *Sinc1.1000*, and the duration is 8.030 ms.

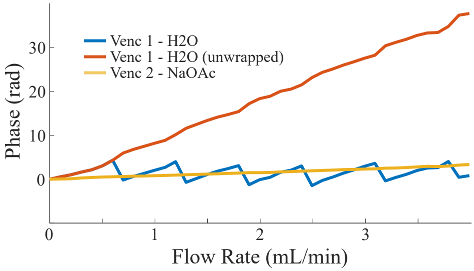

Figure 5.21: Injected phase in each signal versus flow rate for the USFE pulse sequence. The injected phase in H_2O is unwrapped based on the injected phase in NaOAc.

The results presented in Figure 5.21 show that the pulse sequence encodes the velocity into the phase of each MR signal based on two different values of V_{enc}. The value for H_2O is $V_{\mathrm{enc1}} = 0.62\,\mathrm{mm\,s^{-1}}$, and that of NaOAc is $V_{\mathrm{enc2}} = 4.35\,\mathrm{mm\,s^{-1}}$. So, the V_{enc} of NaOAc is 7 times greater than the H_2O. This invention lets us perform a reliable unwrapping on the phase of the first signal (H_2O). As shown in Figure 5.21, the signal from H_2O went through wrapping 6 times, but the phase of the MR signal from NaOAc reveals that in which turn it is. To perform the unwrapping, we need to calculate the unwrapping index. This index indicates the number of unwrappings needed to calculate the actual (unwrapped) phase. The index can be obtained by dividing π by the ratio between the values of V_{enc}. In the current case, the index is $\pi/7 = 0.47$. Now, if the phase of NaOAc is between $(i-1)\times 0.47$ and $(i)\times 0.47$, the phase of H_2O has to be added by $i \times 2\pi$.

This technique is used in the BSFE pulse sequence (Figure 5.16) as well, and the experimental results of both sequences are compared with the benchmark results. The experimental parameters of the BSFE pulse sequence are the following: $G_1 = G_2 = 16\%$ $\delta_i = \Delta_i$, $\delta_1 = 2183\,\mu\mathrm{s}$, and $\delta_2 = 5555.5\,\mu\mathrm{s}$. The selective RF pulses are the same as the USFE pulse sequence, *Sinc1.1000* with the duration of 8.030 ms.

Both pulse sequences are designed such that they result in the same values of V_{enc}. Flow rate increases up to $4.0\,\mathrm{mL\,min^{-1}}$, and the measurement is performed for 41 data points.

The experimental results presented in Figure 5.22 show that both selective excitation pulse sequences enable us to apply different values of V_{enc} in the MR signal of sodium acetate and water. Also, the results are in good agreement with the benchmark experiments obtained from the non-selective sequence. This achievement enables us to perform a measurement in which the issue of wrapping happens at $V_{\mathrm{enc}} = 4.35\,\mathrm{mm\,s^{-1}}$, but it benefits from the phase resolution of a measurement whose V_{enc} is $0.62\,\mathrm{mm\,s^{-1}}$, meaning that the velocity-phase resolution is enhanced by a factor of 7.

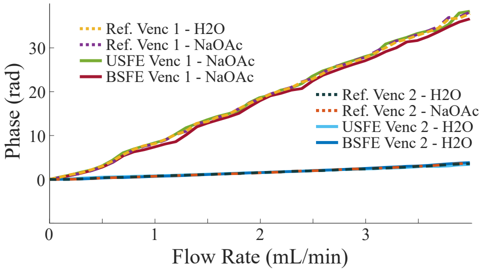

Figure 5.22: Injected phase in each signal versus flow rate. The injected phase in H_2O is shown in blue, and that of NaOAc is shown in orange.

5.2.5 Conclusion

In this chapter, the feasibility of selective excitation in MR flow measurement is proved. First, a flow sample holder is designed to provide us with a 2D-flow, whose net phase response is almost in a linear relationship with the flow rate. Then, a sample is prepared by 2M of sodium acetate (NaOAc) dissolved in 23:77 H_2O:D_2O. In order to perform the measurement by different values of V_{enc} for H_2O and NaOAc, two different selective flow encoding pulse sequences are presented. The first one, called USFE, is a hybrid of PFG-STE and PGSE and benefits from refocusing pulses. The second one, called BSFE, is based on the flow-sensitizing bipolar gradient technique and benefits from more freedom in designing the flow encoding gradients and shorter running times. First, two non-selective benchmark experiments are performed as a reference. Then, the selective pulse sequences are employed to perform flow experiments with two values of V_{enc} in a single measurement. In comparison with the references, the experimental results demonstrate high accuracy. The corresponding value of V_{enc} for water and sodium acetate are $0.62\,\mathrm{mm\,s^{-1}}$ and $4.35\,\mathrm{mm\,s^{-1}}$ respectively. It gives a ratio of 7 between the values.

There are different mechanisms to adjust this ratio. In the USFE pulse sequence, the second value of V_{enc} can change independently of the first value by changing τ. However, it has to be taken into account that the minimum value of τ is

limited by the pulse length of the 180° pulse, which depends on the desired bandwidth of the pulse. Also, the first value can be adjusted independently by changing Δ. Changing the δ and G affects both values. In the BSFE pulse sequence, all parameters can be set separately.
In this study, the ratio between values of V_{enc} is 7. Mathematically, greater ratios are possible to achieve. Technically, we can decrease the smaller one or increase the greater one. Considering the fact that the maximum velocity in the sample is fixed and the biggest V_{enc} has to be slightly greater than that, we discuss decreasing the smaller V_{enc}. For instance, the ratio can increase by increasing δ_1 in the BSFE sequence and Δ in the USFE. However, two main issues define the upper limit of this ratio. The first one is diffusion, and the second and more important one is phase dispersion due to net-phase flow measurement. Assuming the same SNR for all signals in the spectrum, it is recommended to choose the chemical with a smaller diffusion coefficient. However, if the chemicals have different values of SNR, which is the case in this study, it will be a matter of trade-off between SNR and diffusion coefficient. The second issue is phase dispersion due to net-phase flow measurement. In the case of mean flow measurement, we deal with a region in which there is a range of velocities from zero to V_{enc}. It leads to phase dispersion in the MR signal. Using a sample holder that provides a 2D-flow profile can enhance the phase uniformity and shift the loss of signal to a higher flow rate, but the SNR still suffers from this issue. In conclusion, the upper boundary is set by diffusion and, more importantly, the phase dispersion due to the net-phase effect. Also, it might be possible that the phase-SNR of the signal corresponding to the biggest V_{enc} is not enough to determine the number of wrapping in the phase of the other signal. This issue is more likely in cases of a big ratio between the values of V_{enc}. As explained before, in order to decipher the number of wrappings, we should divide π by the ratio between values of V_{enc}. Let's call this ratio R,

$$R = \frac{V_{\text{enc2}}}{V_{\text{enc1}}}. \tag{5.10}$$

Then, if the phase of the other signal is between $(i-1)\,\pi/R$ and $i\pi/R$, the phase has to be increased by $i\times 2\pi$. When R is too big, the span of $\left[(i-1)\,\pi/R\ ,\ i\pi/R\right]$ can be very small. In fact, the phase injection within this span might not be enough to dominate that of noise. In such a case, a third signal can be used whose V_{enc} is between the first two values. This topic can be among the applicable topics for further studies.

In addition, the application of selective excitation in flow MRI is highly recommended and can be tremendously helpful in flow imaging applications. In such an application, the net-phase effect is almost negligible compared to the mean flow measurement, and very high ratios between V_{enc} values are expected. In addition, this application can be used to encode three components of the velocity field $\left(V_x, V_y, V_z\right)$ into the phase of three MR signals within the same measurement. Different values of V_{enc} can be considered for each component to enhance the phase-SNR.

6 Conclusion and outlook

Three main advantages make magnetic resonance velocimetry (MRV) a novel method to evaluate flow behavior in clinical and industrial applications. First, it is non-invasive, meaning it doesn't need access to the inner side of the sample. Second, in this approach, the tracer particles are unnecessary to visualize the flow. Third, there is no need to have optical access to the flow. These merits give more credit to this method compared to some other experimental techniques, including laser Doppler anemometry (LDA), hot-wire anemometry (HWA), and particle imaging velocimetry (PIV). However, MRV has its limitations.

6.1 Conclusion

In this research, the three main limitations of MRV are addressed. The first one is the use of this technique in the flowmeter industry, which is mainly due to the high price and spacious volume of the conventional spectrometers, or in other words, due to the inconsistency of the compact ones. The second issue is about the TE, which is the main bottleneck for fast flow measurements. The last limitation is about the velocity encoding parameter V_{enc}. It has to be slightly bigger than the highest expected velocity, which limits the phase velocity resolution to a certain value. These limitations are discussed in the following, and the corresponding solutions are presented.

1. **Pulse sequence optimization for compact NMR flowmeters**
   This issue is discussed in the third chapter of the current study. A compact device with the size of $125 \times 57 \times 15\,\mathrm{mm}^3$ is chosen to measure the flow rate in a non-invasive way. In making this device, the total cost is kept

under 1000 €, and the thickness is minimized down to 15 mm so that it fits in a small permanent magnet. The flowmeter is made in the PhD framework of Dr. Pedro Silva. The pulse sequence preparation, optimizing experimental parameters, flow behavior evaluation, and flow NMR measurement are performed in this study.

The main challenge in this chapter is the frequency drift of the permanent magnet. First, a pulse sequence is written using the *Job Acquisition* technique to minimize the adverse effects of the drift. This technique lets us have two acquisitions after the excitation. The first one is collected before the application of flow-sensitizing bipolar gradient, and the second one is applied after that. To some extent, it helps us to encounter the drift problem since any drift has the same effect on both acquisitions. But this technique helps until the pulse is on-resonance enough. When it is off-resonance, it affects the excitation and, hence, the flow measurement performance. To keep the NMR experiments coherent, it is necessary to avoid *Frequency Adjustment* since it changes the working frequency and, therefore, the phase response of the hardware. To compensate for this problem, *Drift Adjustment* option is used. This adjustment uses the z_0 shimming coil to return the working frequency to its initial value. However, this adjustment can’t return the frequency precisely, and there will be a slight residual offset (in the range of 3 kHz) after running this adjustment. This issue can be tackled by choosing a broadband excitation pulse. In the next step, the phase response of the sample with three different flow profiles, including plug, rectangular, and cylindrical, is simulated for an ideally uniform laminar flow. Having the plug flow profile is not feasible. Based on the results, a rectangular one results in a high SNR for a wide range of flow rates compared to a cylindrical channel. Considering the small available volume in a compact device, the flow channel is well-designed to provide a uniform flow in front of the stripline [30]. The simulation of flow behavior by COMSOL Multiphysics shows that the flow follows the ideal behavior up to $0.25\,\mathrm{kg\,h^{-1}}$. Experimental results show that the flowmeter is still able to perform robust measurements even for higher flow rates (up to $2.0\,\mathrm{kg\,h^{-1}}$) since the phase response is locally bijective.

2. **Reduction of the echo time (TE) in flow imaging pulse sequences**
Based on the available literature, TE has the most critical effect on fast flow measurement [9]. A shorter TE is beneficial for flow measurement. It reduces the required residence time, enhances the signal intensity, and decreases the dephasing parameter.
In the fourth chapter of the current study, optimal control theory (OCT) is employed to design an excitation pulse that can perform the job of the excitation pulse and bipolar gradient concurrently. The Pontryagin Maximum Principle (PMP) is used to solve the optimal control problem (OCP). The GRadient Ascent Pulse Engineering (GRAPE) algorithm is utilized to maximize the Hamiltonian. First, the application of OCT in managing the phase of the MR images is tried. Then, this theory is used to design a slice-selective flow encoding excitation pulse. To achieve the slice selectivity, the bandwidth of the excitation pulse is constrained. The OCP is divided into two steps. The target of the first step is to establish a linear relationship between the phase and velocity of a central plane of the slice, which is on-resonance at $t = 0$. Then, the phase of the whole excited slice is evaluated. The evaluation shows that there is non-uniformity along the thickness. Therefore, the second step was initiated, and the result of the first step was used as an initial guess for the second step. The target of the second step is to improve the phase uniformity along the thickness. Despite the residual phase dispersion, the second step enhances the phase uniformity along the slice. The designed pulse shows that the delay caused in TE by flow encoding is 1.58 times less than the phase-contrast method. In addition, it performs the job of the slice selection RF pulse and refocusing gradient. Two sample holders are designed to perform the experimental measurement. The first one

has two identical parallel channels, and the second one has a cylindrical inlet, which is placed at the center of the annular outlet. Four different measurements are carried out on each of the two sample holders. The experimental results show good precision in OC flow measurements.

3. **Enhancement of phase-SNR versus the value of V_{enc}**
   The last topic of the current study is about the most critical parameter in flow MRI, V_{enc}. In phase-contrast flow encoding, the velocity of the sample is encoded into the phase of the MR signal. The encoding gradient is designed such that the phase of the voxel with the highest expected velocity is equal to π. So, before performing a measurement, the highest velocity that might be encountered should be known, and the value of V_{enc} should be chosen slightly bigger; otherwise, aliasing will happen [8]. On the contrary, V_{enc} is in a direct relationship with standard deviation [12],

   $$\text{StdDev} = \frac{\sqrt{2}}{\pi} \cdot \frac{V_{\text{enc}}}{\text{SNR}}. \tag{6.1}$$

   Based on Equation 6.1, great values of V_{enc} increase the standard deviation. That is why it should be chosen just slightly greater than the highest expected velocity, on the one hand, to avoid aliasing and, on the other hand, to keep the standard deviation as low as possible. In some cases, the velocity of a few voxels is exceptionally higher than the other voxels. We must keep the V_{enc} high in such cases. As a consequence, we lose phase-SNR for slow-moving voxels.
   This issue is discussed in the fifth chapter of the current study. The proposed solution is to use selective excitation pulses to achieve a different value of V_{enc} for each chemical group of the sample. First, this idea of selective excitation is tried for diffusion measurement. Chemical groups with different chemical shifts might have dissimilar diffusion coefficients. To reach a complete diffusion curve and calculate the coefficient precisely, different values of motion-sensitizing gradients are needed. Diffusion

measurement is conventionally performed by applying a hard pulse and then a motion-sensitizing gradient. This approach restricts us to using the same gradient for all chemical groups. Selective excitation enables us to modify the gradient according to the diffusion coefficient of the chemical group. This technique was tried to measure the diffusion coefficients of water, methionine methyl of Met-Ala-Ser, and alanine methyl of Met-Ala-Ser in a selective manner. Precise results of this study inspired us to use this technique to have multiple values of V_{enc} in NMR flow measurement. For the current study, the number of chemicals is limited to two, and, accordingly, two values of V_{enc} are defined. First, two selective flow encoding pulse sequences are proposed. Then, a sample holder is designed to provide a 2D flow profile, and it is 3D printed by an NMR-compatible resin (Medizinisch MED-AMB). A sample containing 2M of sodium acetate (NaOAc) dissolved in 23:77 H_2O:D_2O is prepared. Then, the V_{enc} of $0.62\,\mathrm{mm\,s^{-1}}$ is assigned to H_2O and $4.35\,\mathrm{mm\,s^{-1}}$ to NaOAc. The absolute value of V_{enc} (the maximum velocity encountered in the system) is $4.35\,\mathrm{mm\,s^{-1}}$. The V_{enc} of water is 7 times smaller than sodium acetate. This enhances the phase-SNR 7 times, keeping the standard deviation the same. Technically, the injected phase in H_2O goes through wrapping. But, since we know the actual value from the phase of NaOAc, a reliable unwrapping can be performed. Both proposed pulse sequences demonstrate a precise mean flow measurement.

6.2 Outlook

Three main topics were introduced in the current thesis. The results show the functionality and effectiveness of the proposed solutions. However, there is the potential for further enhancement and encouraging topics for future research.

1. **Pulse sequence optimization for a compact NMR flowmeter**
   The experimental results demonstrate a precise measurement by an NMR-

based flowmeter. However, assessments show the possibility of further improvements. The flow behavior loses its ideal behavior above a threshold flow rate. Even though the flow measurement is still doable in this flow regime, it leads to signal loss. Topology optimization of the flow channel to provide a uniform flow profile for a wider range of flow rates is among the promising topics for further studies. In addition, NMR detectors are capable of quantifying different chemicals. This feature can be particularly applicable in designing multi-phase flowmeters. Furthermore, they provide the possibility of chemical reaction monitoring, which can be beneficial in many industrial and laboratorial applications.

2. **Reduction of the echo time (TE) in flow imaging pulse sequences**
   Based on the results, the TE of the OC method is 1.58 times shorter than that of the bipolar gradient. In OCP, a dimensionless parameter called Δ_{enc} is defined. In this study, Δ_{enc} equals 3.2. The following equations can calculate the delay caused in TE by flow encoding,

   $$D_{\text{OC}} = \frac{1}{2}\sqrt{\frac{\Delta_{\text{enc}}}{\frac{\gamma}{2\pi} G \cdot V_{\text{enc}}}}. \tag{6.2}$$

   Based on Equation 6.2, the delay is directly proportional to Δ_{enc}. So, redefining the OCP and designing the pulse with a smaller value of Δ_{enc} could further increase the time efficiency of the present method. In addition, the evaluations show that the phase profile along the thickness is not uniform, which results in a loss of signal. In the current study, a non-linear relationship between phase and velocity is established by OCT. The framework of OC is quite flexible. It can be employed to design an RF pulse to achieve the desired relationship between phase and velocity. This attribute can be applicable to enhance phase-SNR for a specific flow rate, for example, for slow-moving voxels. Finally, the robustness of the current method against higher order terms (HOT) of movement is compared with that of the phase contrast (PC) method. The results show a better robustness against HOT in the OC method for fast-moving voxels, while for slow-moving ones, the PC method is better. This limitation could be removed by redefining the OCP and taking the effect of HOT into account.

3. **Enhancement of phase-SNR versus the value of V_{enc}**
   The application of selective excitation is shown in the current study. Experimental results demonstrate that the phase-SNR can be enhanced by at least a factor of 7. Depending on the absolute value of V_{enc}, greater ratios are achievable. The value of the smaller V_{enc} is limited by diffusion and phase dispersion due to the net-phase effect. For the case of net-phase flow measurement, the phase of vector summation of the magnetization of all voxels is measured. Because there is a wide range of velocities in the sample holder, the phase dispersion will be considerable. However, in the case that large ratios are achievable, the phase-SNR of the larger V_{enc} might be insufficient to unwrap the phase response of the other chemical group. In this case, a third group can be helpful.

   The application of selective excitation is used to perform multiple flow measurements within one single experiment. In this research, the difference between measurements was in the values of V_{enc}. However, this application can be used to measure a different set of parameters in the same experiment. For instance, it can be used to measure multiple components of the velocity $\left(V_x, V_y, V_z\right)$. In addition, as mentioned, the ratio between the values of V_{enc} is limited mainly due to the net-phase effect. This problem is far less of a concern in flow MRI. So, the application of selective excitation in flow MRI as a profitable topic is very encouraging for future studies.

Bibliography

[1] Ismail, I., Gamio, J. C., Bukhari, S. F., and Yang, W. Q. Tomography for multi-phase flow measurement in the oil industry, *Flow Measurement and Instrumentation*, **2005**, *16*, 145–155.

[2] Xu, L. J., and Xu, L. A. Gas/liquid two-phase flow regime identification by ultrasonic tomography, *Flow Measurement and Instrumentation*, **1997**, *8*, 145–155.

[3] Cha, J. E., Ahn, Y. C., and Kim, M. H. Flow measurement with an electromagnetic flowmeter in two-phase bubbly and slug flow regimes, *Flow Measurement and Instrumentation*, **2002**, *12*, 329–339.

[4] Yiallourou, T. I., Kröger, J. R., Stergiopulos, N., Maintz, D., Martin, B. A., and Bunck, A. C. Comparison of 4D Phase-Contrast MRI Flow Measurements to Computational Fluid Dynamics Simulations of Cerebrospinal Fluid Motion in the Cervical Spine, *PLoS ONE*, **2012**, *7*.

[5] Fukushima, E. Nuclear magnetic resonance as a tool to study flow, *Annual Review of Fluid Mechanics*, **1999**, *31*, 95–123.

[6] Johnson, D. A. *Laser Doppler anemometry*; NASA Ames Research Center Moffett Field: California, US, **1988**.

[7] Freudenhammer, D., Baum, E., Peterson, B., Böhm, B., Jung, B., and Grundmann, S. Volumetric intake flow measurements of an IC engine using magnetic resonance velocimetry, *Experiments in Fluids*, **2014**, *55*.

[8] Elkins, C. J., Markl, M., Pelc, N., and Eaton, J. K. 4D Magnetic resonance velocimetry for mean velocity measurements in complex turbulent flows, *Experiments in Fluids*, **2003**, *34*, 494–503.

[9] Gladden, L. F., and Sederman, A. J. Recent advances in Flow MRI, *Journal of Magnetic Resonance*, **2013**, *229*, 2–11.

[10] Colnago, L. A., Andrade, F. D., Souza, A. A., Azeredo, R. B., Lima, A. A., Cerioni, L. M., Osán, T. M., and Pusiol, D. J. Why is Inline NMR Rarely Used as Industrial Sensor? Challenges and Opportunities, *Chemical Engineering & Technology*, **2014**, *37*, 191–203.

[11] Gladden, L. F. Magnetic resonance: Ongoing and future role in chemical engineering research, *AIChE Journal*, **2003**, *49*, 2–9.

[12] Pelc, N. J., Sommer, F. G., Li, K. C., Brosnan, T. J., Herfkens, R. J., and Enzmann, D. R. Quantitative magnetic resonance flow imaging., *Magnetic resonance quarterly*, **1994**, *10*, 125–147.

[13] Jiang, L. l., Song, Y. c., Liu, Y., Dou, B. l., Zhu, N. j., Zhao, J. f., and Buliti, A. Measurement of fluid flow in pipe and porous media by high-resolution magnetic resonance imaging, *China Ocean Engineering*, **2012**, *26*, 317–328.

[14] Kugel, H. Improving the signal-to-noise ratio of NMR signals by reduction of inductive losses, *Journal of Magnetic Resonance (1969)*, **1991**, *91*, 179–185.

[15] Elkins, C. J., and Alley, M. T. Magnetic resonance velocimetry: Applications of magnetic resonance imaging in the measurement of fluid motion, *Experiments in Fluids*, **2007**, *43*, 823–858.

[16] Elkins, C. J., Alley, M. T., Saetran, L., and Eaton, J. K. Three-dimensional magnetic resonance velocimetry measurements of

turbulence quantities in complex flow, *Experiments in Fluids*, **2009**, *46*, 285–296.

[17] Huang, L., Mikolajczyk, G., Küstermann, E., Wilhelm, M., Odenbach, S., and Dreher, W. Adapted MR velocimetry of slow liquid flow in porous media, *Journal of Magnetic Resonance*, **2017**, *276*, 103–112.

[18] Deng, F., Xiao, L., Liao, G., Zong, F., and Chen, W. A new approach of two-dimensional the NMR relaxation measurement in flowing fluid, *Applied Magnetic Resonance*, **2014**, *45*, 179–192.

[19] Shukla, M. N., Vallatos, A., Phoenix, V. R., and Holmes, W. M. Accurate phase-shift velocimetry in rock, *Journal of Magnetic Resonance*, **2016**, *267*, 43–53.

[20] Levitt, M. *Spin Dynamics: Basics of Nuclear Magnetic Resonance.*; Wiley: Chichester, **2001**.

[21] Günther, H. *NMR Spectroscopy: Basic Principles, Concepts and Applications in Chemistry*; John Wiley & Sons, **2013**.

[22] Bernstein, M. A., King, K. F., and Zhou, X. J. *Handbook of MRI Pulse Sequences*; **2004**; pp. 1–1017.

[23] Keeler, J. *Understanding NMR Spectroscopy*; John Wiley & Sons: Chichester, **2010**.

[24] McRobbie, D. W., Moore, E. A., Graves, M. J., and Prince, M. R. *MRI from Picture to Proton*; Cambridge University Press, **2006**; pp. 1–397.

[25] Omar Nassar, Innovative micro-NMR/MRI functionality utilizing flexible electronics and control systems. Ph.D. thesis, Karlsruhe Institute of Technology, **2021**.

[26] 2023 AD Elster, E. L. Predicting nuclear spin - Questions and Answers âin MRI. https://mriquestions.com/predict-nuclear-spin-i.html.

[27] Lauterbur, P. C. Image formation by induced local interactions: Examples employing nuclear magnetic resonance, *Nature*, **1973**, *242*, 190–191.

[28] Female human dummy | 3D CAD Model Library | GrabCAD. https://grabcad.com/library/female-human-dummy-1/details?folder_id=779795.

[29] Silva, P. F., Jouzdani, M. A., Condesso, M., Hurtado Rivera, A. C., Jouda, M., and Korvink, J. G. Net-phase flow NMR for compact applications, *Journal of Magnetic Resonance*, **2022**, *341*, 107233.

[30] Silva, P. F. Concepts in low-cost and flow NMR. Ph.D. thesis, Karlsruhe Institute of Technology, **2023**.

[31] Weigang, E., Kari, F. A., Beyersdorf, F., Luehr, M., Etz, C. D., Frydrychowicz, A., Harloff, A., and Markl, M. Flow-sensitive four-dimensional magnetic resonance imaging: flow patterns in ascending aortic aneurysms, *European Journal of Cardio-thoracic Surgery*, **2008**, *34*, 11–16.

[32] Stalder, A. F., Frydrychowicz, A., Russe, M. F., Korvink, J. G., Hennig, J., Li, K., and Markl, M. Assessment of flow instabilities in the healthy aorta using flow-sensitive MRI, *Journal of Magnetic Resonance Imaging*, **2011**, *33*, 839–846.

[33] Piro, M. H., Wassermann, F., Grundmann, S., Tensuda, B., Kim, S. J., Christon, M., Berndt, M., Nishimura, M., and Tropea, C. Fluid flow investigations within a 37 element CANDU fuel bundle supported by magnetic resonance velocimetry and computational fluid dynamics, *International Journal of Heat and Fluid Flow*, **2017**, *66*, 27–42.

[34] Andrade, D. E., Ferrari, M., and Coussot, P. The liquid regime of waxy oils suspensions: A magnetic resonance velocimetry analysis, *Journal of Non-Newtonian Fluid Mechanics*, **2020**, *279*, 104261.

[35] Serkova, N. J., and Brown, M. S. Quantitative analysis in magnetic resonance spectroscopy: From metabolic profiling to in vivo biomarkers. **2012**; https://pubmed.ncbi.nlm.nih.gov/22303835/.

[36] Jouda, M., Torres Delgado, S. M., Jouzdani, M. A., Mager, D., and Korvink, J. G. ArduiTaM: accurate and inexpensive NMR auto tune and match system, *Magnetic Resonance*, **2020**, *1*, 105–113.

[37] Richard, S. J., and Newling, B. Measuring Flow Using a Permanent Magnet with a Large Constant Gradient, *Applied Magnetic Resonance*, **2019**, *50*, 627–635.

[38] Osán, T. M., Ollé, J. M., Carpinella, M., Cerioni, L. M., Pusiol, D. J., Appel, M., Freeman, J., and Espejo, I. Fast measurements of average flow velocity by Low-Field 1H NMR, *Journal of Magnetic Resonance*, **2011**, *209*, 116–122.

[39] O'Neill, K. T., Klotz, A., Stanwix, P. L., Fridjonsson, E. O., and Johns, M. L. Quantitative multiphase flow characterisation using an Earth's field NMR flow meter, *Flow Measurement and Instrumentation*, **2017**, *58*, 104–111.

[40] Wapler, M. C., Leupold, J., Dragonu, I., Von Elverfeld, D., Zaitsev, M., and Wallrabe, U. Magnetic properties of materials for MR engineering, micro-MR and beyond, *Journal of Magnetic Resonance*, **2014**, *242*, 233–242.

[41] Appel, M., Freeman, J. J., and Pusiol, D. Robust multi-phase flow measurement using magnetic resonance technology, SPE Middle East Oil and Gas Show and Conference, MEOS, Proceedings, **2011**; pp. 932–951.

[42] Armstrong, J., E. Suddath Application of Pontryagin's Maximum Principle to the Lunar Orbit Rendezvous Problem, **1963**.

[43] Dorfman, R. An Economic Interpretation of optimal Control theory, *American economic review*, **1969**, *59*, 817–831.

[44] Lefebvre, P. M., Van Reeth, E., Ratiney, H., Beuf, O., Brusseau, E., Lambert, S. A., Glaser, S. J., Sugny, D., Grenier, D., and Tse Ve Koon, K. Active control of the spatial MRI phase distribution with optimal control theory, *Journal of Magnetic Resonance*, **2017**, *281*, 82–93.

[45] Sugny, D., Lapert, M., and Glaser, S. J. Geometric optimal control of the contrast problem in Magnetic Resonance Imaging, *IFAC Proceedings Volumes (IFAC-PapersOnline)*, **2012**, *45*, 231–235.

[46] Tošner, Z., Vosegaard, T., Kehlet, C., Khaneja, N., Glaser, S. J., and Nielsen, N. C. Optimal control in NMR spectroscopy: Numerical implementation in SIMPSON, *Journal of Magnetic Resonance*, **2009**, *197*, 120–134.

[47] Van Reeth, E., Ratiney, H., Tesch, M., Grenier, D., Beuf, O., Glaser, S. J., and Sugny, D. Optimal control design of preparation pulses for contrast optimization in MRI, *Journal of Magnetic Resonance*, **2017**, *279*, 39–50.

[48] Pontryagin, L. Mathematical Theory of Optimal Processes. **1962**; https://doi.org/10.1002/zamm.19630431023.

[49] P Lasalle Rias, B. J. Time optimal control systems, *Proceedings of the National Academy of Sciences*, **1959**, *45*, 573–577.

[50] Bellman, R., Kashef, B. G., and Casti, J. Differential quadrature: A technique for the rapid solution of nonlinear partial differential equations, *Journal of Computational Physics*, **1972**, *10*, 40–52.

[51] Bellman, R., Kashef, B., and Vasudevan, R. The inverse problem of estimating heart parameters from cardiograms, *Mathematical Biosciences*, **1974**, *19*, 221–230.

[52] Shu, C., and Richards, B. E. Application of generalized differential quadrature to solve twoâdimensional incompressible NavierâStokes equations, *International Journal for Numerical Methods in Fluids*, **1992**, *15*, 791–798.

[53] Quan, J. R., and Chang, C. T. New insights in solving distributed system equations by the quadrature method-I. Analysis, *Computers and Chemical Engineering*, **1989**, *13*, 779–788.

[54] Bert, C. W., and Malik, M. Differential quadrature method in computational mechanics: A review, *Applied Mechanics Reviews*, **1997**, *50*, 552.

[55] Eisinberg, A., and Fedele, G. Discrete orthogonal polynomials on Gauss-Lobatto Chebyshev nodes, *Journal of Approximation Theory*, **2007**, *144*, 238–246.

[56] Khaneja, N., Reiss, T., Kehlet, C., Schulte-Herbrüggen, T., and Glaser, S. J. Optimal control of coupled spin dynamics: Design of NMR pulse sequences by gradient ascent algorithms, *Journal of Magnetic Resonance*, **2005**, *172*, 296–305.

[57] Alinaghian Jouzdani, M., Jouda, M., and Korvink, J. G. Optimal control flow encoding for time-efficient magnetic resonance velocimetry, *Journal of Magnetic Resonance*, **2023**, *352*, 107461.

[58] Skinner, T. E., Reiss, T. O., Luy, B., Khaneja, N., and Glaser, S. J. *Application of Optimal Control Theory to the Design of Broadband Excitation Pulses for High Resolution NMR*; **2003**; Vol. 163; pp. 8–15.

[59] Stöcker, T., Vahedipour, K., Pflugfelder, D., and Shah, N. J. High-performance computing MRI simulations, *Magnetic Resonance in Medicine*, **2010**, *64*, 186–193.

[60] Bruker, *ParaVision 360 V3.1 User Manual*; Bruker BioSpin MRI GmbH, **2021**; pp. 1–1196.

[61] MacKinnon, N., Alinaghian, M., Silva, P., Gloge, T., Luy, B., Jouda, M., and Korvink, J. G. Selective excitation enables encoding and measurement of multiple diffusion parameters in a single experiment, *Magnetic Resonance*, **2021**, *2*, 835–842.

[62] Jain, S. V., S. K. Bentley's Textbook of Pharmaceutics - E-Book - Google Books. **2011**; https://www.google.de/books/edition/Bentley_s_Textbook_of_Pharmaceutics_E_Bo/V-9ozTdWdeMC?hl=en&gbpv=0&bshm=rime/1.

[63] Hrabe, J., Kaur, G., and Guilfoyle, D. N. Principles and limitations of NMR diffusion measurements, *Journal of Medical Physics*, **2007**, *32*, 34–42.

[64] Stejskal, E. O., and Tanner, J. E. Spin diffusion measurements: Spin echoes in the presence of a time-dependent field gradient, *The Journal of Chemical Physics*, **1965**, *42*, 288–292.

[65] Larive, A. M. D., and K., C. NMR Spectroscopy with Spectral Editing for the Analysis of Complex Mixtures, *Applied Spectroscopy*, **1999**, *53*, 426A–440A.

[66] Wu, D. H., Chen, A., and Johnson, C. S. An Improved Diffusion-Ordered Spectroscopy Experiment Incorporating Bipolar-Gradient Pulses. **1995**.

[67] Tofts, P. S., Lloyd, D., Clark, C. A., Barker, G. J., Parker, G. J., McConville, P., Baldock, C., and Pope, J. M. Test liquids for quantitative

MRI measurements of self-diffusion coefficient in vivo, *Magnetic Resonance in Medicine*, **2000**, *43*, 368–374.

A Appendix

MATLAB Codes to design the OC flow encoding RF pulse

https://github.com/mehrdad00013/Optimal-Control-Flow-Encoding-.git

Acknowledgement

I hereby would like to express my deep gratitude to all the people who supported me during this wonderful journey. My sincere gratitude goes to ...

1. My supervisor, Prof. Dr. Jan Korvink. I highly appreciate your consistent support during the ups and downs of my Ph.D. I encountered many challenges during this time, and your helpful hints and pieces of advice helped me to find my way. I will never forget your support during my hard days.

2. Prof. Dr. Jürgen Hennig for accepting being the co-examiner of my Ph.D. exam. I highly appreciate it. Your suggestions would be exceptionally helpful to follow my career, and I am really looking forward to them.

3. My group leader, Dr. Mazin Jouda. You have been always supporting me during this time. You gave me many instrumental suggestions. I owe many wonderful ideas and solutions to you. Without your support, it would have been impossible to achieve them.

4. All of my wonderful supportive colleagues at IMT. My former colleagues, Dr. Hossein Davoodi, Dr. Emil Mamleyev, Dr. Pedro Silva, and Dr. Erwin Fuhrer. You welcomed me warmly and helped me a lot as a new Ph.D. student. My current colleagues Dr. Neil MacKinnon, Dr. Dario Mager, Dr. Sören Lehmkuhl, Ahsana Sadaf, Mohammad Rasool Vaezi Kakhki, Hossein Esmaeilizadshali, Albina Julius, Andrea Cristina Hurtado Rivera.

5. The last but the most, my father and my mother. I am out of words. It is not possible to describe the love, support, care, and blessings that I

received from you. I can’t express my gratitude in words. There is nothing more beautiful than your happiness in the world, and I am sure you are the happiest people to see my success. Thank you very much for everything. I LOVE YOU ♡.